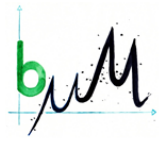




**UNIVERSITÄT  
BAYREUTH**



**An experimental analysis of pressure  
pumping at the air-soil interface in a  
moderately dense spruce forest, Waldstein,  
Germany**

Micrometeorology Group  
University of Bayreuth

**Master Thesis**

submitted by

**Elena Nitzler**

Student number: 1366536

Born on 06.08.1995 in Aschaffenburg

**June 2021**

**First Examiner:**  
**Second Examiner:**

Prof. Dr., C. K. Thomas  
Dr.rer.nat., W. Babel

# Contents

<b>List of Abbreviations and Symbols</b>	<b>II</b>
<b>List of Figures</b>	<b>IV</b>
<b>List of Tables</b>	<b>VI</b>
<b>Selbstständigkeitserklärung</b>	<b>VII</b>
<b>Abstract</b>	<b>VIII</b>
<b>Zusammenfassung</b>	<b>X</b>
<b>1 Introduction</b>	<b>1</b>
<b>2 Data Acquisition</b>	<b>9</b>
2.1 Experimental Site . . . . .	9
2.2 Experimental Setup . . . . .	13
<b>3 Processing and Analysis</b>	<b>15</b>
3.1 Flux Analysis . . . . .	15
3.2 Pressure Pumping Analysis . . . . .	16
<b>4 Results and Discussion</b>	<b>22</b>
4.1 Flux Analysis . . . . .	22
4.2 Time Series Analysis . . . . .	27
4.3 Quadrant Analysis . . . . .	34
<b>5 Conclusions</b>	<b>52</b>
<b>Acknowledgements</b>	<b>55</b>
<b>Bibliography</b>	<b>56</b>
<b>Appendices</b>	<b>61</b>
<b>A Data Processing</b>	<b>61</b>
<b>B Flux Analysis</b>	<b>62</b>
<b>C Time Series Analysis</b>	<b>66</b>
<b>D Quadrant Analysis</b>	<b>70</b>



# List of Abbreviations and Symbols

## Abbreviations

BT	Background Turbulence
C	Fully Coupled canopy
Cs	Coupled canopy by sweeps
CS	Coherent Structures
Dc	Decoupled canopy
Dg	Decoupled ground layer
Ds	Decoupled sub-canopy
EC	Eddy Covariance
H	Hypotheses
INTRAMIX	INvestigation of TRANsport and MIXing
LOeWE	Large eddy Observatory Waldstein Experiment
NEE	Net Ecosystem Exchange
RQ	Research Questions
SWC	Soil Water Content
Syn <sub>mean</sub>	Synoptic mean flow
Syn <sub>prime</sub>	Synoptic perturbation
TKE	Turbulence Kinetic Energy
VSMC	Volumetric Soil Moisture Content
Wa	Wave motion

## Symbols

$CO_2 \text{ soil}$ [ $mmolm^{-3}$ ]	CO <sub>2</sub> at the soil station
$CO_2 \text{ 4m}$ [ $mmolm^{-3}$ ]	CO <sub>2</sub> at the 4 m height station
$F_{CO_2, \text{ top}}$ [ $\mu mol s^{-1} m^{-2}$ ]	Above canopy CO <sub>2</sub> flux
$frc_{\text{corr}}$ [—]	Spectral frequency correction factor (Moore, 1986)
$p_{\text{soil}}$ [ $hPa$ ]	Pressure at the soil station
$p_{\text{4m}}$ [ $hPa$ ]	Pressure at the 4 m height station
$\overline{p'p'}$ [ $hPa^2$ ]	Pressure variance

$Q_H$ [ $Wm^{-2}$ ]	Sensible heat flux
$Q_{LE}$ [ $Wm^{-2}$ ]	Latent heat flux
$R^2$ [—]	Coefficient of determination
$R_{e\ sub}$ [ $\mu mols^{-1}m^{-2}$ ]	Sub-canopy respiration
$\Delta S$ [ $\mu mols^{-1}m^{-2}$ ]	Temporal change of the storage term
$T_{s\ soil}$ [ $^{\circ}C$ ]	Sonic temperature at the soil station
$T_{s\ 4m}$ [ $^{\circ}C$ ]	Sonic temperature at the 4 m height station
$\tau$ [s]	Turbulent time scale / perturbation time
$\tau_{adj}$ [s]	Turbulent adjustment time scale
$\tau_A$ [s]	Averaging time
$U$ [ $ms^{-1}$ ]	effective windspeed
$u_{4m}$ [ $ms^{-1}$ ]	Along-wind component at the 4 m height station
$u_*$ [ $ms^{-1}$ ]	Friction velocity
$v_{4m}$ [ $ms^{-1}$ ]	Cross-wind component at the 4 m height station
$w_{soil}$ [ $ms^{-1}$ ]	Vertical wind speed at the soil station
$w_{4m}$ [ $ms^{-1}$ ]	Vertical wind speed at the 4 m height station
$\overline{w'CO_2'}$ [ $\mu mols^{-1}m^{-2}$ ]	CO <sub>2</sub> flux
$\overline{X}_{all\ raw}$ [(like variable)]	Mean over the entire raw data
$X'_{BT}$ [(like variable)]	Flow mode of background turbulence
$X'_{CS}$ [(like variable)]	Flow mode of coherent structures
$X_{raw}$ [(like variable)]	Raw data
$\overline{X}_{Syn}$ [(like variable)]	Synoptic mean flow
$\overline{X}_{30\ s}$ [(like variable)]	30 s averaged data
$\overline{X}_{30\ min}$ [(like variable)]	30 min averaged data



# List of Figures

1.1	Illustration of the conceptual framework used to improve estimates of net ecosystem exchange (NEE) in tall, dense canopies. . . . .	4
1.2	Illustration of conceptual flow modes and pressure pumping in a dense spruce forest . . . . .	6
1.3	Time scales of atmospheric fluxes . . . . .	7
2.1	Map of the Fichtelgebirge region in northern Bavaria, Germany. . . . .	10
2.2	Climate data for the respective time periods of the INTRAMIX and LOeWE campaign. . . . .	11
2.3	Soil property values for the respective time periods of the INTRAMIX and LOeWE campaign. . . . .	12
2.4	Windrose plots for the experimental site Waldstein (2017 to 2019) . . . . .	13
2.5	Experimental setup for the pressure pumping analysis during the INTRAMIX campaign and the LOeWE campaign . . . . .	14
3.1	Diurnal distribution of the remaining data after filtering. . . . .	18
3.2	Weak-wind threshold for the LOeWE campaign. . . . .	19
3.3	Schematic sketch for the quadrant analysis technique . . . . .	20
4.1	Flux analysis overview for the LOeWE campaign 4 m station . . . . .	24
4.2	Flux analysis overview for the LOeWE campaign soil station . . . . .	25
4.3	Diurnal course of the $CO_2$ flux, sensible heat flux, and latent heat flux . . . .	26
4.4	Time series analysis of pressure during the INTRAMIX campaign . . . . .	29
4.5	Time series analysis of pressure during the LOeWE campaign . . . . .	30
4.6	Time series analysis case study of pressure during the INTRAMIX campaign	31
4.7	Time series analysis case study of pressure during the LOeWE campaign . .	32
4.8	Correlation between pressure on a synoptic and coherent structure time scale for the INTRAMIX and LOeWE campaign . . . . .	34
4.9	Schematic figure of processes involved for each quadrant of a $p_{soil}' - CO_{2\ soil}'$ correlation plot . . . . .	36
4.10	Temperature dependent quadrant analysis of the normalized $p_{soil}' - CO_{2\ soil}'$ correlation for the INTRAMIX campaign . . . . .	39
4.11	Temperature dependent quadrant analysis of the normalized $p_{soil}' - CO_{2\ soil}'$ correlation for the LOeWE campaign . . . . .	40
4.12	Wind regime dependent quadrant analysis of the normalized $p_{soil}' - CO_{2\ soil}'$ correlation for the INTRAMIX campaign . . . . .	41
4.13	Wind regime dependent quadrant analysis of the normalized $p_{soil}' - CO_{2\ soil}'$ correlation for the LOeWE campaign . . . . .	42

4.14	Kernel density quadrant analysis of the normalized $w_{\text{soil}}'$ - $p_{\text{soil}}'$ correlation for the INTRAMIX campaign . . . . .	43
4.15	Kernel density quadrant analysis of the normalized $w_{\text{soil}}'$ - $p_{\text{soil}}'$ correlation for the LOeWE campaign . . . . .	44
4.16	Quadrant analysis case study for the INTRAMIX campaign . . . . .	46
4.17	Quadrant analysis case study for the LOeWE campaign . . . . .	47
4.18	Quadrant analysis after times of day and wind regimes for the INTRAMIX campaign with overall wind regime and time of day specific percentage . . . . .	50
4.19	Quadrant analysis after times of day and wind regimes for the LOeWE campaign with overall wind regime and time of day specific percentage . . . . .	51
A.1	Flow chart of the pressure pumping data processing . . . . .	61
B.1	Flux analysis overview for the INTRAMIX campaign . . . . .	62
B.2	Flux analysis case study for the LOeWE campaign at the 4 m station . . . . .	63
B.3	Flux analysis case study for the LOeWE campaign at the soil station . . . . .	64
B.4	Flux analysis case study for the INTRAMIX campaign at the soil station . . . . .	65
C.1	Time series analysis of the vertical wind during the INTRAMIX campaign . . . . .	66
C.2	Time series analysis of the vertical wind during LOeWE campaign . . . . .	67
C.3	Time series analysis of the CO <sub>2</sub> concentration during the INTRAMIX campaign . . . . .	68
C.4	Time series analysis of the CO <sub>2</sub> concentration during the LOeWE campaign . . . . .	69
D.1	Wind regime dependent quadrant analysis of the normalized $w_{\text{soil}}'$ - $p_{\text{soil}}'$ correlation for the INTRAMIX campaign . . . . .	70
D.2	Wind regime dependent quadrant analysis of the normalized $w_{\text{soil}}'$ - $p_{\text{soil}}'$ correlation for the LOeWE campaign . . . . .	71
D.3	Quadrant analysis after times of day and wind regimes for the INTRAMIX campaign with quadrant specific percentage of wind regime and time of day . . . . .	72
D.4	Quadrant analysis after times of day and wind regimes for the LOeWE campaign with quadrant specific percentage of wind regime and time of day . . . . .	73



# List of Tables

3.1	Plausibility limits for forest sub-canopy statistics . . . . .	16
3.2	Variables selected for the further pressure pumping analysis processing . . .	17
3.3	Time of day index for the data sets Syn, CS and BT . . . . .	20
4.1	Quadrant analysis kernel density observation of $p_{\text{soil}}'$ against $CO_{2\text{ soil}}'$ for the INTRAMIX campaign . . . . .	37
4.2	Quadrant analysis kernel density observation of $p_{\text{soil}}'$ against $CO_{2\text{ soil}}'$ for the LOeWE campaign . . . . .	37

# Selbstständigkeitserklärung

Hiermit versichere ich, dass ich die vorliegende Arbeit selbständig und ohne die Hilfe anderer als im Literaturverzeichnis angegebener Quellen angefertigt habe. Wörtliche oder sinngemäße Zitate aus veröffentlichten und unveröffentlichten Schriften wurden kenntlich gemacht. Die Arbeit hat in gleicher oder ähnlicher Form noch keiner anderen Prüfungsbehörde vorgelegen.

---

Datum, Ort

---

Elena Nitzler



# Abstract

It has long-since been recognized by the community of boundary layer meteorology, that the common eddy-covariance (EC) technique employed to establish a mass balance for the net ecosystem exchange (NEE) in forests experiences shortcomings of its meaningfulness in the sub-canopy. Pressure-induced gas fluxes between the soil and the atmosphere referred to as the *pressure pumping phenomenon* have recently shifted into focus as they are thought to be responsible for enhancing the diffusion of soil- $\text{CO}_2$  from autotrophic and heterotrophic respiration. The resulting  $\text{CO}_2$  efflux is typically not adequately accounted for by the 3-D and 1-D mass balance approach and leads to an overestimation of NEE. The presented thesis aims at identifying flow modes capable of generating this pressure-induced exchange of  $\text{CO}_2$  between the soil and atmosphere in a moderately dense spruce forest. To that end, two temporally separated field studies, namely the INTRAMIX 2016 and the LOeWE 2020 campaign, were conducted within a mountainous central European spruce forest. The experimental setup consisted of pressure transducers, gas analyzers and ultrasonic anemometers at an installation height of 0.1 m (soil station) and 4 m (4 m station) above the ground. Four research questions and corresponding hypotheses are proposed concerning firstly the time scales and time scale-related flow modes sufficient to resolve the phenomenon of pressure pumping, secondly the type of pressure (static or dynamic) dominating the system at the soil station measurement site, thirdly the prevalent source of air (soil or sub-canopy) detected by the soil station and lastly the dependency of pressure pumping on wind regimes and times of day. The presented thesis assumes that the vertical transport of air, from the soil to the 0.1 m station ( $\text{CO}_2$  enriched) or from the sub-canopy above to the 0.1 m station ( $\text{CO}_2$  depleted), is initiated either by static pressure or advective/turbulent transport. It was found, that pressure minima on a synoptic time scale over a 30 min averaging period ( $\text{Syn}_{\text{mean}}$ ) are closely correlated (INTRAMIX  $R^2 = 0.40$ , LOeWE  $R^2 = 0.55$ ) with a high standard deviation of pressure fluctuations on a 30 s coherent structure (CS) perturbation time scale. Coherent structures are considered responsible for the coupling of air between the vertical layers of the forest system in connection with pressure fluctuations at the forest surface during the passage of fronts. A quadrant analysis on a  $p_{\text{soil}}' - \text{CO}_{2\text{soil}}'$  correlation plot determined an equal distribution of the static pressure (INTRAMIX: 43 %, LOeWE: 42 % events focused in quadrant Q2 and Q4) and the dynamic pressure (INTRAMIX: 43 %, LOeWE: 41 % events focused in quadrant Q1 and Q3) signal detected by the soil station. The same quadrant analysis could allocate over 62 % of the INTRAMIX and more than 48 % of the LOeWE CS results towards air stemming from the sub-canopy region above the soil station by identifying the initiator of motion with its directional tendencies in each quadrant. This finding gains importance when considering that 15 % of the INTRAMIX analysis plots as well as 13 % of the LOeWE events could not be attributed towards a specific

source area. A further analysis of the data revealed a conjunction of downward-directed CO<sub>2</sub> fluxes with strong-wind occurrences during daytime and transition time. Those events were additionally accompanied by warm air recorded at 0.1 m above ground. The underlying process of these observations were strong pressure gradients as well as flow instabilities at the top of the canopy in consequence of high wind velocities. The resulting coherent sweep motions led to a displacement of warm, moist air from the canopy into the sub-canopy and the ground layer. Both field studies showed similar tendencies in the presented results. While this thesis has demonstrated a high degree of reproducibility during matching environmental conditions, it is advisable to conduct additional experiments on sites with varying soil properties and forest architecture. The objective of developing a uniform method for the estimation of a meaningful NEE does not need to be restricted to the research on pressure pumping in forest systems but should span over multiple urban and natural sites, taking respective wind regimes, flow modes and topography as well as parameters of atmospheric stability and radiation into account.



# Zusammenfassung

Die Limitation der gängigen Eddy-Kovarianz (EC) Technik zur Bestimmung der Massenbilanz des Netto Ökosystem Austausches (NEE) im Unterbestand von Wäldern ist in der Grenzschichtmeteorologie allgemein bekannt. Die Gefahr einer Überschätzung des eigentlichen NEE erhöht sich zusätzlich durch einen gesteigerten druckinduzierten Gasaustausch zwischen dem Boden und der Atmosphäre. Dieses so genannte *Pressure-Pumping-Phänomen* ist in der Lage die Diffusion von  $\text{CO}_2$  im Boden aus autotropher und heterotropher Atmung zu erhöhen, was eine Unterschätzung der Bodenrespiration in der NEE Massenbilanz zur Folge hat. Im Rahmen einer Diskussion um aussagekräftige NEE Werte wurde deshalb in jüngster Zeit der Forschungsschwerpunkt auf das *Pressure-Pumping-Phänomen* verlagert. Ziel der vorliegenden Arbeit ist es, Strömungsmodi und Umweltbedingungen zu identifizieren, die den druckinduzierten Austausch von  $\text{CO}_2$  zwischen Boden und Atmosphäre in einem mäßig dichten Fichtenwald verursachen. Zu diesem Zweck wurden zwei zeitlich getrennte Feldstudien, die INTRAMIX 2016 und die LOeWE 2020 Kampagne, in einem gebirgigen mitteleuropäischen Fichtenwald durchgeführt. Der Versuchsaufbau bestand aus Druckanalysatoren, Gasanalysatoren und Ultraschallanemometern in einer Installationshöhe von 0,1 m (Bodenstation) und 4 m (4 m Station) über dem Boden. Es wurden vier Forschungsfragen mit entsprechenden Hypothesen aufgestellt. Diese betreffen zum einen die Frage welche zeitskalenbezogenen Strömungsmodi für das *Pressure-Pumping-Phänomen* verantwortlich sind. Des Weiteren wurde über die Art des Drucks spekuliert, welcher das System am Messort der Bodenstation dominiert (statischer oder dynamischer Druck). In diesem Zusammenhang wurde außerdem nach der vorherrschende Quelle der von der Bodenstation erfassten Luft gefragt (Boden oder Unterbestand) und schließlich eine Abhängigkeit des *Pressure-Pumpings* von Windregimen und Tageszeiten vorhergesagt. In der vorliegenden Arbeit wird davon ausgegangen, dass der vertikale Lufttransport vom Boden zur 0,1 m Station (Quelle mit  $\text{CO}_2$  angereicherter Luft) bzw. vom darüber liegenden Unterdach zur 0,1 m Station (Quelle mit  $\text{CO}_2$  abgereicherter Luft) entweder durch statischen Druck oder durch advektiven/turbulenten Transport ausgelöst wird. Im Rahmen der Datenanalyse wurde festgestellt, dass Druckminima auf der synoptischen Zeitskala  $\text{Syn}_{\text{mean}}$  (30 min Mittelungsintervall) eng mit einer hohen Standardabweichung der Druckschwankungen auf einer 30 s Perturbationszeitskala kohärenter Strukturen (CS) korrelieren (INTRAMIX  $R^2 = 0.40$ , LOeWE  $R^2 = 0.55$ ). Diese kohärente Strukturen wurden als ursächlich für die Kopplung der Waldluft bestimmt und mit den Druckschwankungen im Unterbestand nach Frontendurchzügen in Zusammenhang gebracht. Mittels einer Quadrantenanalyse in einem  $p_{\text{soil}}' - \text{CO}_{2\text{soil}}'$  Koordinatensystem konnte eine gleichmäßige Verteilung zwischen den von der Bodenstation erfassten statischen (INTRAMIX: 43 %, LOeWE: 42 % der Ereignisse mit einer Fokussierung im Quadranten Q2 und Q4) und dynamischen (INTRAMIX: 43 %, LOeWE: 41 % der Ereignisse mit einer

Fokussierung im Quadranten Q1 und Q3) Drucksignalen ermittelt werden. Mit selbiger Quadrantenanalyse wurde die Richtung des CO<sub>2</sub> Flusses ausgemacht und der Unterbestand bzw. Kronendachbereich oberhalb der Bodenstation als Quelle der detektierten Luft für 62 % der INTRAMIX- und mehr als 48 % der LOeWE CS Ergebnisse bestimmt. Diese Gewichtung wird vor dem Hintergrund verstärkt, dass 15 % der INTRAMIX sowie 13% der LOeWE Analyseplots keiner spezifischen Luftregion zugewiesen werden konnten. Eine weitere Zerlegung der Daten ergab eine Verbindung zwischen den abwärts gerichteten CO<sub>2</sub> Flüssen und den Starkwindereignissen während der Morgens-, Mittags- und Abendstunden. Ein Zusammenhang mit Warmluftmessungen an der Bodenstation konnte ebenfalls festgestellt werden. Der den Beobachtungen zugrundeliegende Prozess wurde auf die Entstehung großer Druckgradienten sowie auf Strömungsinstabilitäten an der Oberkannte des Kronendachs in Folge hoher Windgeschwindigkeiten zurückgeführt. Die daraus resultierenden kohärenten Absinkbewegungen führen zu einer Verdrängung von warmer, feuchter Luft aus dem Kronendach hinein in den Unterbestand und zur Bodenschicht der 0,1 m Messstation. Beide Kampagnen zeigten ähnliche Ergebnisse in ihrer Datenanalyse. Somit weißt die vorliegende Arbeit bei übereinstimmenden Umweltbedingungen ein hohes Maß an Reproduzierbarkeit auf. Im Sinne einer einheitlichen und aussagekräftigen Methode zur Messung von NEE, ist es allerdings ratsam ähnliche Versuche an Standorten mit unterschiedlichen Bodeneigenschaften und Waldarchitekturen durchzuführen. Die Einbeziehung von weiteren urbanen und natürlichen Landschaften in das Forschungsvorhaben könnte den Einfluss von Variablen wie standorttypischen Windregimen, Strömungsmodi, Topografie, Stabilitätsparameter und Strahlungsparameter auf das *Pressure-Pumping-Phänomen* verdeutlichen oder revidieren.

# 1. Introduction

In the critical zone the transfer and mixing of e.g. heat, water vapor, carbon dioxide and nutrients near the surface control the biophysical resources which affect the abundance and quality of life (Thomas, 2016). The importance of these mixing processes becomes especially apparent when CO<sub>2</sub>-budgets from leaf to continental scales are observed and the relevance of forests for the global carbon cycle are evaluated. A widely applied technique for establishing a carbon-budget within a forest system is the determination of the net ecosystem exchange (NEE) of CO<sub>2</sub> with the eddy-covariance (EC) method in a mass balance approach (Aubinet et al., 2000; Ruppert et al., 2006). However, several studies (Aubinet et al., 2000; Gu et al., 2005; Ruppert et al., 2006; Flechard et al., 2007) found a high dependency of friction velocity ( $u_*$ ) and air pressure fluctuations on NEE variability not accounted for by this approach. Pressure-induced gas fluxes between the soil and the atmosphere, commonly known as the *pressure pumping phenomenon*, have recently become of great interest for the community of boundary layer meteorology. They are thought to be responsible for enhancing the diffusion of soil-CO<sub>2</sub> from autotrophic and heterotrophic respiration (Flechard et al., 2007; Thomas et al., 2013). The resulting CO<sub>2</sub> efflux is typically not adequately captured by the 3-D and 1-D mass balance approach and leads to an overestimation of NEE (Thomas et al., 2013). Schematically, pressure pumping can be presumed as pressure perturbations which press CO<sub>2</sub>-depleted air into the soil at one location and time and force CO<sub>2</sub>-enriched air out of the soil at an other location and time (see Fig.1.2). The origin of this phenomenon is still subject to ongoing research. The forest structure and related flow modes are suggested to play a critical role for the development of pressure fluctuations sufficient to impact the soil-air gas exchange (Ruppert et al., 2006; Thomas et al., 2013). Apart from that, Subke et al. (2004) emphasize the importance of soil temperature and soil moisture on the soil CO<sub>2</sub> efflux. Similarly, Flechard et al. (2007) find that the pressure pumping effect is highly dependent on temperature and soil water content (SWC). Moreover, Maier et al. (2010) believe well and deeply aerated soils to be most affected by the pressure pumping phenomenon. This thesis aims to identify flow modes capable of generating pressure pumping in a moderately dense spruce forest. The focus lies on an extensive analysis of CO<sub>2</sub>- and pressure dynamics at the forest surface. Properties of soil and air presumed to affect the pressure pumping phenomenon are outlined and evaluated on their impact on the pressure induced exchange of CO<sub>2</sub> between the soil and atmosphere.

Forests are commonly known to act as a net sink of CO<sub>2</sub> during the day but as a net source during the night (Misson et al., 2007; Freundorfer et al., 2019). In order to correctly describe a forest system and the exchange of mass and energy within, one may have to discard classic theories of transport and mixing (e.g. Monin and Obukhov (1954)) more suitable for sufficiently strong winds and significant solar heating or radiative cooling (Thomas, 2016).



Weak-wind regimes and limited mixing are frequently encountered at forest sites. This is due to their high flow resistance. Particularly the clear bole space in the understorey termed the sub-canopy layer, experiences wind velocities usually  $\leq 1.5 \text{ m s}^{-1}$  and downward momentum transport from the stronger above-canopy flow enhances mixing (Thomas, 2011, 2016). What is more, the transport of mass and energy between the sub-canopy and above-canopy layer is significantly reduced during the weak-wind regime, especially at night (Freundorfer et al., 2019). This in turn often leads to a decoupling between the EC measurement system and the sub-canopy layer, resulting in an underestimation of the true biological  $\text{CO}_2$  flux (Freundorfer et al., 2019). Shaw et al. (1990) found that features of the sub-canopy air movement and surface pressure signal result directly from the velocity field near the top of the forest. This suggests an early indication for the importance of coupling regimes in the course of the pressure pumping discussion. The developed classification scheme for the identification of exchange regimes proposed by Thomas and Foken (2007) allows one to estimate the region of the canopy participating in the exchange of energy and matter with the above-canopy air under varying environmental conditions.

Thomas and Foken (2007) distinguish between five main exchange regimes, often following a distinct diurnal cycle:

- *Wave motion (Wa)*: The flow above the canopy is dominated by linear gravity waves rather than by turbulence. The above-canopy, canopy and sub-canopy levels are assumed to be decoupled and the exchange between those levels is negligible. These linear wave motions can be commonly observed during the night, when strong radiative cooling results in a fairly stable stratification.
- *Decoupled canopy (Dc)*: The air above the canopy is decoupled from the canopy and sub-canopy. There is no transfer of energy and matter into or out of the canopy. This extensive decoupling was shown to take place during the night and the first half of the day.
- *Decoupled sub-canopy (Ds)*: The atmosphere is coupled with the canopy, but decoupled from the subcanopy. The exchange of energy and matter is limited to the above-canopy and canopy layers. In the morning hours, the buoyancy flux at higher levels of the canopy is stronger than the one at lower levels. As well as the decoupled canopy (Dc), the decoupled sub-canopy (Ds) can therefore be observed mainly during the first half of the day.
- *Coupled sub-canopy by sweeps (Cs)*: The exchange between the above-canopy air and the sub-canopy is forced by a strong downward sweep motion. This exchange regime is a typical transition regime between Ds and C and mostly takes place during the second half of the day.
- *Fully coupled canopy (C)*: The atmosphere, the canopy and the sub-canopy are in a fully coupled state. The intense solar radiation during the afternoon together with low longitudinal wind speeds has the potential to result in unstable stratification during the second half of the day.

Based on the previous study by Thomas and Foken (2007), Thomas et al. (2013) also assume that the scalar exchange between vertical layers can be categorized into discrete canopy coupling regimes. They aim to identify a meaningful estimator for canopy mixing, coupling, and decoupling, in order to improve NEE estimates for a fairly dense mature Douglas-fire stand (see Fig.1.1). The set up was composed of concurrent eddy covariance flux observations above the main canopy crown and in the clear bole space below the sub-canopy crown (Thomas et al., 2013). In contrast to the study of Thomas and Foken (2007), which mainly focuses on the exchange of energy and matter between the above-canopy air and the canopy through upward motions (ejections) and downward motions (sweeps), Thomas et al. (2013) seek to diagnose the communication of air across the canopy profile by relating the scalar-scalar fingerprint to the turbulent mixing strength. Building on the research of Thomas et al. (2013), Freundorfer et al. (2019) additionally found a distinction between weak-wind regimes and strong wind-regimes to be important for the differentiation of coupling regimes. For strong-wind regimes e.g., turbulence in the sub-canopy tends to remain strong regardless of reduced above-canopy turbulence (Freundorfer et al., 2019). In conjunction with the diurnal dependency of coupling regimes on the NEE shown by Thomas and Foken (2007), Flechard et al. (2007) hypothesize that soil CO<sub>2</sub> storage changes and pressure pumping may explain enhanced CO<sub>2</sub> fluxes during the day and a decrease in CO<sub>2</sub> at night within the sub-canopy layer. They found that CO<sub>2</sub> accumulates in the soil during night when limited mixing takes place and transport is restricted to molecular diffusion as well as advective fluxes. During daytime however, wind-induced pressure pumping results in a gradual daytime flushing out of CO<sub>2</sub> from the soil. According to Flechard et al. (2007), soil CO<sub>2</sub> storage and friction velocity ( $u_*$ ) are negatively correlated on a diurnal time scale.

Ramp-shaped flow patterns observed in time series in and above forest canopies termed coherent structures are an important transport mechanism for CO<sub>2</sub> mass transfer in a forest system (Raupach et al., 1996). Not only do they play a major role for the differentiation of exchange regimes in Thomas and Foken (2007), but Thomas et al. (2008) also found that these structures are likely to be the underlying transport mechanism for the respiration events occurring during daytime. They define coherent structures as an aperiodic, but organized pattern in the turbulent flow on time scales of several 10 s consisting of a moderate upward motion (ejection, burst) ejecting air out of the canopy followed by a rapid downward motion (sweep, gust) injecting air into the canopy. According to Thomas et al. (2008) the vertical lifting of air in the ejection phase of one coherent structure observed at the EC tower is caused by an injection of air into the canopy (sweep phase) of a different coherent structure away from the tower. This process occurs as a dynamic change between the two phases (ejection and sweep) of a coherent structure satisfying the continuity equation. The injection displaces the air in the sub-canopy that had a sufficiently large residence time to accumulate the respiration signal of the sub-canopy. A field experiment conducted by Shaw et al. (1990) revealed a period of overpressure roughly centered around the time of passage of coherent structures related to scalar microfronts at the top of the canopy. Typically, these microfronts separate the ejection of warm, humid air from the forest and the sweep of dry, cool air from above during daytime conditions (Shaw et al., 1990). Other studies, like Ruppert et al. (2006)

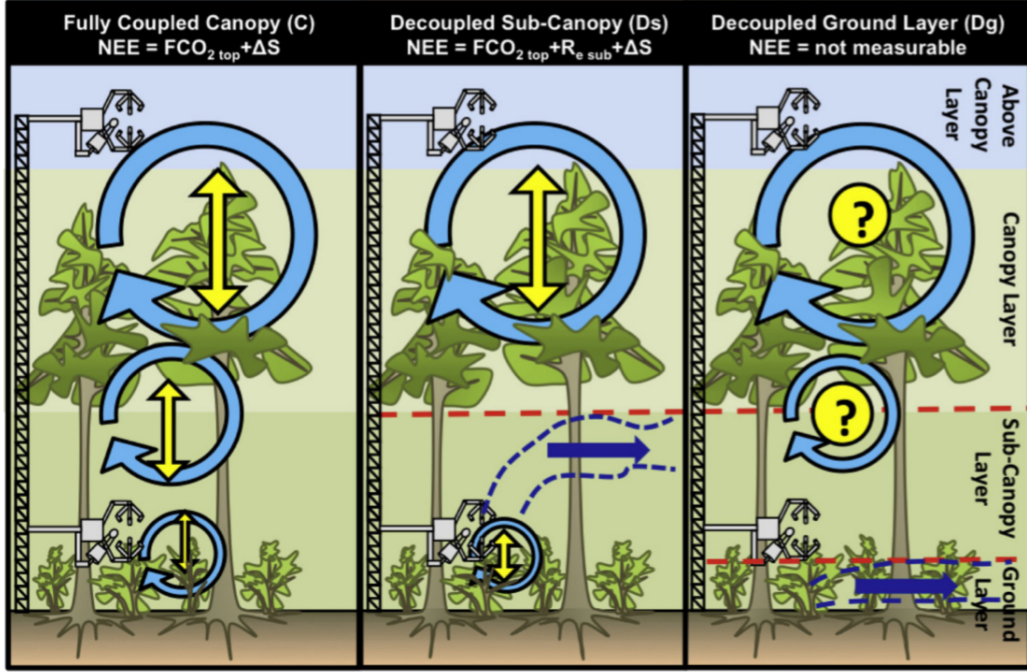


Figure 1.1.: Illustration by Thomas et al. (2013) of the conceptual framework used to improve estimates of net ecosystem exchange (NEE) in tall, dense canopies. The vertical canopy coupling decreases from left to right from the fully coupled canopy (C), over the decoupled sub-canopy (Ds), to the decoupled ground layer (Dg) regimes. For the fully coupled canopy, it is assumed that the above-canopy EC flux ( $F_{CO_2, top}$ ) integrates the turbulent exchange of all carbon sinks and sources. For the decoupled sub-canopy regime, the above-canopy EC flux only integrates over sinks and sources located in the overstory, while the sub-canopy EC observations can be used to indirectly determine the advective loss through accounting for the sub-canopy respiration ( $R_{e, sub}$ ). For the decoupled ground layer regime, turbulent mixing is very weak and advection is assumed to be the dominant term in the carbon balance, which is not captured by any of the EC systems.  $\Delta S$  is the temporal change of the storage term. Horizontal red dashed lines indicate decoupling between layers, dark blue arrows symbolize advection, and yellow vertical arrows show turbulent exchange. The light-blue circles symbolize turbulent structures in general. They are neither flow mode specific nor do they represent exact length scales.

and Takle et al. (2003) concordantly name coherent structures as a primary mechanism to enforce the phenomenon of pressure pumping.

Takle et al. (2003) distinguish between two main effects responsible for pressure pumping (see Fig.1.2):

- *Pressure fluctuations in turbulent flow (e.g. Coherent Structures)*: These scale with the square of wind speed fluctuations.
- *Pressure fluctuations attributable to variations of the mean wind interacting with obstacles (e.g. Von-Karman-Vortices)*: These are based on the square of the mean wind speed.

The findings of Shaw et al. (1990), Takle et al. (2003) and Flechard et al. (2007) agree with the conclusion of Thomas et al. (2008), who confirmed an increase in the magnitude of CO<sub>2</sub> refixation and a larger uncertainty for meaningful daytime estimates of sub-canopy respiration for very dense, multi-layered canopies with a reduced depth of penetration of coherent structures into the canopy.

One way to identify flow modes responsible for the pressure pumping phenomenon is to look into the time scales on which the respective flow modes exist. Figure 1.3 assigns the flow modes introduced in Figure 1.2 to three main categories of 5/3 small scale turbulence (or background turbulence), organized turbulence, and mean flow. However Kolmogorov's similarity theory requires these categories not to be self-contained and independent of each other, but puts them on a spectrum of turbulence where large anisotropic eddies with a high averaging time  $\tau_A$  determine small scale eddies and turbulence (Wang et al., 1996). The interdependencies and soft edges between the flow modes displayed in Figure 1.2 become especially apparent when trying to assign the so called submeso-scale motions to one of the categories mentioned above. Even though they are not normally considered part of the mean flow, submeso-scale motions can be found on time scales of minutes to up to one hour and span between the largest turbulence scales and mesoscales (Mahrt, 2010; Kang et al., 2015).

Furthermore, it is important to understand that pressure can not simply be viewed as the result of motion as Figure 1.2 and Figure 1.3 might suggest. According to the Bernoulli equation for fluid dynamics, pressure can be both, a result of motion (dynamic pressure) and the initiator of motion (static pressure) (Atkinson, 2009). The sum of the two makes out the total pressure (Lindner, 1991). More specifically, Shaw et al. (1990) point out that pressure fluctuations emanate from fields of convergence and divergence of fluid motion, whereas turbulent pressure gradients enforce velocity fluctuations. This can be derived from the necessity to satisfy the momentum equation and the Poisson equation.

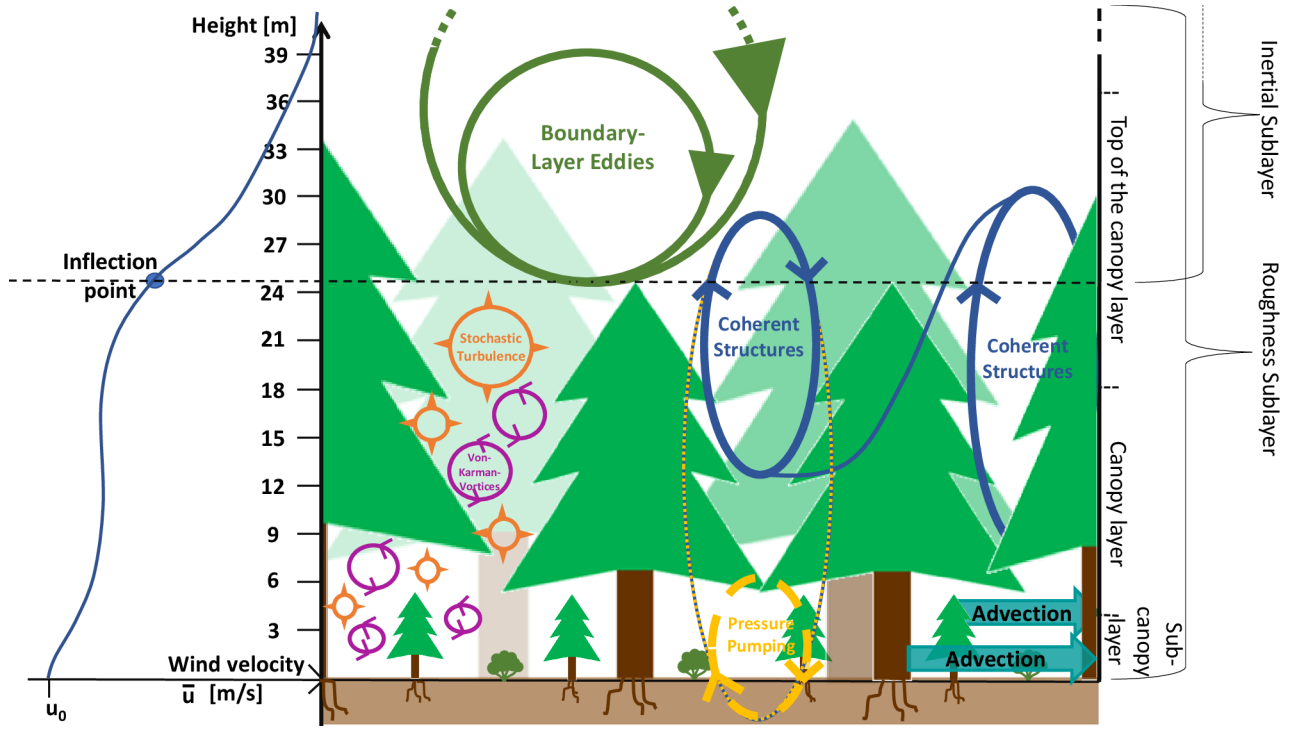


Figure 1.2.: Illustration of conceptual flow modes and pressure pumping in a dense spruce forest. The wind profile (left) shows the inflection point. This marks the point of greatest shear at the top of the canopy. Here, according to the mixing-layer hypothesis (Raupach et al., 1996), the strong wind directional and speed shear give rise to flow instabilities, which result in coherent structures (blue arrows) (Böhm et al., 2013). These coherent structures are hypothesized to be a major mechanism responsible for the phenomenon of pressure pumping (yellow arrows) (Shaw et al., 1990; Takle et al., 2003; Ruppert et al., 2006; Flechard et al., 2007). Boundary-Layer eddies (green arrows) can be found in the production range of the turbulent spectrum and are an anisotropic form of turbulence originating directly from the extraction of the turbulence kinetic energy (TKE) from the mean flow (Salesky et al., 2013; Wang et al., 1996). Von-Karman vortices (purple) build up behind obstacles due to flow separation and scale up with the size of the obstacle itself (Stoesser et al., 2009). According to Kolmogorov’s similarity theory, bigger eddies (like boundary-layer eddies, coherent structures and Von-Karman vortices) break down into smaller eddies, which are so far removed from the production range of the TKE, that they become isotropic and homogeneous in character (Wang et al., 1996). They are here termed as stochastic turbulence (orange circles). The turquoise arrows indicate an advective flow in the sub-canopy.

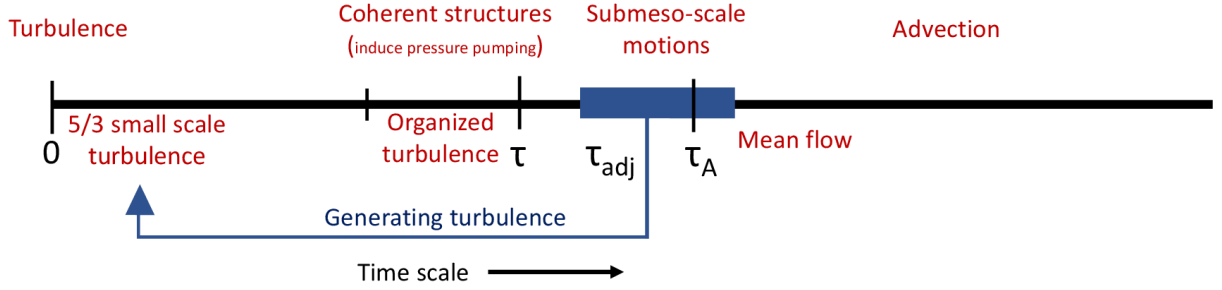


Figure 1.3.: Placing the flow modes typical for a weak-wind regime on a time scale of atmospheric fluxes. The letter  $\tau$  marks the turbulent time scale or perturbation time scale reaching from a few seconds to up to ten minutes (Orlanski, 1975; Mahrt and Thomas, 2016).  $\tau_{\text{adj}}$  marks the turbulent adjustment time scale required by the turbulence to adjust to new conditions (Mahrt and Thomas, 2016). In a weak-wind regime, the averaging time  $\tau_A$  is usually larger than the largest turbulent scale  $\tau$  (Mahrt and Thomas, 2016). According to Mahrt and Thomas (2016) this choice of  $\tau_A > \tau$  leads to perturbation quantities that include non-turbulent motions on time scales between  $\tau$  and  $\tau_A$ . The non-stationary submeso-scale motions within the  $\tau_{\text{adj}}$  range extent from several minutes to up to one hour (Mahrt, 2010). They are fit to generate turbulence and may prevent turbulence equilibrium (Mahrt and Thomas, 2016).

In order to guarantee reproducibility for the outcomes of this thesis, two corresponding but temporally separated experiments were conducted. Both were incorporated in a larger field study of the Micrometeorology Dark-Mix Group namely the INTRAMIX 2016 (INvestigation of **TR**ansport and **MIX**ing within a forest) and LOeWE 2020 (Large eddy **O**bservatory **W**aldstein **E**xperiment) campaign (see BayCEER (a), accessed 26.05.2021). The experimental setup respectively consisted of sonic anemometers, gas analyzers and pressure transducers at two levels in the sub-canopy of a spruce forest at the BayCEER research site and Fluxnet location in Waldstein / Weidenbrunnen. In connection to the overall objective of this thesis, four research questions (RQ) and respective hypotheses (H) are postulated as follows:

RQ<sub>1</sub>: *Which time scales and time scale-related flow modes are associated with the phenomenon of pressure pumping?*

H<sub>1</sub>: Coherent structures covering time scales of 30 seconds will be dominating the pressure pumping phenomenon in terms of resolution and forcing (Shaw et al., 1990; Ruppert et al., 2006). A high dependency of coherent structures on synoptic phenomena e.g. large-scale weather pattern can be expected (Shaw et al., 1990; Böhm et al., 2013).

RQ<sub>2</sub>: *Which type of pressure dominates the system at the soil station measurement site?*

H<sub>2</sub>: Based on the experimental setup with a built-in Quad-Disc probe for the detection of pressure fluctuations, it can be hypothesized that static pressure will mainly be detected by the system (Nishiyama and Bedard Jr, 1991; Liberzon and Shemer, 2010).



RQ<sub>3</sub>: *Under the assumption that a vertical transport of air is initiated by either static pressure or advective/turbulent transport, what is the dominating source area (air stemming from the sub-canopy or soil) detected at the soil station measurement site?*

H<sub>3</sub>: There will be no source of air (sub-canopy or soil) dominating over the other one during the entire experimental period. However, a dominating source area will be found for smaller time periods. This will be dependent on wind regimes, diurnal courses, soil properties and the behavior of sweeps and ejections of coherent structures (Shaw et al., 1990; Thomas and Foken, 2007; Flechard et al., 2007).

RQ<sub>4</sub>: *What is the dependency of pressure pumping on wind regimes and times of day?*

H<sub>4</sub>: The exchange regimes Cs and C as classified in Thomas and Foken (2007) mainly form during the afternoon and will be a driving force for the pressure pumping phenomenon especially during times of prevailing strong-wind regimes. In general, the pressure pumping phenomenon can be hypothesized to be more pronounced during the day (Thomas and Foken, 2007; Flechard et al., 2007).

By answering these research questions, this thesis aims at coupling physical phenomena including turbulence and mixing of air with biophysical and biochemical processes of plant physiology and soil physics. Soils and forests are known to be the largest global carbon sink (Nabuurs et al., 2007). To that end a key role for the mitigation of climate change is to understand the state of the art methods of quantifying the physical and chemical interconnections between the environmental compartments, as well as closing the gaps within the ongoing research. Through the simple and cost-effective setup presented in this thesis, valuable data can be collected. The resulting pressure pumping analysis has the potential to substantially contribute to the field of theoretical surface meteorology by closing the research gaps on the acquisition of a meaningful NEE.

## 2. Data Acquisition

The data retrieval for the pressure pumping objective requires a comprehensive understanding of the *experimental site* and *experimental setup*. The general location of the measurement stations as well as the environmental conditions under which the data was obtained are outlined in this chapter. Hereby, the focus was specifically set on parameters that have shown to impact the pressure pumping phenomenon in the past (Subke et al., 2004; Flechard et al., 2007; Ruppert et al., 2006; Thomas et al., 2013), namely soil properties, forest structure and climatic circumstances. As the thesis is based on two temporally separated field studies, this chapter additionally addresses similarities and differences in the experimental setup of both.

### 2.1. Experimental Site

The INTRAMIX campaign and the LOeWE campaign were each carried out in the northern Fichtelgebirge on the BayCEER research site (see BayCEER (b), accessed 26.04.2021) and Fluxnet location in Waldstein / Weidenbrunnen, between Weißenstadt, Sparneck and Zell (see Fig.2.1). The experimental periods spanned from 26.05.2016 to 18.07.2016 (INTRAMIX) and 25.08.2020 to 01.11.2020 (LOeWE).

The research site lies within a moderately dense spruce forest (*Picea abies*), with an average tree height of  $h_c=25$  m (measured: 2008) (see BayCEER (c), accessed 27.05.2021). At the Waldstein site the canopy extends from approximately 10 m to 25 m with the majority of the plant tissue concentrated in this area and a mean plant area index (PAI) of  $5.6 \text{ m}^2 \text{ m}^{-2}$  for the crown space and  $3.5 \text{ m}^2 \text{ m}^{-2}$  for the understorey (Ehrnsperger, 2017; Wunder, 2017). The main leaf mass is expected to be at 0.5 to 0.9  $h_c$  (see Fig. 2.1.2 in Wunder (2017)). The tree density is around  $1000 \text{ ha}^{-1}$ . In the understorey the vegetation is covering 60 to 80 % of the ground (Wunder, 2017). The sub-canopy consists of an undergrowth of herbaceous plants (*Calamagrostis villosa*, *Deschampsia flexuosa*, *Dryopteris dilatata*, *Oxalis acetosella*), dwarf shrubs (*Vaccinium myrtillus*) and mosses (*Dicranum scoparium*) (Wunder, 2017). Babel et al. (2017) found an increasing trend of annual NEE uptake with values around  $-40 \text{ g C m}^{-2} \text{ a}^{-1}$  for 1997 to 1999 and up to  $-615 \pm 79 \text{ g C m}^{-2} \text{ a}^{-1}$  for 2011 to 2014. The experimental site is characterized by a moist-temperate continental climate (Dc according to Köppen-Trewatha) with a mean annual temperature of  $5.3 \text{ }^\circ\text{C}$  (1971 to 2000) and a mean annual precipitation of  $1162.5 \text{ mm}$  (1971 to 2000) (Ehrnsperger, 2017).

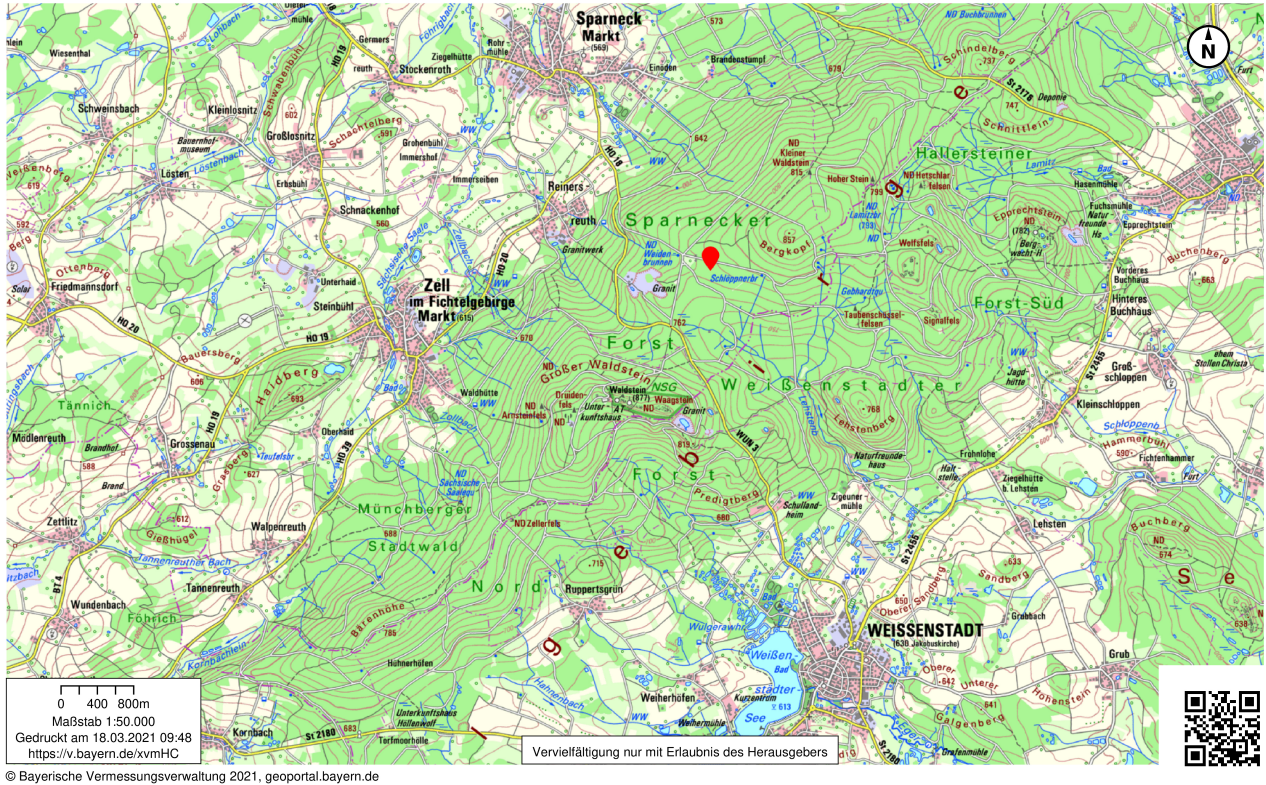


Figure 2.1.: Map of the Fichtelgebirge region in northern Bavaria, Germany (see BayernAtlas accessed 18.03.2021). The location of the Waldstein experimental site ( $50^{\circ} 08' 31''$  N,  $11^{\circ} 52' 01''$  E) of the University of Bayreuth is indicated by a red pin.

During both experiments, data of air temperature and precipitation were collected (see Fig. 2.2). With a mean of  $15.7^{\circ}\text{C}$  averaged over the measurement period of May 2016 to July 2016, the INTRAMIX campaign shows slightly warmer temperatures compared to the LOeWE campaign ( $10.7^{\circ}\text{C}$ ). In turn, the LOeWE campaign collected data during the colder summer to fall transition months (August 2020 to November 2020) and yields a higher sum of total precipitation (INTRAMIX: 55 mm; LOeWE: 66 mm).

Subke et al. (2004) conducted extensive soil research in close proximity to the Waldstein experimental site. They identified the soil type as a cambic podzol over granite bedrock, characterized by low pH values of around 3.5 to 4.2. The organic soil horizons are well stratified and of the moder type (Subke et al., 2004). The mean soil  $\text{CO}_2$  efflux was calculated as  $560 \pm 43 \text{ g C m}^{-2} \text{ a}^{-1}$  (1997 to 2000) (Subke et al., 2004). Analogously to the climate data, a detection of the parameters soil temperature and soil moisture was performed over the course of the two experiments (see Fig. 2.3). In conjunction with the air temperature analysis, the INTRAMIX campaign shows a slightly higher value for the mean soil temperature (INTRAMIX:  $11.9^{\circ}\text{C}$ ) than the LOeWE campaign (LOeWE:  $10.7^{\circ}\text{C}$ ). Despite less precipitation, the mean volumetric soil moisture content (VSMC) is noticeably higher for the INTRAMIX campaign (INTRAMIX: 31 %; LOeWE: 20 %).

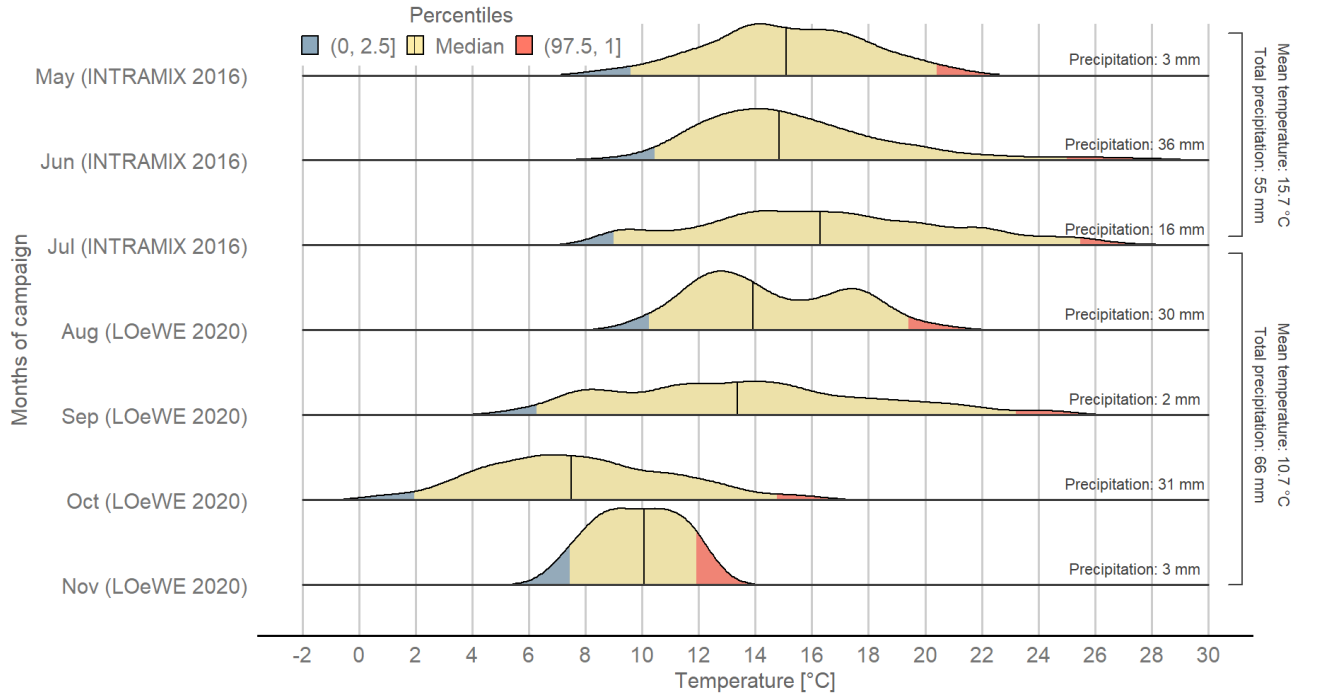


Figure 2.2.: Climate data for the respective time periods of the INTRAMIX and LOeWE campaign. For each month of the two campaigns, the temperature distribution with a 50th percentile median, the 2.5 percentile, 97.5 percentile as well as the total precipitation are given. The right side of the diagram additionally shows the mean temperature (INTRAMIX: 15.7 °C; LOeWE: 10.7 °C) and total precipitation (INTRAMIX: 55 mm; LOeWE: 66 mm) over the entire experimental periodes, respectively. The employed data is resolved in 30 min intervals. The sonic temperature was measured at the soil site pressure pumping station, whereas the precipitation data was recorded at the Pflanzgarten air quality center (see Chapter 2.2).

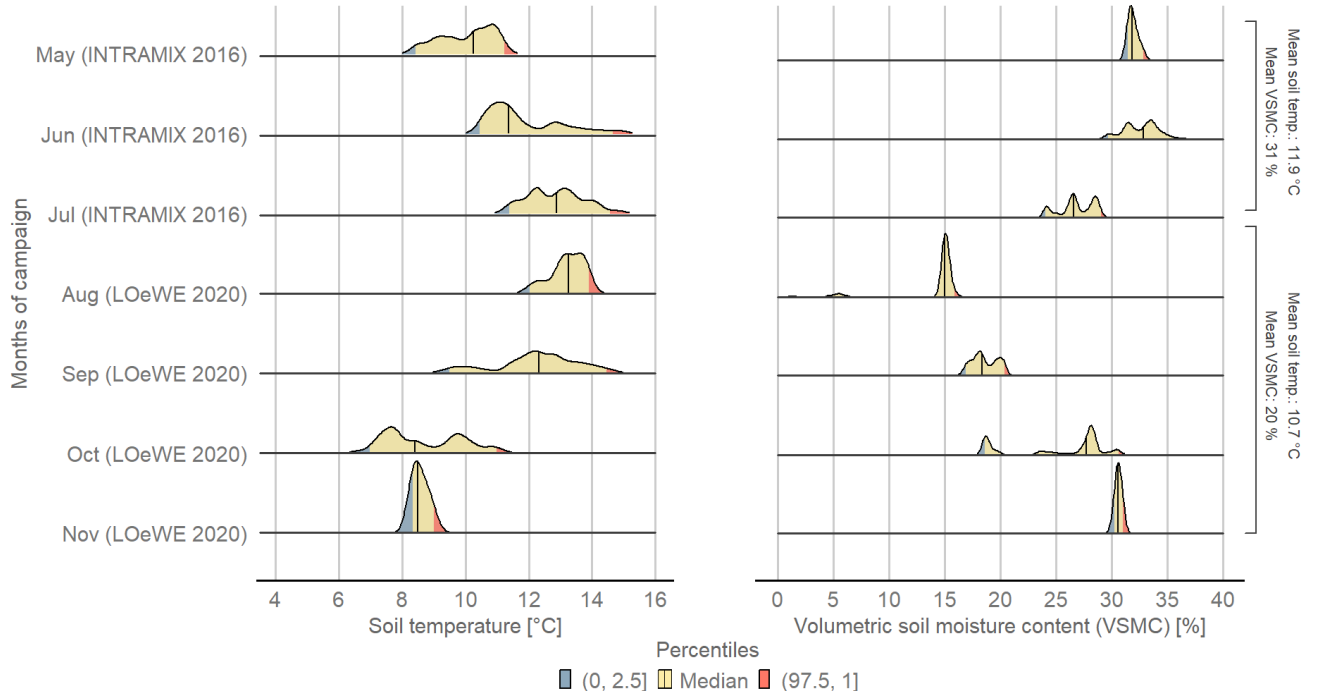


Figure 2.3.: Soil property values for the respective time periods of the INTRAMIX and LOewe campaign. For each month of the two campaigns, the distribution of soil temperature (left) and volumetric soil moisture content (right) with a 50th percentile median, the 2.5 percentile and 97.5 percentile are given. At the very right side of the two diagrams the means of both soil properties are shown for the entirety of the respective campaigns (INTRAMIX: 11.9 °C, 31 % VSMC; LOewe: 10.7 °C, 20 % VSMC). The employed data is resolved in 30 min intervals and was recorded at the Weidenbrunnen main flux tower (see Chapter 2.2).



An analysis of wind data collected prior to the LOeWE experiment was important for the correct setup of the soil station measurement site (see Chapter 2.2) and to ensure the representation of the main wind sectors in the data collection of the LOeWE experiment. Figure 2.4 displays the azimuth-corrected wind direction and wind velocity from 10 min averages of 20 Hz wind data collected at the Waldstein site from 2017 to 2019. The above-canopy flow is separated into the three main wind sectors north, south-east and west with a mean wind speed of  $3.6 \text{ m s}^{-1}$ . In the sub-canopy, the wind velocities are reduced to a mean wind speed of  $0.8 \text{ m s}^{-1}$  mainly coming from a northern direction.

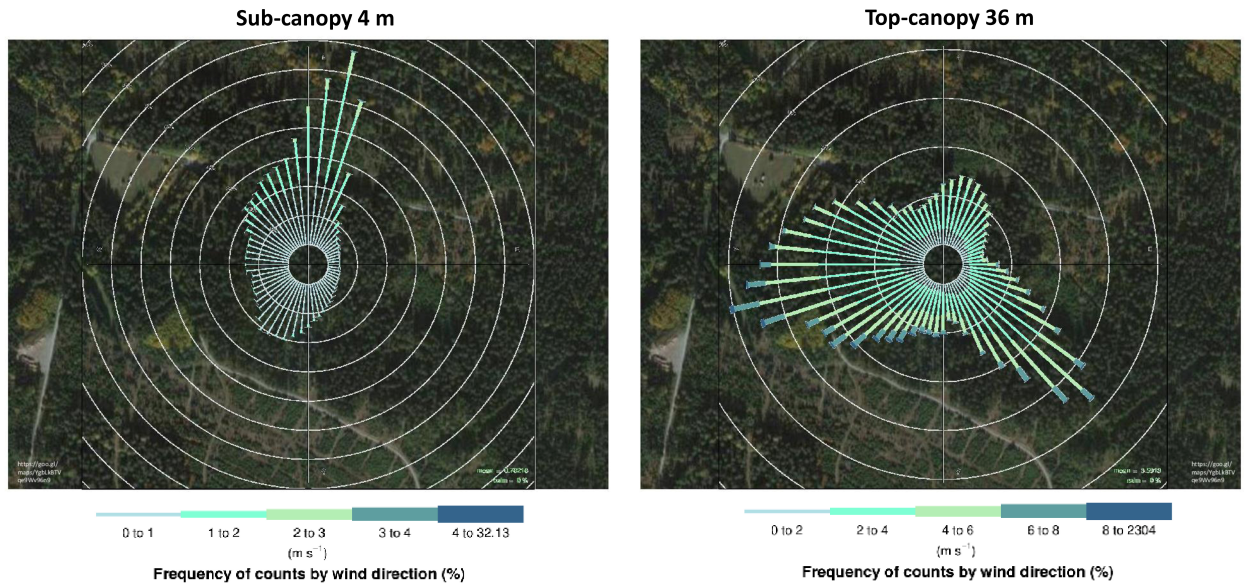


Figure 2.4.: Windrose plots for the experimental site Waldstein (2017 to 2019) ( $50^{\circ} 08' 31''$  N,  $11^{\circ} 52' 01''$ , 775 m). The plots consist of 10 min averages of 20 Hz wind data. The frequency of counts by wind direction is given in [%] and the wind velocities are shown by the color scheme light turquoise to dark turquoise with increasing magnitude for the sub-canopy at 4 m height (left) and the top-canopy at 36 m height (right).

## 2.2. Experimental Setup

The experimental setup for the pressure pumping analysis during the LOeWE campaign was designed following the pilot field studies of the INTRAMIX campaign. Since the master's thesis by Laura Ehrnsperger (2017) was part of the INTRAMIX campaign, a detailed description of an experimental setup well suited for pressure pumping analysis at the Waldstein site can also be found in her work. An infra-red gas analyzer (INTRAMIX: LI-7500, LOeWE: LI-7500) for  $\text{CO}_2$  and  $\text{H}_2\text{O}$  flux measurements was installed approximately 0.1 m above the ground (soil station) for both campaigns (see Fig. 2.5). In order to capture the vertical wind perturbations in the vicinity of the gas analyzer, an upside down sonic anemometer



(INTRAMIX: Metek USA1, LOeWE: Campbell Scientific CSAT3) was positioned right next to it. All changes in pressure on the ground were registered by a fast-response pressure transducer (INTRAMIX: Paroscientific 216b, LOeWE: Paroscientific 6000-16B-IS) for high resolution measurements of static atmospheric pressure with a built-in Quad-Disc probe. A similar setup of a non-rotated sonic anemometer (Campbell Scientific CSAT3) and pressure transducer (Paroscientific 216b) was built for the INTRAMIX campaign at a distance of 6 m from the soil station measurement site at a height of 4 m (4 m station). During the LOeWE experiment, additional measurements were conducted with a non-rotated sonic anemometer (Campbell Scientific CSAT3), a pressure transducer (Paroscientific 6000-16B-IS) and a gas analyzer (LI-7500) in 4 m height (4 m station), 68 m away from the soil measurement site. Over the course of the INTRAMIX campaign, data was collected with CR3000 data loggers at a resolution of 20 Hz. For the LOeWE campaign, the soil station measurements as well as the 4 m station data were recorded by a CR6 data logger with a 20 Hz resolution. A power outage between the 22nd to 28th of September (soil station) and the 8th to 13th of October (4 m station) led to gaps in data recording during the LOeWE experiment. Over the course of both campaigns precipitation data and soil property measurements were conducted at the Pflanzgarten air quality container (325 m distance from soil station) and Weidenbrunnen main flux tower (68 m distance from soil station), respectively.



Figure 2.5.: Experimental setup for the pressure pumping analysis during the INTRAMIX campaign on the left side and the LOeWE campaign on the right side. INTRAMIX: with pressure transducer (Paroscientific 216b in -0.05 m height within the soil), sonic anemometer (Metek USA1 in 0.16 m height) and infra-red gas analyzer (LI-7500 in 0.07 m height); LOeWE: with pressure transducer (Paroscientific 6000-16B-IS in -0.05 m height within the soil), sonic anemometer (Campbell Scientific CSAT3 in 0.16 m) and infra-red gas analyzer (LI-7500 in 0.08 m height) (photo: Laura Ehrnsperger, Elena Nitzler).

## 3. Processing and Analysis

The division of the *data processing and analysis* chapter was based on the choice of prioritization for the pressure pumping. Whilst the *flux analysis* is sufficient to present general tendencies of fluxes and environmental conditions on an averaging period of 30 min, the *pressure pumping analysis* inspects the phenomenon of pressure induced gas exchange between the soil and atmosphere in more detail and on several time scales. The latter is consequently more elaborate in its methodological description.

### 3.1. Flux Analysis

In order to receive 30 min averaged data of meaningful latent heat flux ( $Q_{LE}$ ), sensible heat flux ( $Q_H$ ), CO<sub>2</sub> flux ( $\overline{w'CO_2'}$ ) and pressure variance ( $\overline{p'p'}$ ), respective raw data had to be processed using a Matlab analysis tool for flux data (*bmmflux*) written by Christoph Thomas (see Appendix in Thomas et al. (2009)). The *bmmflux* software requires a configuration file to adjust for sensor, process and site specific characteristics. Among other things, this includes information concerning the position of the measurement instruments, their separation length as well as site specific parameters like the roughness length and canopy height of the measurement site. Additionally, common post-field data quality control corrections, namely a coordinate 3-D-rotation (Wilczak et al., 2001), a despiking of the time series data (Foken et al., 2004), a frequency response correction (Moore, 1986), a density correction for open-path instruments (Webb et al., 1980) and the Schotanus correction for the conversion of buoyancy flux into sensible heat flux (Liu et al., 2001) were applied. Precipitation data for the INTRAMIX and LOeWE campaign was downloaded from the BayEOS-Server (see BayEOS accessed 22.03.2021). Both, the results of the *bmmflux* processing and the precipitation data were further filtered and analyzed with the open source statistical software *R* (version 4.0.3). Here, the pressure variance was calculated as the square of the standard deviation of pressure for each 30 min interval. The 30 min averages of precipitation, pressure variance and flux data in the forest sub-canopy were then merged according to the respective dates, times and heights. Unphysical data were filtered out by applying the 95th percentile of the data and current literature (Launiainen et al., 2005) (see Table 3.1).

Table 3.1.: Plausibility limits for forest sub-canopy statistics

Variables	Limits
$Q_{LE} [Wm^{-2}]$	$[-60; 60]$
$Q_H [Wm^{-2}]$	$[-50; 50]$
$w'CO_2' [\mu mol s^{-1} m^{-2}]$	$[-5; -5]$
$\overline{p'p'} [hPa^2]$	$[0; 0.1]$

## 3.2. Pressure Pumping Analysis

During the pressure pumping analysis, the same processing procedure was applied to both, the INTRAMIX and LOeWE data. A basic flow chart for a more profound understanding is given in the appendices (see A.1).

The *bmmflux* software was used to average the 4 m height station 20 Hz raw data for pressure analyzer settings into 4 min block averaged periods. To this end, the configuration file (see chapter 3.1) was changed accordingly and the density correction for open-path instruments (Webb et al., 1980) was switched off. The results of this routine were then read into the open source statistical software *R* (version 4.0.3), along with the 20 Hz raw data of the soil station measurement site and the 4 m height station. This is, where the main processing took place. The pressure variance ( $\overline{p'p'}$ ) was calculated for each of the averaged 4 min intervals. The  $\overline{p'p'}$  data was then prefiltered according to its 95th percentile, such that only the highest 5 % of the data remained. Since the pressure pumping phenomenon is expected to yield high pressure fluctuations in the collected data, this criterion aims at a more specified data analysis for the objective of the presented thesis. In a next step, the raw data at both stations was filtered so that every 30 min period of 20 Hz data which contained at least one of the remaining 4 min prefiltered data points was chosen for the pressure pumping analysis. Table 3.2 shows the variables selected for the further processing.

Table 3.2.: Variables selected for the further pressure pumping analysis processing

Variables	Limits (IN- TRAMIX)	Limits (LOeWE)	Criteria for forced limits (INTRAMIX)	Criteria for forced limits (LOeWE)
<i>Time</i>	[27.05.2016 02:30:00; 12.07.2016 01:30:00]	[25.08.2020 11:30:00; 27.10.2020 08:30:00]	-	-
$w_{\text{soil}}$ [ $ms^{-1}$ ]	[-1.62; 1.16]	[-3.15; 2.81]	-	-
$p_{\text{soil}}$ [ $hPa$ ]	[912.40; 936.21]	[903.44; 938.26]	-	-
$CO_2$ soil [ $mmolm^{-3}$ ]	[0; 30]	[0; 30]	98th percentile	98th percentile
$T_{\text{s soil}}$ [ $^{\circ}C$ ]	[9.29; 37.89];	[0.05; 22.33]	-	-
$w_{4m}$ [ $ms^{-1}$ ]	[-2; 2]	[-1; 1]	99th percentile	98th percentile
$p_{4m}$ [ $hPa$ ]	[911.98; 935.77]	[902.96; 937.81]	-	-
$CO_2$ 4m [ $mmolm^{-3}$ ]	-	[0; 30]	-	98th percentile
$T_{\text{s 4m}}$ [ $^{\circ}C$ ]	[6.63; 35.00];	[1.00; 27.00]	99.999 per- centile	Percentiles: [0.1; 99.999]
$u_{4m}$ [ $ms^{-1}$ ]	[-10.00; 10.00]	[-3.04; 5.76]	Percentiles: [0.03; 99.99]	-
$v_{4m}$ [ $ms^{-1}$ ]	[-10.00; 10.00]	[-7.32; 6.79]	Percentiles: [0.03; 99.95]	-

As a consequence of prefiltering for the highest 5 % of pressure variances, the time series were no longer continuous. In fact the focus was shifted towards the daytime data (see Fig. 3.1). This was to be expected as it coincides with times of intense solar radiation, which give rise to enhanced buoyancy forces, strong pressure gradients and therefore higher pressure variances (Thomas and Foken, 2007; Flechard et al., 2007). A pronounced representation of the daytime data becomes especially apparent for the INTRAMIX campaign. For the LOeWE campaign, the remaining data was generally more uniformly distributed throughout the diurnal course and shows only a slight tendency towards midday.

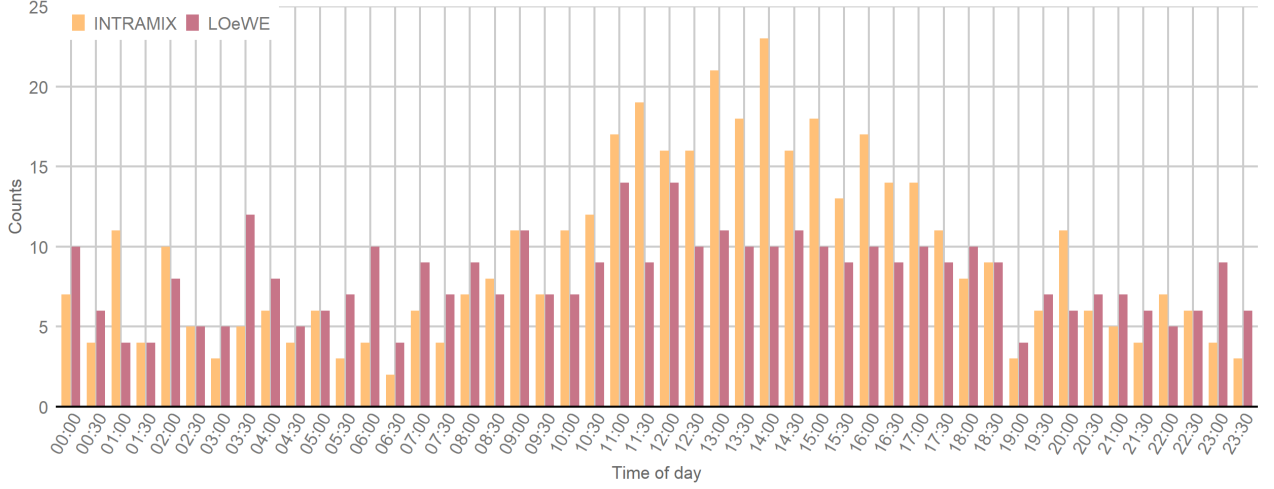


Figure 3.1.: Diurnal distribution of the remaining data after filtering. The histogram shows the distribution of each filtered 30 min averaged period of raw data (INTRAMIX: total of 445 periods, LOeWE: total of 388 periods) over a diurnal course for the INTRAMIX campaign (yellow) and LOeWE campaign (red).

In order to differentiate between the flow modes and time scales introduced in Chapter 1 (see Fig. 1.3), a triple decomposition was performed following Hussain and Reynolds (1970). The presented thesis distinguishes between a synoptic mean flow ( $\text{Syn}_{\text{mean}}$ ) and a synoptic perturbation ( $\text{Syn}_{\text{prime}}$ ) with an averaging period of 30 min (see Equ. 3.1 and 3.2). Whilst  $\text{Syn}_{\text{mean}}$  equals the 30 min averaging periods ( $\overline{X}_{30\text{min}}$ ) (INTRAMIX: total count of 445 data points, LOeWE: total count of 388 data points), the synoptic perturbation subtracts the mean of the whole of the raw data ( $\overline{X}_{\text{all raw}}$ ) from  $\overline{X}_{30\text{min}}$ . The thesis moreover mathematically defines coherent structures (CS) as the difference between every 30 s averaging period ( $\overline{X}_{30\text{s}}$ ) and the 30 min mean data ( $\overline{X}_{30\text{min}}$ ) (see Equ. 3.3), yielding a perturbation time scale for CS of 30 s (also see Thomas and Foken (2007)). The background turbulence (BT) has a perturbation time scale equal to the raw data (20 Hz), as every raw data point ( $X_{\text{raw}}$ ) gets subtracted by the 30 s averaging period ( $\overline{X}_{30\text{s}}$ ) it falls into (see Equ. 3.4).

$$\overline{X}_{\text{Syn}} = \overline{X}_{30\text{min}} \quad (3.1)$$

$$X'_{\text{Syn}} = \overline{X}_{30\text{min}} - \overline{X}_{\text{all raw}} \quad (3.2)$$

$$X'_{\text{CS}} = \overline{X}_{30\text{s}} - \overline{X}_{30\text{min}} \quad (3.3)$$

$$X'_{\text{BT}} = X_{\text{raw}} - \overline{X}_{30\text{s}} \quad (3.4)$$

Equation 3.1 to 3.4 were respectively applied to the variables  $w_{\text{soil}}$ ,  $w_{4\text{m}}$ ,  $CO_{2\text{ soil}}$ ,  $CO_{2\text{ 4m}}$ ,  $p_{\text{soil}}$  and  $p_{4\text{m}}$  (see Table 3.2). Additionally, the sonic temperatures ( $T_{\text{s soil}}$  and  $T_{\text{s 4m}}$ ) for each time scale ( $\text{Syn}_{\text{mean}}$ ,  $\text{Syn}_{\text{prime}}$ , CS and BT), as well as a vertical- ( $w_{4\text{m}}$ ), along- ( $u_{4\text{m}}$ ) and

cross-wind ( $v_{4m}$ ) component were calculated from the means of the raw data according to the time scale's averaging and perturbation time. Subsequently, the effective wind speed ( $U_{4m}$ ) for the synoptic time scales and the coherent structures was calculated after Equation 3.5.

$$U_{4m} = \sqrt{u_{4m}^2 + v_{4m}^2 + w_{4m}^2} \quad (3.5)$$

A categorization into weak-wind and strong-wind regimes was performed for both campaigns. To this end, a weak-wind threshold of  $0.6 \text{ m s}^{-1}$  determined in Wunder (2017) and Ehrnsperger (2017) was adopted for the INTRAMIX data. The same threshold of  $0.6 \text{ m s}^{-1}$  could be found for the LOeWE campaign 4 m station by plotting the 4 min averaged friction velocity ( $\overline{u}_*$ ) over the 4 min averaged effective wind speed ( $\overline{U}$ ) (see Fig. 3.2). Here, a quality control of the data was performed prior to the weak wind-analysis by excluding data of precipitation events and quality flags  $\geq 2$ . The post field-data quality control was carried out after Foken et al. (2004), who assign high quality data including good integral turbulence characteristics for fundamental research to the classes 1 and 2 out of nine. The stronger increase of  $\overline{u}_*$  with  $\overline{U}$  at approximately  $0.6 \text{ m s}^{-1}$  marks the weak-wind threshold for the LOeWE campaign.

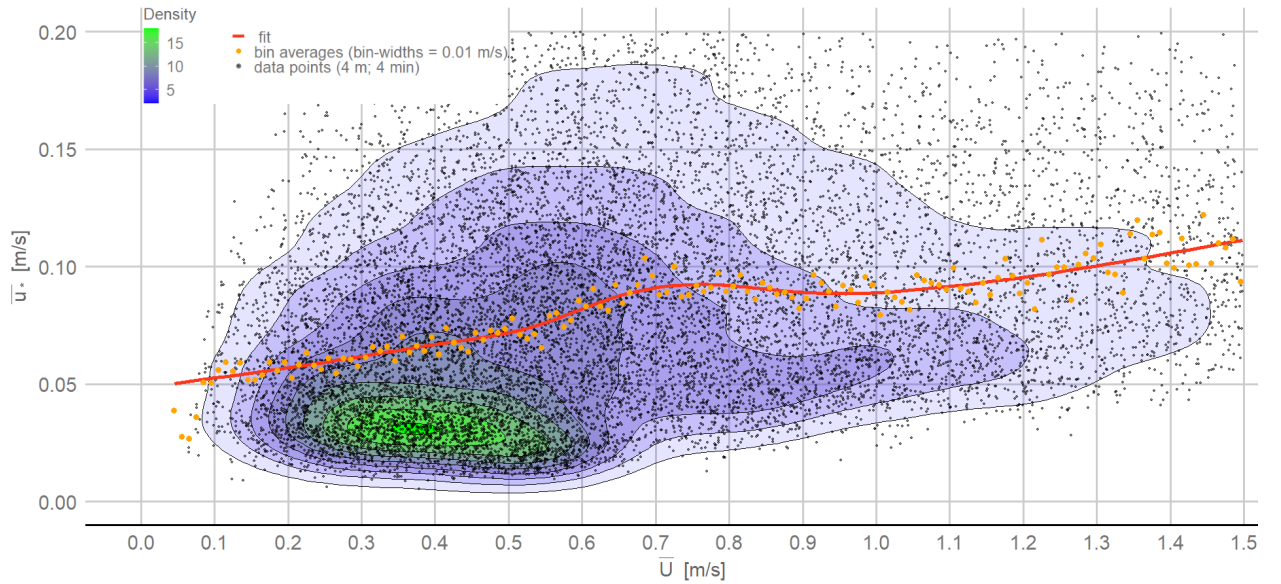


Figure 3.2.: Weak-wind threshold for the LOeWE campaign. Data of precipitation events and quality flags  $\geq 2$  (lower quality (Foken et al., 2004)) were excluded. Black points represent the 4 min averaged measurement values of the 4 m station data. The density of the data points increases with the color scale from light purple to deep green. The orange points are bin averages with a constant bin-width of  $\Delta \overline{U} = 0.01 \text{ m s}^{-1}$ . The mean fit was created by cubic spline regression.

The weak-wind threshold categorization was applied to the CS data set. This resulted in 64 % of the INTRAMIX CS data and 70 % of the LOeWE CS data being attributed to strong-wind (INTRAMIX CS weak-wind: 36 %; LOeWE CS weak-wind: 30 %). For the  $\text{Syn}_{\text{mean}}$  and the  $\text{Syn}_{\text{prime}}$  data, a 30 min interval was marked as weak-wind, whenever more

weak-wind occurrences than strong-wind occurrences of CS wind regimes were noted within one Syn 30 min interval. The labeling for Syn strong-wind events was carried out accordingly. Furthermore, a time of day index was created for all four data sets of  $\text{Syn}_{\text{mean}}$ ,  $\text{Syn}_{\text{prime}}$ , CS and BT. The index differentiates between transition time, daytime and nighttime as shown in Table 3.3.

Table 3.3.: Time of day index for the data sets Syn, CS and BT

Time of day	Limits
Transition time	[6:00:00; 10:00:00] and [18:00:00; 22:00:00]
Daytime	]10:00:00; 18:00:00[
Nighttime	]22:00:00; 06:00:00[

The main analysis for the pressure pumping phenomenon was realized employing the quadrant analysis technique (Wallace et al., 1972; Lu and Willmarth, 1973; Shaw et al., 1983). This technique is considered as the method of choice in the search for an empirical relationship between the critical parameters  $w$ ,  $p$  and  $CO_2$ . The quadrant analysis method uses a scatter plot of two flow variables  $x$  and  $y$  in a two-dimensional plane and was deployed before by Thomas and Foken (2007) in order to estimate coherent exchange at the Waldstein site. The Cartesian axes of the scatter plot define four quadrants Q1 ( $x > 0$ ,  $y > 0$ ), Q2 ( $x < 0$ ,  $y > 0$ ), Q3 ( $x < 0$ ,  $y < 0$ ), Q4 ( $x > 0$ ,  $y < 0$ ) (see Fig. 3.3).

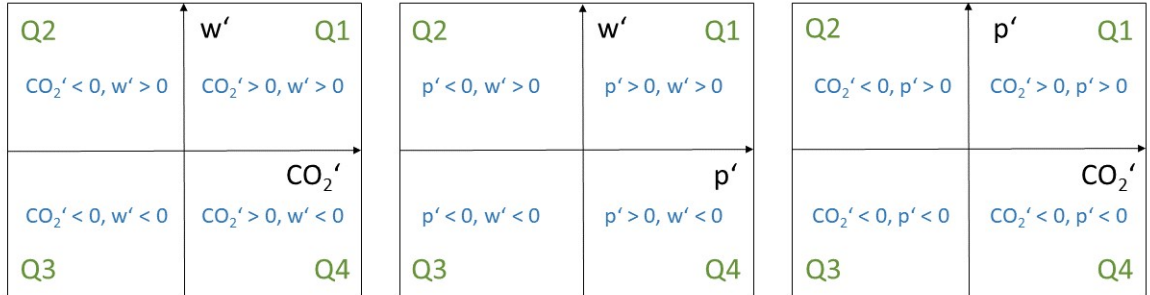


Figure 3.3.: Schematic sketch for the quadrant analysis technique. The relevant flow variables are shown in black, the four quadrants are written in green and the mathematical meaning of the variables in each of the four quadrants is defined in blue.

In preparation for the quadrant analysis  $w_{\text{soil}}'$ ,  $w_{4m}'$ ,  $CO_{2 \text{ soil}}'$ ,  $CO_{2 \text{ 4m}}'$ ,  $p_{\text{soil}}'$  and  $p_{4m}'$  of the  $\text{Syn}_{\text{prime}}$ , CS and BT data sets were each normalized by the 30 min period standard deviation of the raw data they fall in to. The quadrant analysis was then applied to the respective normalized variables for  $\text{Syn}_{\text{prime}}$ , CS and BT, categorized into daytime, nighttime, transition



time, weak-wind and strong-wind and color-coded by temperature and an additional kernel density distribution. However, these overview plots were deemed inappropriate to show any clear correlations or physical interdependencies between the parameters, and will therefore not be further analyzed or discussed in Chapter 4.3. Subsequently, the quadrant analysis method was performed on the CS data set for every available 30 min time period, resulting in a total of 445 CS quadrant plots for the INTRAMIX campaign and 388 plots for the LOeWE campaign. The focus was hereby shifted towards the correlation of  $p_{\text{soil}}'$  and  $CO_{2\text{ soil}}'$ , such that a categorization by quadrants was performed for every CS 30 min period  $p_{\text{soil}}' - CO_{2\text{ soil}}'$  plot. Specifically, this was based on a kernel density observation and by a visual screening regarding the position of the density center (Q1, Q2, Q3 and Q4) for each of the resulting plots. The quadrant analysis was then applied to the CS  $p_{\text{soil}}' - CO_{2\text{ soil}}'$  data and the  $w_{\text{soil}}' - p_{\text{soil}}'$  in accordance with this categorization. Additionally a test for dominant wind-regimes and times of day within these categories was realized in form of a histogram.

## 4. Results and Discussion

In order to address the four research questions proposed in Chapter 1, a *flux analysis*, *time series analysis* and *quadrant analysis* was performed. Respective bulk studies and case studies for the INTRAMIX and LOeWE campaign will be given in conjunction with each section. For the sake of comparability, the case studies are respectively set for three days each (INTRAMIX: 09.07.2016 00:00:00 to 12.07.2016 00:00:00; LOeWE: 26.08.2020 00:00:00 to 29.08.2020 00:00:00), whereas the bulk studies will span the entire experimental period.

### 4.1. Flux Analysis

The analysis of the physical environment including transfer of heat, water vapor and CO<sub>2</sub> at the soil station measurement site is crucial for the pressure pumping discussion. Knowing that sensible heat is a driver for buoyancy and thereby turbulence in the atmosphere (Monin and Obukhov, 1954) it was hypothesized, that varying buoyancy forces during a diurnal course will impact the strength of the pressure pumping phenomenon significantly (see H<sub>4</sub> Chapter 1). Figures 4.1 and 4.2 show the dependency between the CO<sub>2</sub> flux ( $\overline{w'CO_2'}$ ) and the pressure variance ( $\overline{p'p'}$ ) as well as the time series of the CO<sub>2</sub> flux, sensible heat flux ( $Q_H$ ) and latent heat flux ( $Q_{LE}$ ) over the entire period of the LOeWE experiment for the 4 m station (Fig. 4.1) and the soil station measurement site (Fig. 4.2). Note, that the data has not yet been filtered for the highest 5 % of pressure variance at this point of the analysis.

Despite the fact that only times of high  $\overline{p'p'}$  will be of interest for the pressure pumping analysis, it can be shown that most of the data points originally experience low pressure variances at both stations. The distribution of high to low  $|\overline{w'CO_2'}|$  occurs equally at both ends of the  $\overline{p'p'}$  spectrum. Generally the  $|\overline{w'CO_2'}|$  at the soil station appears to be higher than the one for the 4 m station. This becomes apparent for both the  $\overline{p'p'}$  and time dependent CO<sub>2</sub> flux plots. It can be presumed that soil respiration directly at the ground level plays a major role for this observation, leading to an enhanced CO<sub>2</sub> flux at the soil station. The 4 m station however is further removed from the source of CO<sub>2</sub>. Even though multiple studies (Subke and Tenhunen, 2004; Humphreys et al., 2003; Launiainen et al., 2005) found a seasonal dependency of the highest CO<sub>2</sub>,  $Q_H$  and  $Q_{LE}$  fluxes occurring during the warmer summer months, no such correlation could be seen in Figur 4.1 and 4.2. Since the measurement period only spanned three months, annual patterns could not be captured. Additionally it was found that precipitation seems to reduce the quality of the data owing to sensor sensibility. During the 30th of August, 25th of September as well as the 6th to 7th, 14th to 16th and 28th to 31st of October for instance, precipitation events fall together with high fluctuations of CO<sub>2</sub>, sensible heat and latent heat flux. Moreover, the increased water

availability shortly after and during precipitation periods can be presumed to offer ideal conditions for microorganisms as well as plant roots, acting to enhance soil respiration (see Matteucci et al. (2000)). A high water availability coupled with warm temperatures, would additionally result in an increase of  $Q_{LE}$  through enhanced evapotranspiration.

A similar figure to Figs. 4.1 and 4.2 (LOeWE campaign) was generated for the INTRAMIX campaign (see Fig. B.1). As stated in Chapter 2.2 there was no gas analyzer installed at 4 m height during the INTRAMIX experiment. Consequently, a calculation of  $Q_{LE}$  and  $\overline{w'CO_2'}$  could not be performed and no flux analysis is shown in the presented thesis at 4 m for the INTRAMIX campaign.

Due to the low resolution of data on a time span of almost ten weeks, it is difficult to identify any diurnal dependencies in Figs. 4.1 and 4.2. This is why a statistical analysis for the entire time period of both experiments was performed showing the hourly behaviour of  $\overline{w'CO_2'}$ ,  $Q_H$  and  $Q_{LE}$  over a diurnal course (see Fig. 4.3). Note, that positive values represent fluxes directed away from the surface whilst negative values indicate fluxes towards the surface.

When analyzing Fig. 4.3, it can be seen that the INTRAMIX data (soil station: yellow) shows a more pronounced variability in all three fluxes compared to the data of the LOeWE campaign (soil station: brow; 4 m station: blue). This might be due to higher soil and air temperatures together with an increase of VSMC during the INTRAMIX campaign (see Fig. 2.2 and 2.3 in Chapter 2.1) driving soil respiration and enhancing the  $CO_2$  fluxes in the sub-canopy. Most of the data from the LOeWE campaign is concentrated around zero for the sensible and latent heat flux and slightly above zero for the  $CO_2$  flux. The soil respiration which is directed away from the surface and into the atmosphere becomes the main driver for  $CO_2$  fluxes in the sub-canopy where vegetation is sparse and the photosynthesis rates are low. Interestingly, the boxes of the soil station and the 4 m station  $CO_2$  flux data shown in Fig. 4.3 for the LOeWE campaign shift against each other in a daily course. During nighttime, the  $CO_2$  flux at the soil station is higher than the  $CO_2$  flux at the 4 m station, but becomes lower and for some parts even negative during the mixing period at around midday, indicating an uptake of  $CO_2$  directly at the ground. This was not anticipated, and was not discernible from Figs. 4.1 and 4.2. However, it can be explained by the uptake of  $CO_2$  due to photosynthesis of grasses and moses in direct vicinity to the soil station measurement instruments. It is likely, that this understorey vegetation dominates the flux signal during the day at the soil station site to some extent. Conversely, the 4 m station site picks up a more mixed signal of soil respiration and sparse vegetation signals with a larger footprint in general, resulting in a more positive net flux at midday.

During both, the LOeWE and INTRAMIX campaign, the sensible and latent heat flux in Fig. 4.3 show a clear diurnal course of low flux variability around  $0 \text{ W m}^{-2}$  at night and an increased flux variability during the day. The daytime heat fluxes are mostly positive, indicating the surface to be an energy source for the above air and demonstrating an evaporation of water near the ground during times of higher solar irradiation. In contrast, the nighttime  $Q_H$  and  $Q_{LE}$  tend to be more negative. The upper soil layer cools down more

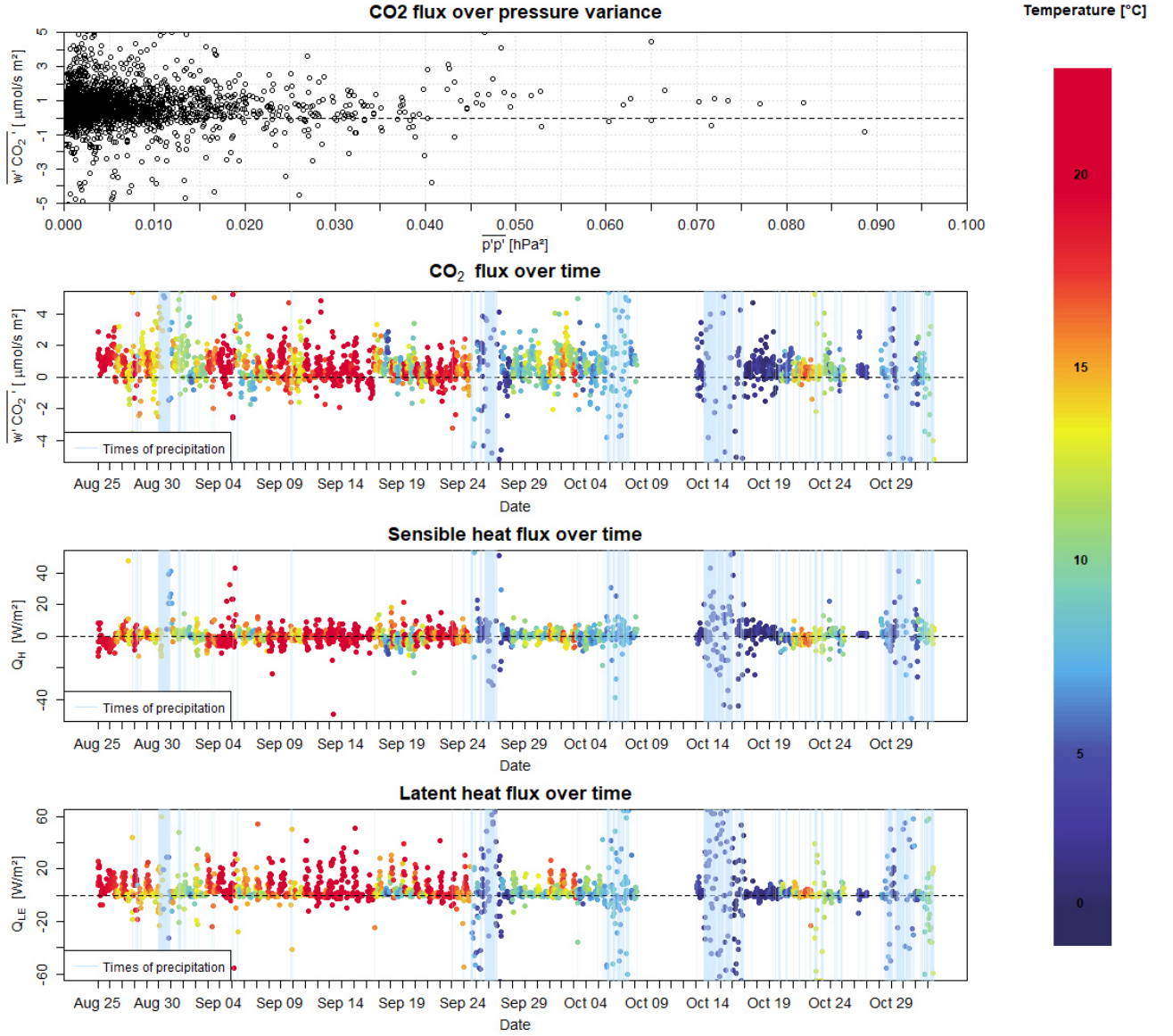


Figure 4.1.: Flux analysis overview plot for the 4 m station measurement site of the LOeWE campaign with an averaging period of 30 min. Dependencies between the CO<sub>2</sub> flux ( $\overline{w'CO_2'}$ , 95th percentile within plausibility limits:  $2.4 \mu\text{mol s}^{-1} \text{m}^{-2}$ ) and pressure variance ( $\overline{p'p'}$ ) (first plot) as well as the time series of the CO<sub>2</sub> flux (second plot), sensible heat flux ( $Q_H$ ) (third plot) and latent heat flux ( $Q_{LE}$ ) (fourth plot) are provided for the entire period of the LOeWE experiment. The time series are color-coded by temperature and marked with blue vertical lines during precipitation events.

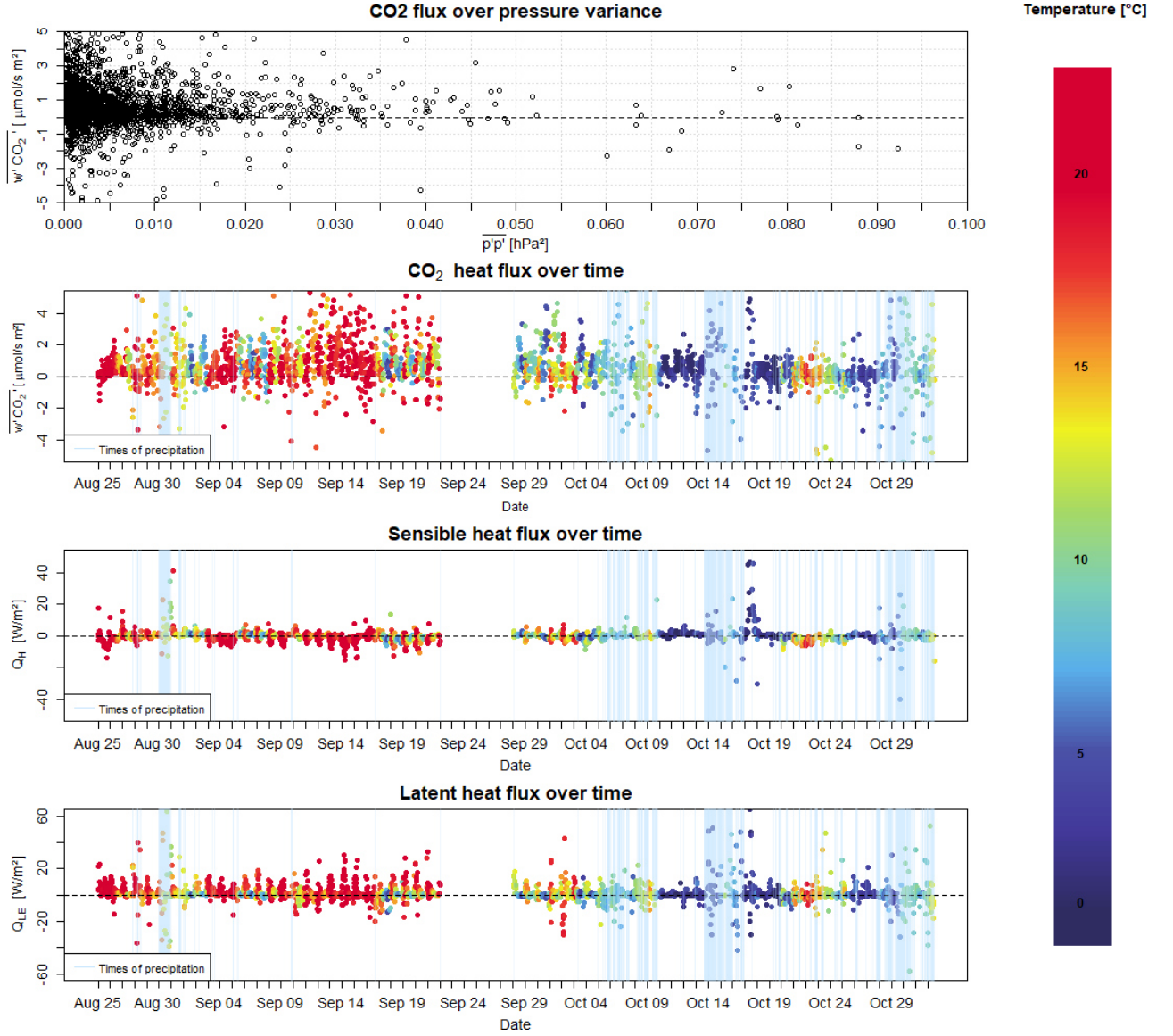


Figure 4.2.: Flux analysis overview plot for the soil station measurement site of the LOeWE campaign with an averaging period of 30 min. Dependencies between the CO<sub>2</sub> flux ( $\overline{w'CO_2'}$ , 95th percentile within plausibility limits:  $2.7 \mu\text{mol s}^{-1} \text{m}^{-2}$ ) and pressure variance ( $\overline{p'p'}$ ) (first plot) as well as the time series of the CO<sub>2</sub> flux (second plot), sensible heat flux ( $Q_H$ ) (third plot) and latent heat flux ( $Q_{LE}$ ) (fourth plot) are provided for the entire period of the LOeWE experiment. The time series are color-coded by temperature and marked with blue vertical lines during precipitation events.

efficiently than the above air during times of low or no solar radiation leading to an energy flux directed towards the surface. A negative latent heat flux results in condensation often present in the forms of fog or dew fall directly at the forest ground. Occasional negative heat fluxes during the day are more likely related to mesoscale motions as well as sweeps and ejection phases, which can cause a directional change of fluxes during periods of high mixing. The heat fluxes at the 4 m station mostly exceed the ones at the soil station by less than  $10 \text{ W m}^{-2}$ . These small errors might be the subjects of different separation distances in the application of the Moore correction (Moore, 1986). However, the median of the spectral frequency correction factor applied to the LOeWE data during the Moore correction did not significantly differ in magnitude between the soil station and the 4 m station ( $\text{frc}_{\text{corr } Q_H \text{ soil: } 1.029}$ ,  $\text{frc}_{\text{corr } Q_H \text{ 4 m: } 1.022}$ ,  $\text{frc}_{\text{corr } Q_{LE} \text{ soil: } 1.056}$ ,  $\text{frc}_{\text{corr } Q_{LE} \text{ 4 m: } 1.043}$ ). It could therefore be argued that site related differences like the amount of vegetation and shadowing between the soil station and the 68 m removed 4 m height main tower station are more likely to be responsible for the  $< 10 \text{ W m}^{-2}$  discrepancies mentioned above.

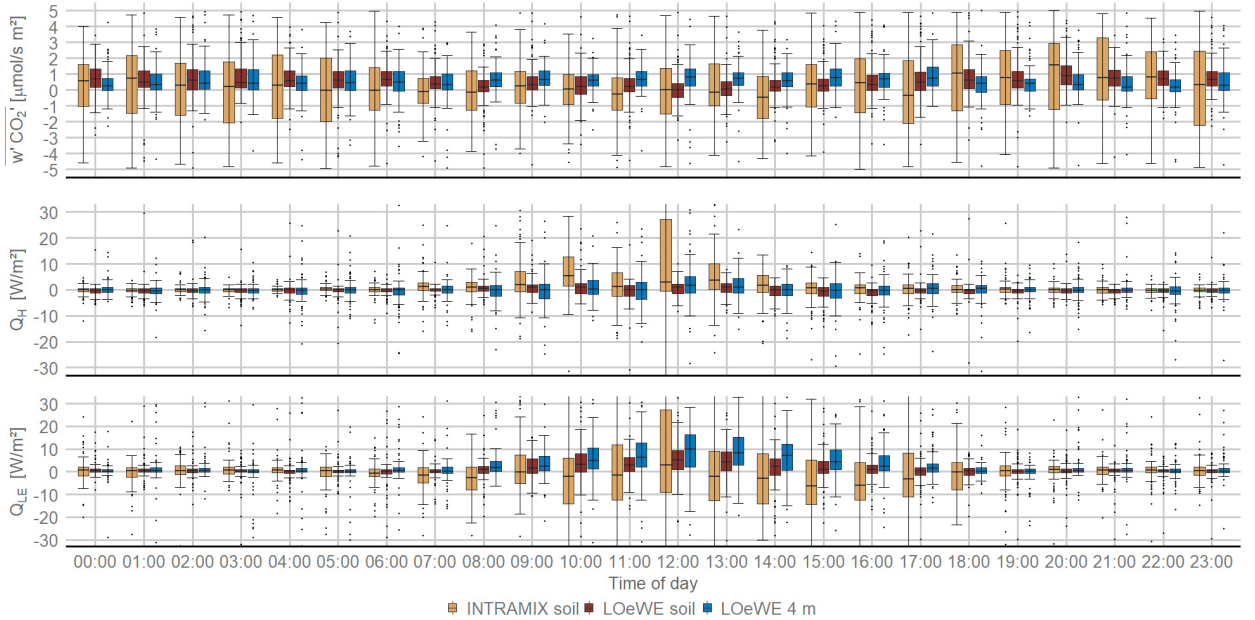


Figure 4.3.: Diurnal course of the  $\text{CO}_2$  flux (top), sensible heat flux (middle), and latent heat flux (bottom) for the INTRAMIX (soil station: yellow) and the LOeWE (soil station: brown; 4 m station: blue) experiment. The respective box-plots are fed with hourly data composed of 30 min averaging periods. The horizontal line within each box shows the 50th percentile of the hourly data, the upper border of the box presents the 75th percentile and the lower border gives the 25th percentile. The ends of the whiskers, respectively display the largest and smallest value within 1.5 times interquartile range above and below these borders. Black dots represent outside values  $> 1.5$  and  $< 3$  times the interquartile range beyond either end of the box.

Case studies for both campaigns were conducted. Their results generally agree with the findings of the statistical analysis and discussion of the diurnal courses of  $\overline{w'CO_2'}$ ,  $Q_H$  and  $Q_{LE}$  displayed in Fig. 4.3 and can be found in the appendices (see Fig. B.2, B.3 and B.4). The LOeWE case study, among other things, confirms the observation, that the 4 m station experiences more pronounced fluctuations of heat fluxes over a 24 hour period compared to the soil station site. An extensive flux variability coupled with temperatures around 30 °C at midday can also be ascertained for the INTRAMIX soil station case study (see Fig. B.4). This is in agreement with the previously discussed findings of generally more pronounced fluctuations within the INTRAMIX data compared to the LOeWE data.

The flux analysis is sufficient to outline the basic environmental conditions for the pressure pumping analysis. In this context, it was also important to show the relationship between the  $CO_2$  flux  $\overline{w'CO_2'}$  and the pressure variance  $\overline{p'p'}$  without the 95th percentile filter criterion for an unbiased overview of the pressure -  $CO_2$  flux interconnection. Moreover, the flux analysis presents first insights regarding hypothesis  $H_4$ . In a direct comparison between the INTRAMIX and LOeWE campaign in Fig. 4.3, it was shown that an intense solar radiation enhances fluxes around midday and during the warmer months of the year (see INTRAMIX). However, a further analysis is needed and provided in Chapter 4.3 in order to fully verify this observation.

## 4.2. Time Series Analysis

After a general data assessment of the environmental conditions and fluxes on an averaging period of 30 min in the previous chapters, the *time series analysis* aims to identify the time scales and time scale related flow modes sufficient to resolve the phenomenon of pressure pumping. In this regard, it was hypothesized that coherent structures covering time scales of 30 seconds will be dominating the pressure pumping phenomenon in terms of resolution and forcing (see  $H_1$  in Chapter 1). Furthermore, Shaw et al. (1990) and Böhm et al. (2013) found a high dependency of coherent structures on synoptic velocity and pressure fields.

In an effort to address this hypothesis, an analysis of the INTRAMIX and LOeWE data ( $w_{soil}$ ,  $w_{4m}$ ,  $CO_{2\ soil}$ ,  $CO_{2\ 4m}$ ,  $p_{soil}$  and  $p_{4m}$ ) was performed on three time scales, which give rise to the flow modes of synoptic mean, coherent structures and background turbulence (see Eqs. 3.1 to 3.4). As the main focus of this thesis lies on pressure fluctuations near the surface, the time series analysis of pressure during the INTRAMIX campaign (Fig. 4.4) and LOeWE campaign (Fig. 4.5) at the soil station (brown) and the 4 m station (blue) for the raw data, and flow modes of  $Syn_{mean}$ , CS and BT is shown in this chapter. A concurrent analysis of the vertical wind and  $CO_2$  concentrations can be found in the appendices (see C.1, C.2, C.3 and C.4). The data used in this part of the analysis was filtered for the highest 5 % of pressure variance according to the data processing explained in Chapter 3.2 and Fig. A.1. Resulting data gaps in the time series become apparent in Fig. 4.4, 4.5, C.1, C.2, C.3 and C.4.

The soil station data was overlaid with the 4 m station data in Fig. 4.4 and 4.5, such that

most of the soil station data points lie directly underneath the data points of the 4 m station. This indicates similar pressure patterns for both. The INTRAMIX as well as the LOeWE campaign show slightly higher pressure values ( $\overline{\Delta p} = 0.4 \text{ hPa}$ ) for the soil station compared to the 4 m station in the raw data and the 30 min averaged synoptic mean. This was to be expected, since air is a compressible fluid and atmospheric pressure typically decreases with increasing height. The 30 min averaged pressure along with the raw data demonstrate wave-like pressure fluctuations extending over several days. These low frequency waves in pressure can be attributed to large-scale weather patterns and the passage of fronts. During large-scale weather situations the pressure is generally stable for several days and varies more extensively between the troughs and ridges and during the passage of a front. A rapid decline in pressure directly at the ground level occurs when a warm front glides on top of a cold front or a cold front thrusts underneath a warm front. Both cases result in a fast air rising and condensation as well as the formation of a distinct high pressure area aloft and a low pressure area near the surface. In Fig. 4.4 and 4.5 these events are reflected as pressure minima during the 30 min averaged synoptic mean e.g. in the evening of the 29th of May, 16th of June and 25th of June during the INTRAMIX campaign and the 28th of August and 3rd of October during the LOeWE campaign. Moreover, the data yields drops in pressure on a synoptic scale accompanied by strong pressure fluctuations on the time scale of coherent structures. A correlation between the two time scales in relation to the pressure pumping phenomenon would be in agreement with the findings of Shaw et al. (1990) and Böhm et al. (2013) and needs to be analysed in more detail. The behavior of the background turbulence pressure on the other hand seems to be rather random with no clear dependencies on either of the other time scales.

When analyzing the time series for a period of only three days (see Figs. 4.6 and 4.7), the smooth low frequency wave-like motions of the synoptic time scale becomes even more apparent. In contrast to this, the coherent time scale shows very pronounced ramp shaped structures with maxima in its perturbation during the 11th of July at 18:00 (INTRAMIX: Fig. 4.6) and the 28th of August at 08:00 and 20:00 (LOeWE: Fig. 4.7). This again coincides with minima of the synoptic pressure. Compared to the background turbulence, the fluctuation patterns of the coherent structures are more consistent. The background turbulence exhibits phases of small to large fluctuations without any visible connection to the other time scales in varying temporal intervals.

The graphical observation, that strong CS pressure fluctuations are initiated by pressure minima on the synoptic time scale is in agreement with the findings of the existing literature (see Thomas et al. (2008), Shaw et al. (1990), Ruppert et al. (2006), Takle et al. (2003) and Böhm et al. (2013)) and hypothesis  $H_1$ . Therefore, a more detailed investigation into coherent structures as well as an analysis of the relationship between the 30 s time scale of coherent structures and the 30 min  $\text{Syn}_{\text{mean}}$  time scale appears to be most promising in order to meet the objective of this thesis.

To this end, the absolute value of stationarity (change of pressure over time) of the  $\text{Syn}_{\text{mean}}$  was calculated for every three continuous data points. The standard deviation of the CS



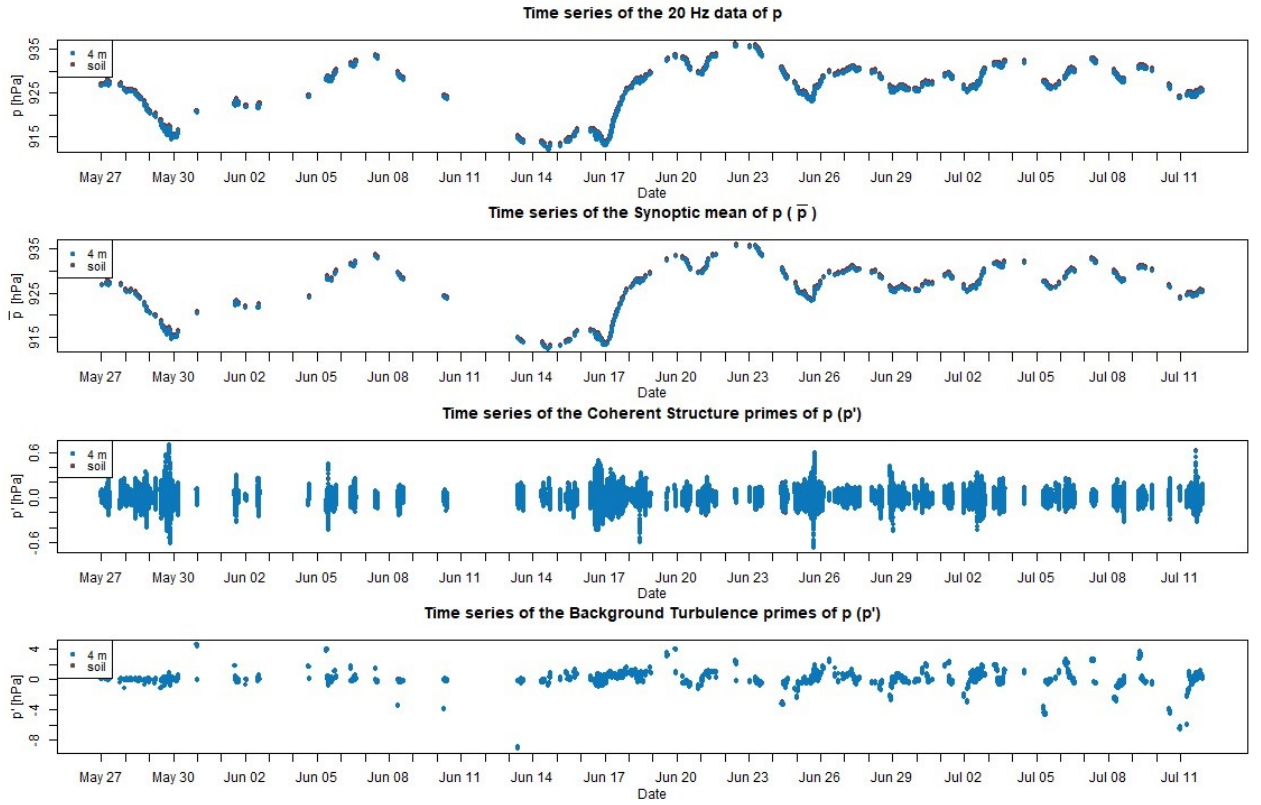


Figure 4.4.: Time series analysis of pressure during the INTRAMIX campaign, showing the raw data (20 Hz), synoptic mean (30 min), coherent structures (30 s) and back-ground turbulence (20 Hz) for the soil station (brown) and 4 m station (blue).

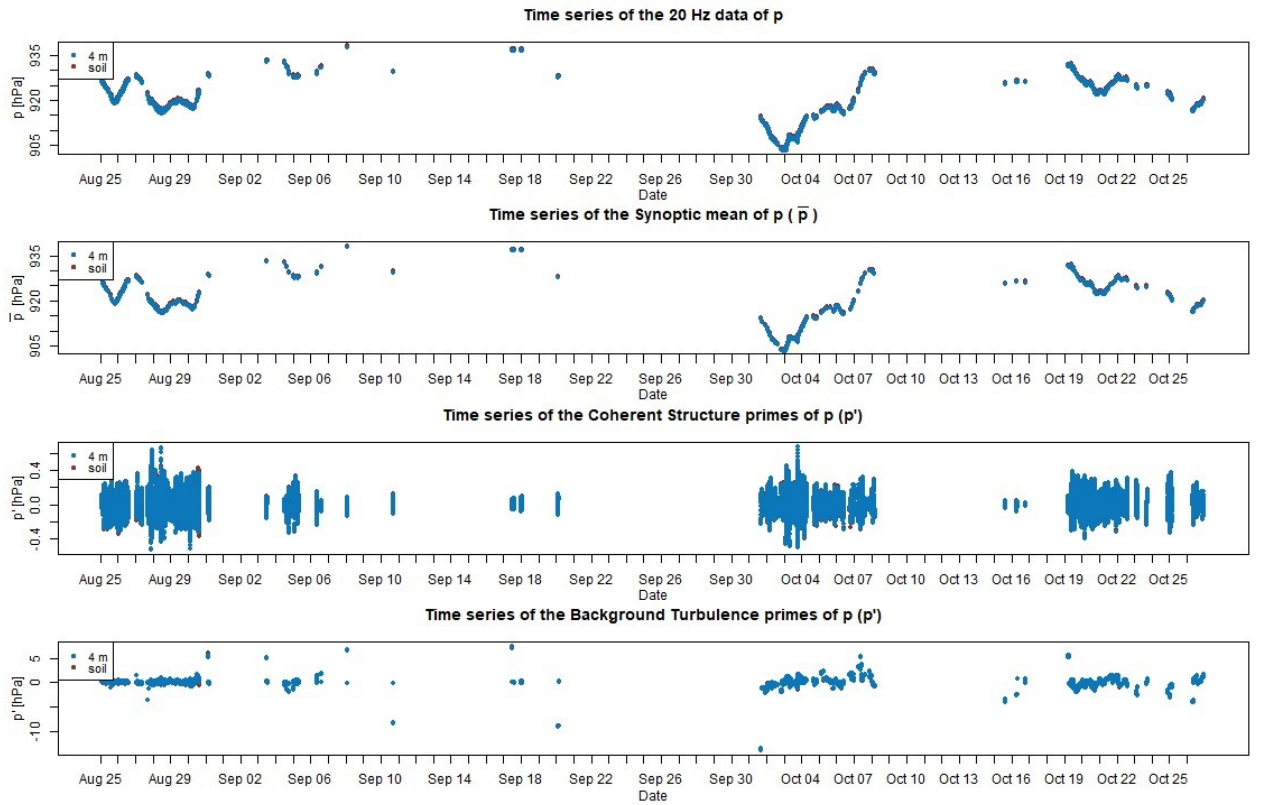


Figure 4.5.: Time series analysis of pressure during the LOeWE campaign, showing the raw data (20 Hz), synoptic mean (30 min), coherent structures (30 s) and background turbulence (20 Hz) for the soil station (brown) and 4 m station (blue).

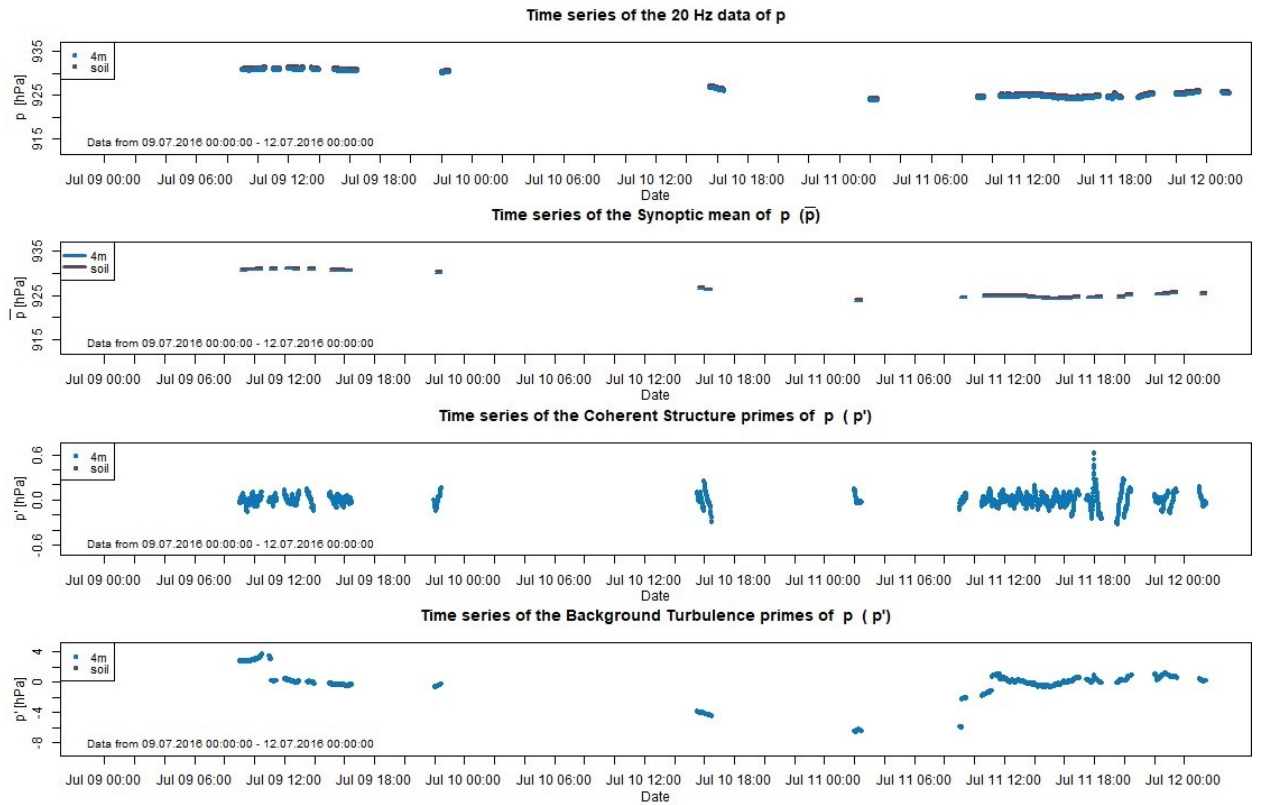


Figure 4.6.: Time series analysis case study of pressure during the INTRAMIX (top; 09.07.2016 00:00:00 to 12.07.2016 00:00:00) campaign, showing the raw data (20 Hz), synoptic mean (30 min), coherent structures (30 s) and background turbulence (20 Hz) for the soil station (brown) and 4 m station (blue).

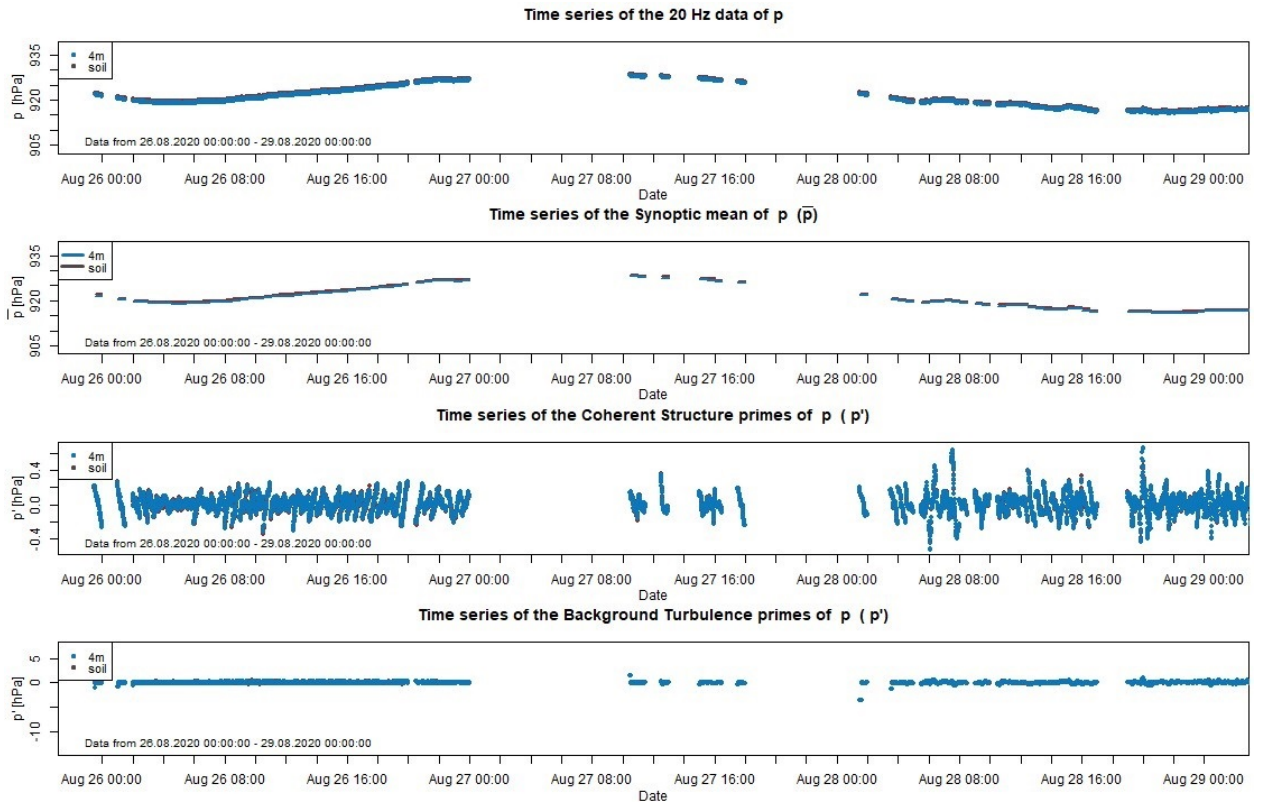


Figure 4.7.: Time series analysis case study of pressure during the LOeWE (bottom; 26.08.2020 00:00:00 to 29.08.2020 00:00:00) campaign, showing the raw data (20 Hz), synoptic mean (30 min), coherent structures (30 s) and background turbulence (20 Hz) for the soil station (brown) and 4 m station (blue).

data points for each of the respective 30 min intervals were then plotted against the resulting values of the  $\text{Syn}_{\text{mean}}$  stationarity (see Fig. 4.8). This approach was applied to the soil station and the 4 m station for both, the INTRAMIX and the LOeWE campaign. Additionally, a linear regression with the function  $y = 0.03 + 10.29$  (INTRAMIX) and  $y = 0.06 + 6.75$  (LOeWE) was fitted to the data. Given the fact, that for each campaign the data points of the 4 m station and soil station are nearly congruent, no station specific difference in their linear function can be determined within the chosen number of decimal digits.

Figure 4.8 shows a positive linear dependency of high  $\text{Syn}_{\text{mean}}$  stationarity values being accompanied by an increased standard deviation of CS pressure. This validates the observations from Fig. 4.4 and 4.5, where a dependency between drops in pressure on the synoptic time scale and an enhanced turbulent energy of coherent structures was already suspected. The strength of the correlation is best described in numbers by the coefficient of determination ( $R^2$ ),  $R^2 = 0.55$  (INTRAMIX) and  $R^2 = 0.41$  (LOeWE). This can be interpreted as approximately half of the data points falling within the regression line and a likelihood of around 50 % for a similar correlation during a concordant experiment in the future. The results suggest, that the pressure pumping phenomenon can most likely be observed on a CS time scale (30 s) during distinct drops in pressure on a synoptic time scale (30 min). Specifying the cumulative occurrences of enhanced soil-air gas exchanges through pressure pumping for the time frame of large-scale weather patterns (e.g. the passage of a front) can be an important step towards correcting the overestimation of NEE estimates.

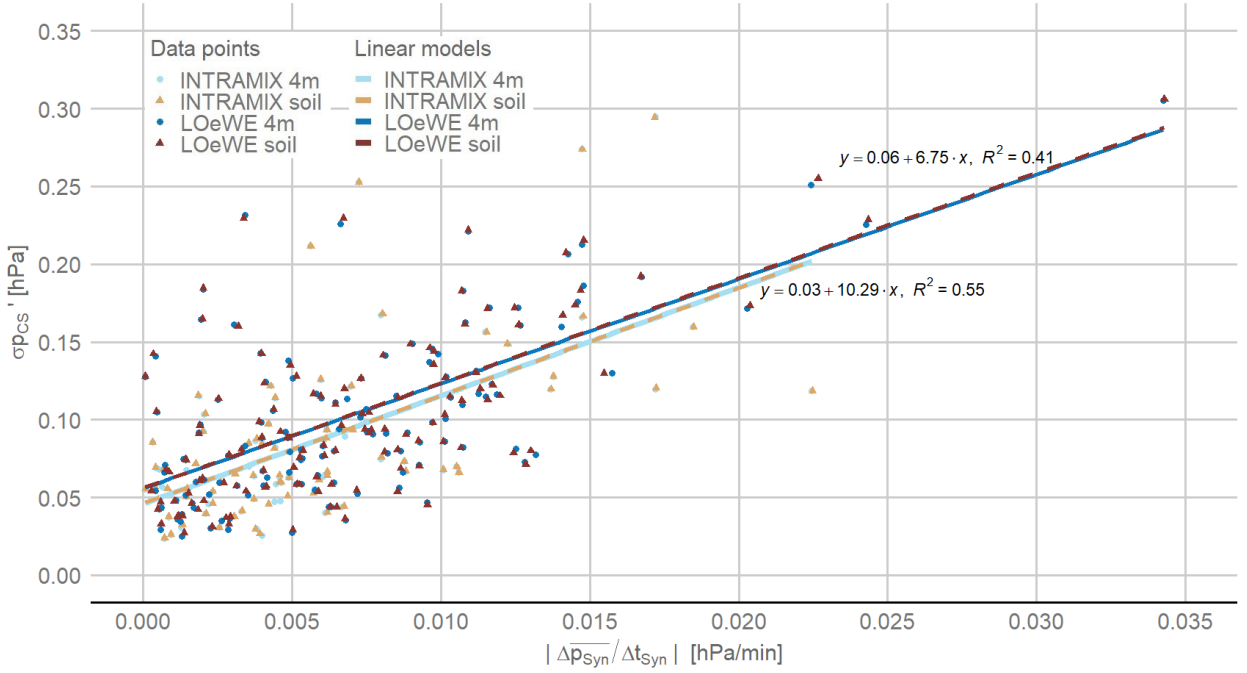


Figure 4.8.: Correlation between pressure on a synoptic and coherent structure time scale for the INTRAMIX (soil station: beige; 4 m station: light blue) and LOeWE (soil station: brown; 4 m station: dark blue) campaign. The x-axis shows the absolute value of stationarity for every three continuous data points on the  $\text{Syn}_{\text{mean}}$  time scale. The y-axis displays the standard deviation of the CS data points for the respective 30 min intervals. A linear regression model and the coefficient of determination are given for each station during the INTRAMIX and the LOeWE campaign.

### 4.3. Quadrant Analysis

Building on the findings of the *time series analysis* in the previous chapter, the pressure pumping analysis will be continued with a *quadrant analysis* on the time scale of coherent structures. This specifically relates to the research questions regarding the type of pressure dominating the system ( $\text{RQ}_2$ ) and the source area of air (stemming from the soil or sub-canopy) detected at the soil station measurement site ( $\text{RQ}_3$ ). Research question four ( $\text{RQ}_4$ ), which was already addressed in Chapter 4.1 will also be discussed in more detail.

The hypotheses connected to  $\text{RQ}_2$  and  $\text{RQ}_3$  ( $\text{H}_2$  and  $\text{H}_3$ ) can be best explained schematically with Fig. 4.9. It was stated, that based on the experimental setup with a built-in Quad-Disc probe, static pressure will be predominantly detected by the measurement system. Moreover, it was speculated that while there will be no source of air (stemming from the soil or sub-canopy) dominating over the other one during the entire experimental period, smaller time periods might show tendencies of upwards directed fluxes from the soil or downward directed

fluxes from the sub-canopy dependent on wind regimes and times of day. Figure 4.9 shows an exemplary quadrant analysis of  $p_{\text{soil}}'$  (y-axis) against  $CO_{2\text{ soil}}'$  (x-axis) and the processes presumably involved behind each quadrant (Q1, Q2, Q3 and Q4). The bold type writing describes the initiator of the fluxes in every quadrant, whereas the statements underneath characterize the resulting processes and their impact on the  $CO_2$  fluxes. Furthermore, the green writing states the type of pressure (static or dynamic) attributed to a certain quadrant. The fill color represents the source of air detected by the measurement instruments coming from the soil (brown) or the sub-canopy (blue). According to Fig. 4.9, high static pressure directly at the ground leads to an upward directed vertical wind and a positive  $CO_2$  flux from the soil into the atmosphere. These types of processes would be reflected by data points located in Q1 ( $CO_{2\text{ soil}}' > 0$ ,  $p_{\text{soil}}' > 0$ ). An accumulation of data points in Q2 ( $CO_{2\text{ soil}}' < 0$ ,  $p_{\text{soil}}' > 0$ ) can be attributed to a downward directed vertical wind resulting in an increase of dynamic pressure at the surface. Here, the air near the measurement instruments is depleted in  $CO_2$  due to the low  $CO_2$  signal from the sub-canopy. Conversely, Q3 ( $CO_{2\text{ soil}}' < 0$ ,  $p_{\text{soil}}' < 0$ ) indicates low static pressure at the ground, which initiates a vertical wind towards the surface in conjunction with a downward directed  $CO_2$  flux and  $CO_2$  depleted air signals recorded by the measurement instruments. Lastly, an upward directed vertical wind generates a decrease of dynamic pressure at the ground and leads to  $CO_2$  getting sucked out of the soil and into the air above. This process becomes evident as data points fall into Q4 ( $CO_{2\text{ soil}}' > 0$ ,  $p_{\text{soil}}' < 0$ ) of the correlation plot.

Since a relationship between the synoptic time scale and the coherent structure turbulence was already concluded from Chapter 4.2, the quadrant analysis method was performed on the CS data set for every available 30 min time period (see Chapter 3.2). The focus is hereby placed on the correlation of  $p_{\text{soil}}'$  with  $CO_{2\text{ soil}}'$  as displayed schematically in Fig. 4.9.

Tables 4.1 and 4.2 show in which quadrant the kernel density observations of the respective CS 30 min interval plots were centered for both the INTRAMIX and the LOeWE campaign. The location of this center was hereby assessed visually, such that the CS 30 min interval plots could each be sorted into one of twelve categories of Table 4.1 and 4.2. Multiple numbers in a column of the "Quadrant(s)" row indicate that the center of the kernel density observation spans over more than one quadrant. A "NA" entry was attributed to Table 4.1 with 4 counts. This is because of the filter criteria from Table 3.2 in Chapter 3.2, which results in an insufficient amount of data points for four of the generated plots. A kernel density observation becomes meaningless for these cases and a "NA" was assigned to the column.

A clear distinction between the quadrants with the center of the kernel density precisely falling into one of the four quadrants makes out 83 % of the INTRAMIX campaign and 80 % of the LOeWE campaign. It can be ascertained, from the amount of counts located in each of the four quadrants, that every scenario discussed in Fig. 4.9 comes into play in such a degree, that none of the quadrants can be discarded as underrepresented. A translation of the quadrant number back to the processes involved (see Fig. 4.9) leads to the compelling consequence, that static pressure is not the prevalent type of pressure



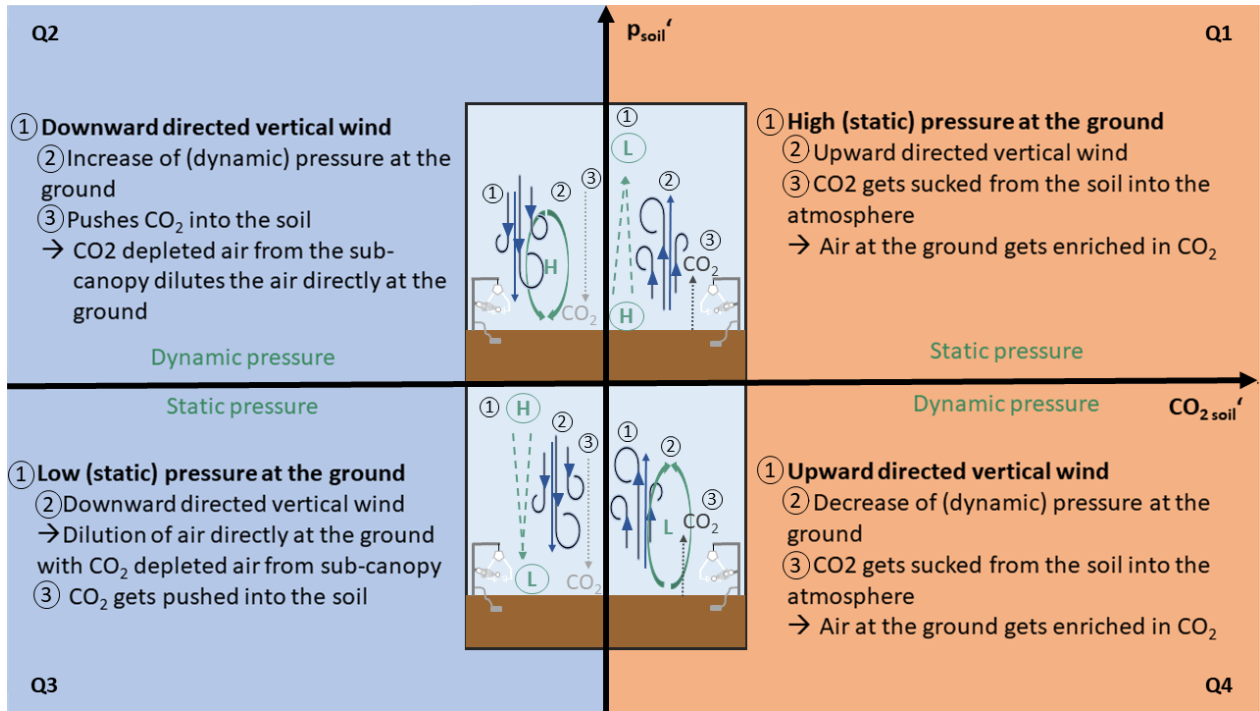


Figure 4.9.: Schematic figure of processes involved for each quadrant of a  $p_{soil}'$  (y-axis) -  $CO_{2,soil}'$  (x-axis) correlation plot. The bold type writing describes the initiator of the fluxes in every quadrant. The statements underneath characterize the resulting processes and their impact on the CO<sub>2</sub> fluxes. Two fill colors characterize the source of air detected by the measurement instruments coming from the soil (brown) or the sub-canopy (blue). The type of pressure attributed to the respective quadrants is given in green writing. The numbers in the schematic sketches indicate the chronological order of the processes involved in each Quadrant.

detected by the measurement system and hypothesis H<sub>2</sub> therefore needs to be rejected. With a total of 43 % (INTRAMIX) and 42 % (LOeWE) of the events focused on Q2 and Q4 as well as 43 % (INTRAMIX) and 41 % (LOeWE) of the cases centered in Q1 and Q3, the distribution between occurrences of dynamic or static pressure is equal. This result is somewhat surprising, since the inbuilt Quad-Disc probe of the pressure transducer has been proven to successfully eliminate the effects of dynamic pressure in the past (Liberzon and Shemer, 2010). Since the system was not designed for the exceptional conditions of a weak-wind boundary layer however, the differentiation between dynamic pressure and static pressure by the Quad-Disc probe might be limited in the sub-canopy. Additionally, the reliability of the employed pressure probe has been proven to decrease with an increasing angle  $\alpha$  (horizontal wind:  $\alpha = 0^\circ$ ; vertical wind:  $\alpha = 90^\circ$ ) (Wyngaard et al., 1994). The fact that the experimental setup of this thesis studies vertical pressure gradients might therefore add to the static pressure error of the instrument.

With regards to research question RQ<sub>3</sub>, which asks about the source of air detected by the



system, it becomes apparent from Table 4.1 and Table 4.2, that 62 % (INTRAMIX) and 48 % (LOeWE) of all cases can be allocated to Q2 and Q3. Based on Fig. 4.9 this is in agreement with a predominant occurrence of a downward directed flux from the sub-canopy towards the surface. Whilst the dependence on wind regimes, diurnal courses, soil properties and the behavior of sweeps and ejection of coherent structures remains to be further studied, it is true that the sub-canopy is the main source of air for most of the analyzed 30 min intervals. The first part of hypothesis H<sub>3</sub> can therefore be confirmed.

Table 4.1.: Quadrant analysis kernel density observation of  $p_{\text{soil}}'$  against  $CO_{2\text{ soil}}'$  for the INTRAMIX campaign

Quadrant(s)	1	2	3	4	1,2	1,3	1,4	2,3	2,4	3,4	2,3,4	NA
<b>Counts of 30 min periods</b>	53	126	128	62	11	7	8	22	6	17	1	4
<b>Percentage of total</b>	12%	28%	29%	14%	2%	2%	2%	5%	1%	4%	0%	1%

Table 4.2.: Quadrant analysis kernel density observation of  $p_{\text{soil}}'$  against  $CO_{2\text{ soil}}'$  for the LOeWE campaign

Quadrant(s)	1	2	3	4	1,2	1,3	1,4	2,3	2,4	3,4	1,2,4	1,2,3,4
<b>Counts of 30 min periods</b>	70	90	80	70	19	9	8	15	4	17	1	5
<b>Percentage of total</b>	18%	23%	21%	18%	5%	2%	2%	4%	1%	4%	0%	1%

In order to further analyze hypothesis H<sub>3</sub>, dependencies of temperature and wind regimes on the distribution of quadrants presented in Table 4.1 and 4.2 need to be identified. This can be realized by studying the normalized  $p_{\text{soil}}'$  (y-axis) -  $CO_{2\text{ soil}}'$  (x-axis) correlation plots as presented in Fig. 4.10, 4.11, 4.12 and 4.13. They were categorized after the first four columns of Table 4.1 and Table 4.2, in such ways that "Normalized CS primes (Quadrant 1)" represents all cases of column one, "Normalized CS primes (Quadrant 2)" shows all occurrences of column two, "Normalized CS primes (Quadrant 3)" displays the events of column 3 and "Normalized CS primes (Quadrant 4)" demonstrates all cases of column 4.

Figure 4.10 and 4.11 are color-coded by 30 s period temperatures and give additional information about the distribution of strong-wind and weak-wind events within each of the quadrants. The most apparent difference between Fig. 4.10 and 4.11 are the overall temperatures of the two campaigns, spanning from 9.4 °C to 34.1 °C for the INTRAMIX experiment

(Fig. 4.10), and from 0.2 °C to 21.4 °C for the LOeWE campaign (Fig. 4.11). This however seems not to affect the scattering of the data points and the shape of the kernel density distribution significantly since differences relating thereto are small at the most. It appears that Q3 experiences more warm data points than the other quadrants for both experiments. This could be due to a higher heat transfer in humid air near the plant canopy with warm air being pushed down by the CS sweep motions. The strong-wind events dominate over the weak-wind events for all quadrants. This was to be expected, since only the highest 5 % of pressure data was used for the analysis and a strong correlation between pressure and velocity signals was determined before by Shaw et al. (1990). Even though the relation between strong-wind and weak-wind is similarly distributed over the quadrants in Fig. 4.10 and 4.11, a small tendency towards stronger winds can be ascertained for Q1 and Q3. Together with the "warmer" data points in Q3, this indicates stronger forces sufficient to initiate and accelerate motion in Q3 compared to the others. Here, strong sweep motions presumably initiated by a low static pressure at the surface and a high static pressure at the top of the canopy (also see Chapter 4.2) lead to a fully coupled canopy (see Cs and C in Chapter 1) and bring air from the canopy down into the ground layer. It should be noted, that this thesis does not provide a renewed analysis of coupling regimes but refers back to the regimes proposed by (Thomas and Foken, 2007) (also see Chapter 1) in a general manner for the sake of the pressure pumping discussion. The coupling of the forest air with the sub-canopy and canopy as the primary source of air measured at the soil station seems to be dependent on strong-wind regimes and pronounced sweep motions. This is in agreement with the second part of hypothesis H<sub>3</sub>. Note, that Fig. 4.10 and 4.11 give the percentage of the relation between strong-wind and weak-wind occurrences within one quadrant. A more detailed analysis of the existing wind regimes for each quadrant related to the overall distribution of strong-wind and weak-wind events will be discussed at a later point.

In Figure 4.12 and 4.13, the categories (Q1, Q2, Q3, Q4) have been additionally filtered for wind regimes. The light green data points show the weak-wind percentage of the first four categories of Table 4.1 and Table 4.2, whilst the dark green color stands for the strong-wind events. The kernel density distribution for each plot of Fig. 4.12 and 4.13 is located in the exact quadrant of its respective category. This supports the categorization of Table 4.1 and Table 4.2, which seems to work very well even when splitting up the data for a more detailed analysis. Moreover, it becomes apparent that the strong-wind regimes are generally better correlated towards the categorization with a higher coefficient of determination  $R^2$ . This is true for all but Q2 where a stronger correlation of the weak-wind regime during the LOeWE campaign (4.13) can be observed. As a result one could argue that more precise directional processes like sweep and ejection phases can be mainly attributed to strong-wind events. During weak-wind occurrences in contrary, the vertical fluxes of pressure and CO<sub>2</sub> are less pronounced and might even be disturbed by molecular diffusion and horizontal advection as described in Fig. 1.1 (Thomas et al., 2013). It should be pointed out however, that the differences in the distribution of the data and  $R^2$  between strong-wind and weak-wind occurrences are marginal at the most. An interpretation without a further investigation can only be speculative at this point.

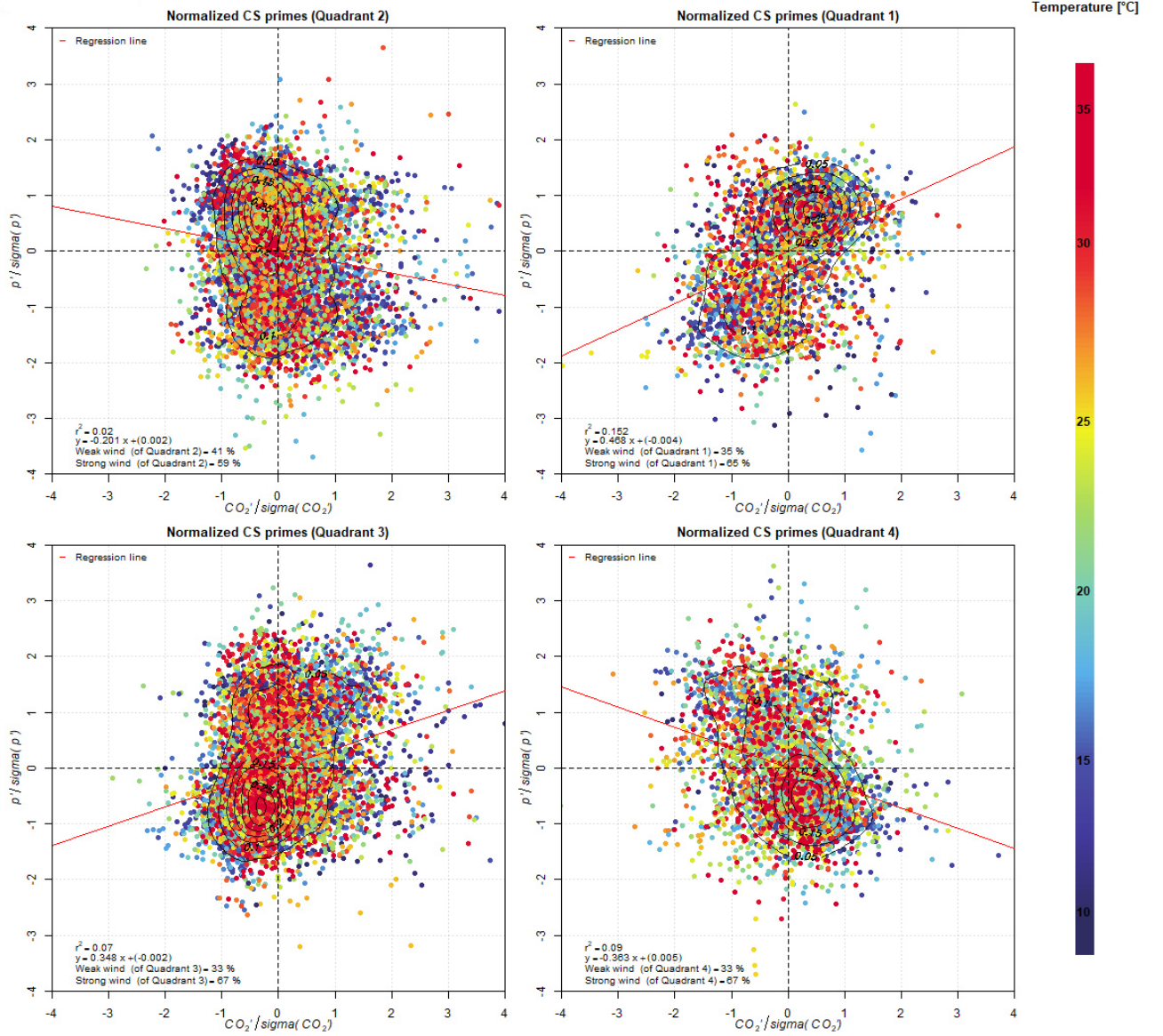


Figure 4.10.: Temperature dependent quadrant analysis of the normalized  $p_{\text{soil}}'$  (y-axis) -  $\text{CO}_2 \text{ soil}'$  (x-axis) correlation for the INTRAMIX campaign. The CS data was normalized by 30 min period standard deviation of the raw data they fall into and categorized according to the first four columns of Table 4.1. A regression line was drawn for each categorized quadrant and the information about its linear function, the coefficient of determination and the relation of weak-wind to strong-wind occurrences is given in the bottom left corner for the respective category. The data points are color-coded by temperature and additional kernel density lines for each subplot are displayed with identical isolines.

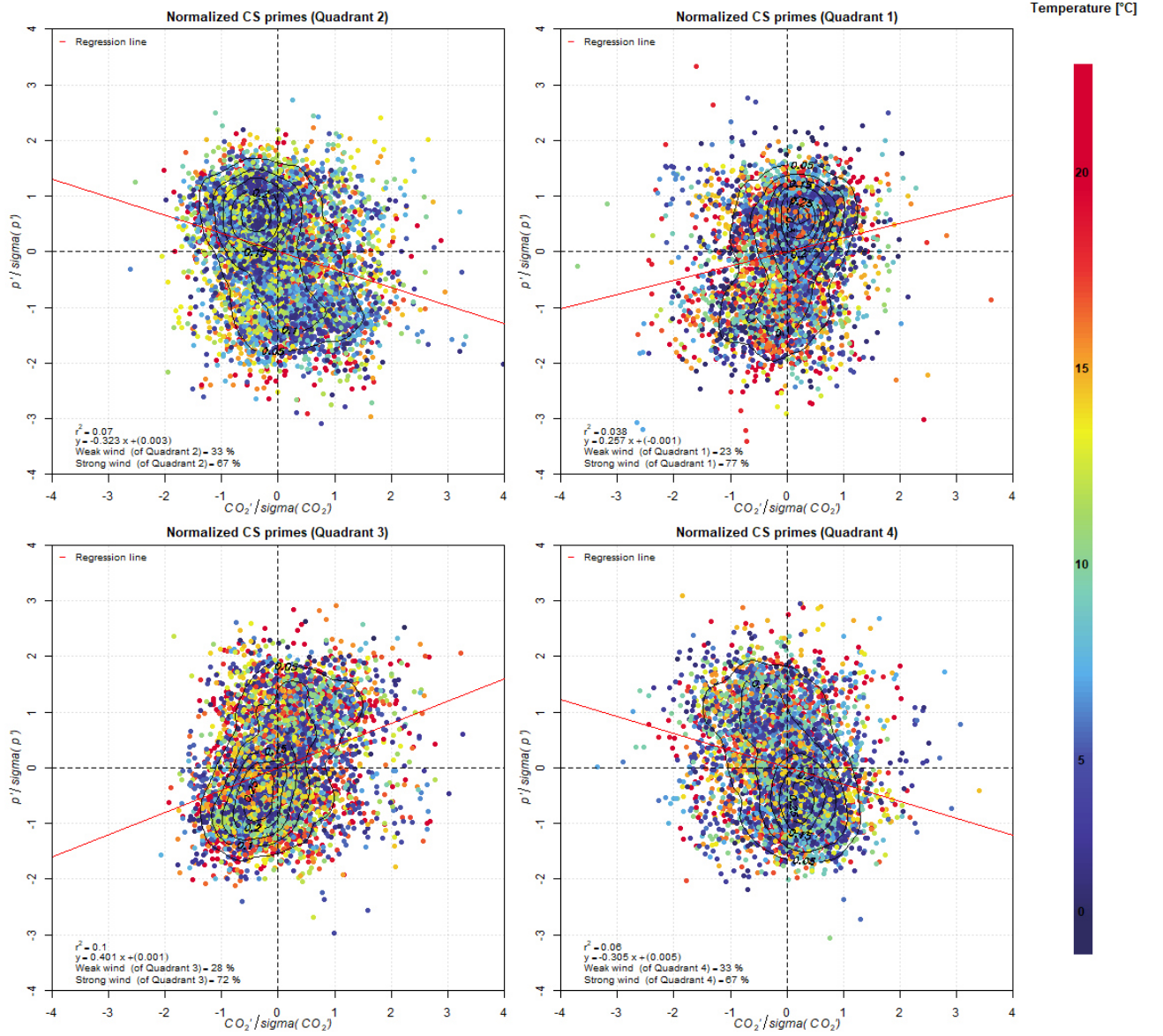


Figure 4.11.: Temperature dependent quadrant analysis of the normalized  $p_{soil}'$  (y-axis) -  $CO_{2,soil}'$  (x-axis) correlation for the LOeWE campaign. The CS data was normalized by 30 min period standard deviation of the raw data they fall into and categorized according to the first four columns of Table 4.2. A regression line was drawn for each categorized quadrant and the information about its linear function, the coefficient of determination and the relation of weak-wind to strong-wind occurrences is given in the bottom left corner for the respective category. The data points are color-coded by temperature and additional kernel density lines for each subplot are displayed with identical isolines.

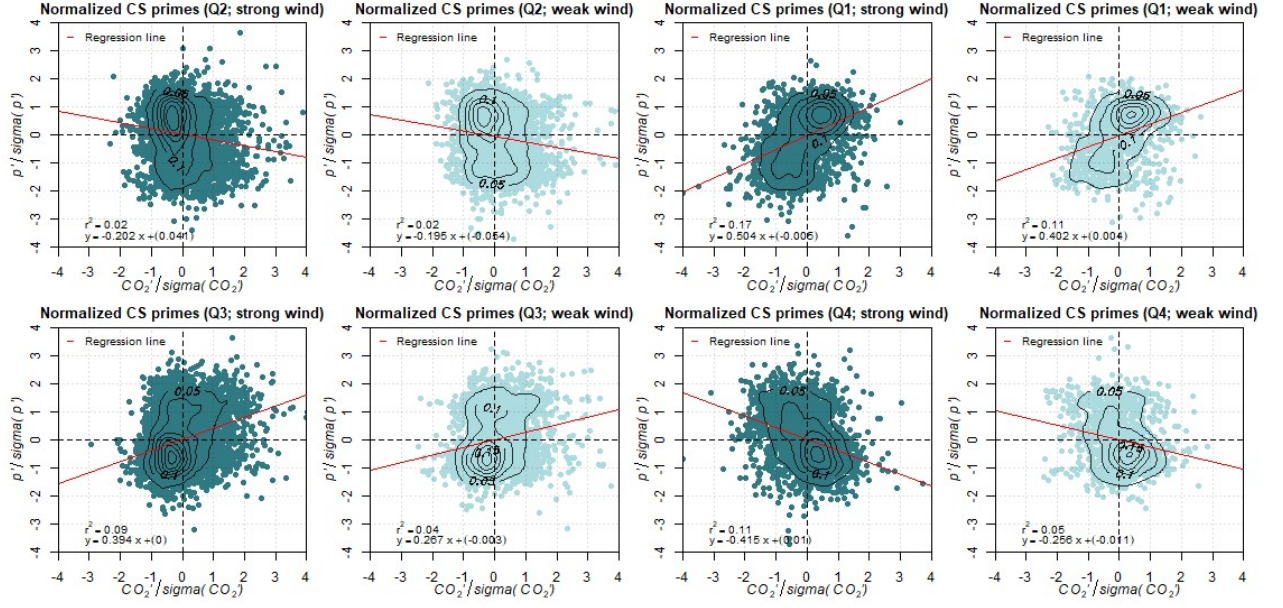


Figure 4.12.: Wind regime dependent quadrant analysis of the normalized  $p_{\text{soil}}'$  (y-axis) -  $\text{CO}_2_{\text{soil}}'$  (x-axis) correlation for the INTRAMIX campaign. The CS data was normalized by the 30 min period standard deviation of the raw data they fall into and categorized according to the first four columns of Table 4.1. These categories have been additionally filtered towards wind regimes (weak-wind: light green; strong-wind: dark green). A regression line was drawn for each categorized quadrant and the information about its linear function as well as the coefficient of determination is given in the bottom left corner for the respective category. Kernel density lines for each subplot are displayed with identical isolines.



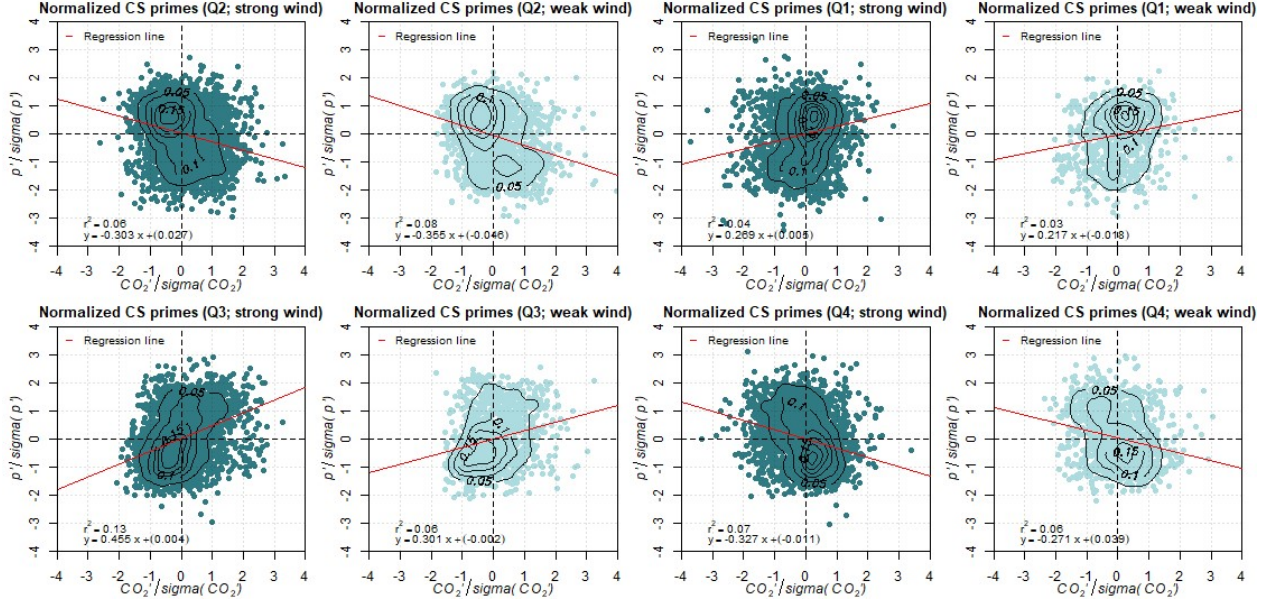


Figure 4.13.: Wind regime dependent quadrant analysis of the normalized  $p_{\text{soil}}'$  (y-axis) -  $\text{CO}_2 \text{soil}'$  (x-axis) correlation for the LOeWE campaign. The CS data was normalized by the 30 min period standard deviation of the raw data they fall into and categorized according to the first four columns of Table 4.2. These categories have been additionally filtered towards wind regimes (weak-wind: light green; strong-wind: dark green). A regression line was drawn for each categorized quadrant and the information about its linear function as well as the coefficient of determination is given in the bottom left corner for the respective category. Kernel density lines for each subplot are displayed with identical isolines.

Similar to Figs. 4.10 and 4.11, Figs. 4.14 and 4.15 show the categorization after the first four columns of Table 4.1 and Table 4.2 in a  $w_{\text{soil}}'$  (y-axis) -  $p_{\text{soil}}'$  (x-axis) coordinate system. This makes it possible to test for interdependencies between the  $p_{\text{soil}}'$  -  $\text{CO}_2 \text{soil}'$  categorization and the  $w_{\text{soil}}'$  -  $p_{\text{soil}}'$  correlation. An analysis on wind regimes within the  $w_{\text{soil}}'$  -  $p_{\text{soil}}'$  plot corresponding to Figs. 4.12 and 4.13 can be found in the appendices (Fig. D.1 and D.2).

Figure 4.14 and 4.15 show patterns of quadrant category one and two (see Table 4.1 and Table 4.2) having the kernel density center between Q1 and Q4 in the  $w_{\text{soil}}'$  -  $p_{\text{soil}}'$  correlation plot and quadrant category three and four showing the kernel density center between Q2 and Q3 of the  $w_{\text{soil}}'$  -  $p_{\text{soil}}'$  analysis. It can also be ascertained, that the variability in  $w_{\text{soil}}'$  is low and close to zero, such that the kernel density lines are stretched out along the x-axis ( $p_{\text{soil}}'$ ). Figure 4.14 and 4.15 show hardly any dependency of  $w_{\text{soil}}'$  on the  $p_{\text{soil}}'$  -  $\text{CO}_2 \text{soil}'$  correlation presented in Figs. 4.10 and 4.11. Therefore, it can be assumed, that at the perturbation time scale of CS 30 s, an averaging over the sweep and injection phases occurs on the vertical wind  $w_{\text{soil}}'$ . An even narrower  $w_{\text{soil}}'$  over the course of the INTRAMIX campaign compared to the LOeWE campaign additionally speaks for generally less strong-wind events (INTRAMIX

strong-wind occurrences: 63 %; LOeWE strong-wind occurrences: 70 % (see Chapter 3.2)) during the former.

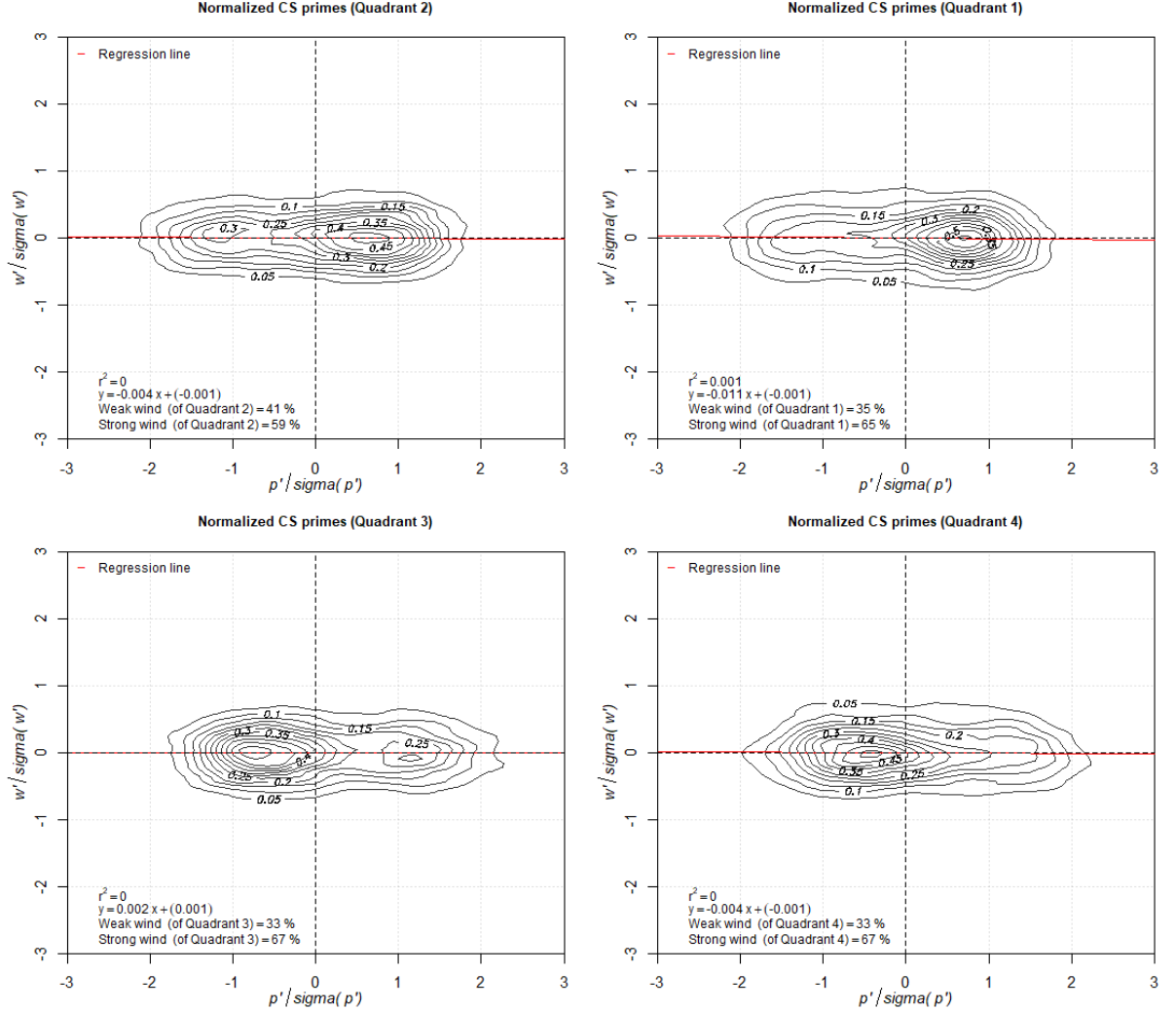


Figure 4.14.: Kernel density quadrant analysis of the normalized  $w_{\text{soil}}'$  (y-axis) -  $p_{\text{soil}}'$  (x-axis) correlation for the INTRAMIX campaign. The CS data was normalized by the 30 min period standard deviation of the raw data they fall into and categorized according to the first four columns of Table 4.1. A regression line was drawn for each categorized quadrant and the information about its linear function, the coefficient of determination and the relation of weak-wind to strong-wind occurrences is given in the bottom left corner for the respective category. Kernel density lines for each subplot are displayed with identical isolines.



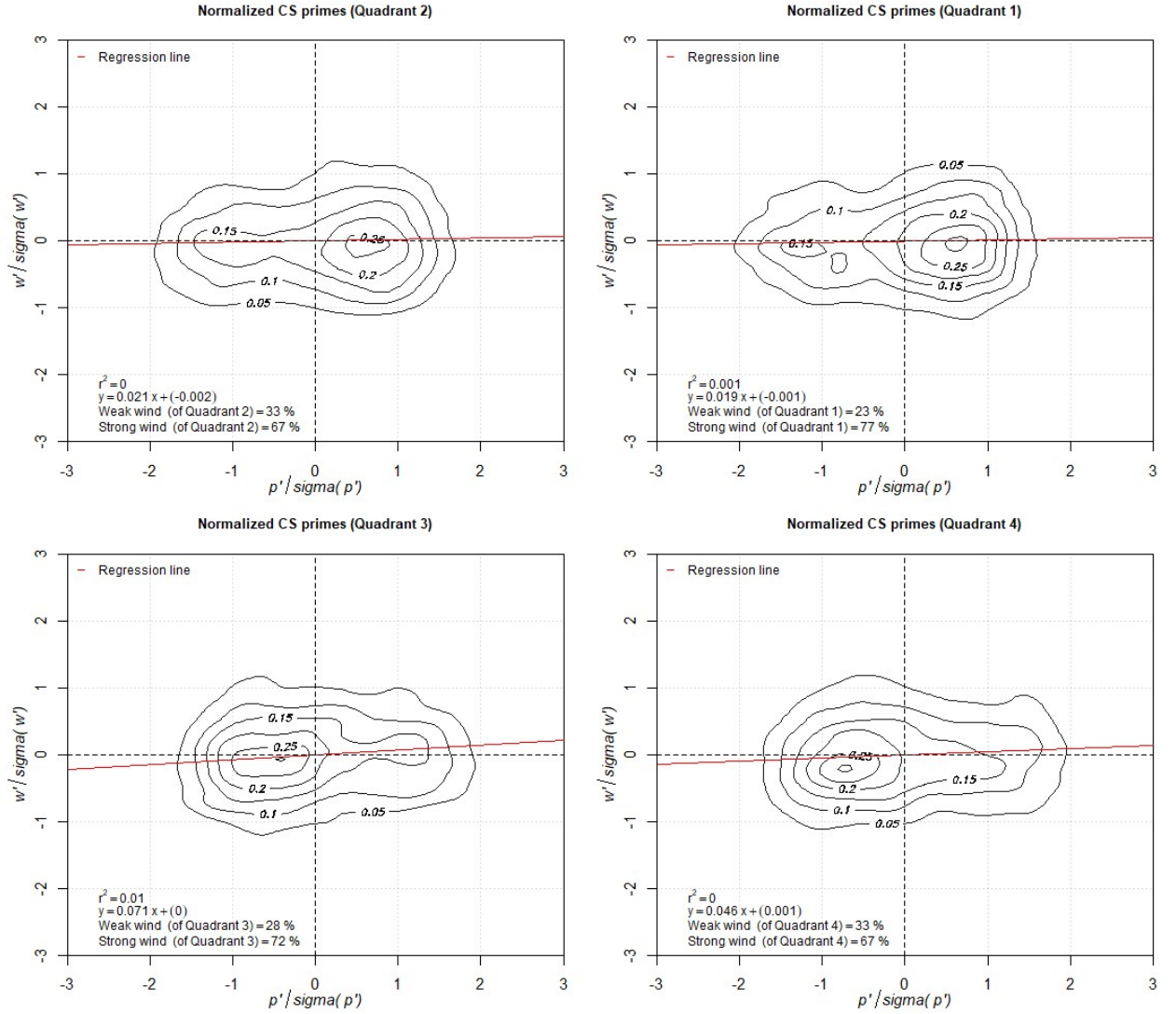


Figure 4.15.: Kernel density quadrant analysis of the normalized  $w_{soil}'$  (y-axis) -  $p_{soil}'$  (x-axis) correlation for the LOeWE campaign. The CS data was normalized by the 30 min period standard deviation of the raw data they fall into and categorized according to the first four columns of Table 4.2. A regression line was drawn for each categorized quadrant and the information about its linear function, the coefficient of determination and the relation of weak-wind to strong-wind occurrences is given in the bottom left corner for the respective category. Kernel density lines for each subplot are displayed with identical isolines.

Two figures (Fig. 4.16: INTRAMIX and Fig. 4.17: LOeWE) with exemplary CS 30 min period plots are given in the following not only for the soil station (brown)  $w_{soil}'$  -  $p_{soil}'$  correlation and  $p_{soil}'$  -  $CO_{2\ soil}'$  correlation, but also for the dependency of  $w_{soil}'$  on  $CO_{2\ soil}'$  as well as their respective equivalents at the 4 m station (blue). Owing to the missing gas analyzer at the 4 m station during the INTRAMIX experiment, only the  $w_{soil}'$  -  $p_{soil}'$

correlation can be shown in Fig. 4.16 for this height. Figure 4.16 and 4.17 further differentiate between strong-wind (soil: light brown, 4 m: light blue) and weak-wind (soil: dark brown, 4 m: dark blue) data and display the relation in percentage between these two parameters in the bottom left corner of each plot. Here, the linear function of the regression line, the coefficient of determination along with the date and time of the chosen 30 min period are presented as well. In order to provide a similar baseline situation for both campaigns, the case study plots are given for the same time of day (14:00 to 14:30) respectively. However, since the INTRAMIX and the LOeWE campaign do not span the same months of observation, the date of the case study was set for the last day of the INTRAMIX (11.07.2016) and the first day of the LOeWE (26.08.2020) experiment, such that seasonal effects are as comparable as possible for both. Similarly to the figures above (Fig. 4.10, 4.11, 4.12, 4.13, 4.14 and 4.15), the kernel density distribution was chosen as a tool to display distributional patterns in Fig. 4.16 and 4.17. In the quadrant categorization of Table 4.1 and 4.2 the INTRAMIX case study (Fig. 4.16) was sorted into Q3, whilst the one of the LOeWE campaign (Fig. 4.17) was categorized into Q4.

For all ten plots in Fig. 4.16 and 4.17, the strong-wind data significantly outweighs the weak-wind events. It can therefore be expected, that a fully coupled canopy with both sweep phases into the ground layer and ejection phases out of the sub-canopy prevails for this 30 min period. The case study for the soil station site generally represents the features of the already discussed overview plots from Fig. 4.10, 4.11, 4.12, 4.13, 4.14 and 4.15 quite well. Here again, the fluctuation in  $p_{\text{soil}}'$  is high compared to the one of  $w_{\text{soil}}'$ . However, the  $\text{CO}_2$  soil' variability seems smaller than for the bulk analyses. Respiration (mainly from the soil) and photosynthesis (mainly from mosses and grasses in direct vicinity to the soil station, as well as from the canopy) are both processes that need to be taken into account for this midday case. These mechanisms might cancel each other out over the course of the 30 s perturbation period, especially during the significant mixing expected for strong-wind data. The difference between the  $w_{\text{soil}}' - p_{\text{soil}}'$  and the  $w_{4\text{m}}' - p_{4\text{m}}'$  correlation plot is quite moderate in Fig. 4.16 and 4.17. This becomes particularly apparent for the LOeWE case study in Fig. 4.17. The INTRAMIX 30 min period plot (Fig. 4.16) of  $w_{\text{soil}}'$  against  $p_{\text{soil}}'$  shows a slightly narrower  $w'$  fluctuation compared to its 4 m station. The soil station presumably experiences a less thoroughly coupled ground layer, where horizontal advection may dominate over vertical mixing. A strong turbulent mixing with sweep and ejection phases in the LOeWE case study (Fig. 4.17) on the other hand, leads to a higher correlation of positive  $\text{CO}_2$  fluxes from the soil towards the sub-canopy and negative  $\text{CO}_2$  fluxes from the sub-canopy towards the surface. The sub-canopy 4 m  $\text{CO}_2$  experiences sufficiently strong vertical wind fluctuations coupled with a  $\text{CO}_2$  signal which is very close to zero. Again, this can be attributed to an averaging of the  $\text{CO}_2$  flux by powerful sweep and ejection motions.

Flow instabilities as a consequence of high wind velocities at the top of the canopy have been repeatedly shown to be the main initiator for the occurrence of coherent structures (Thomas et al., 2008; Thomas and Foken, 2007). Moreover, this thesis could confirm the findings of multiple other studies (Shaw et al., 1990; Ruppert et al., 2006; Takle et al., 2003), which determined a strong relationship between coherent structures and pressure pumping.

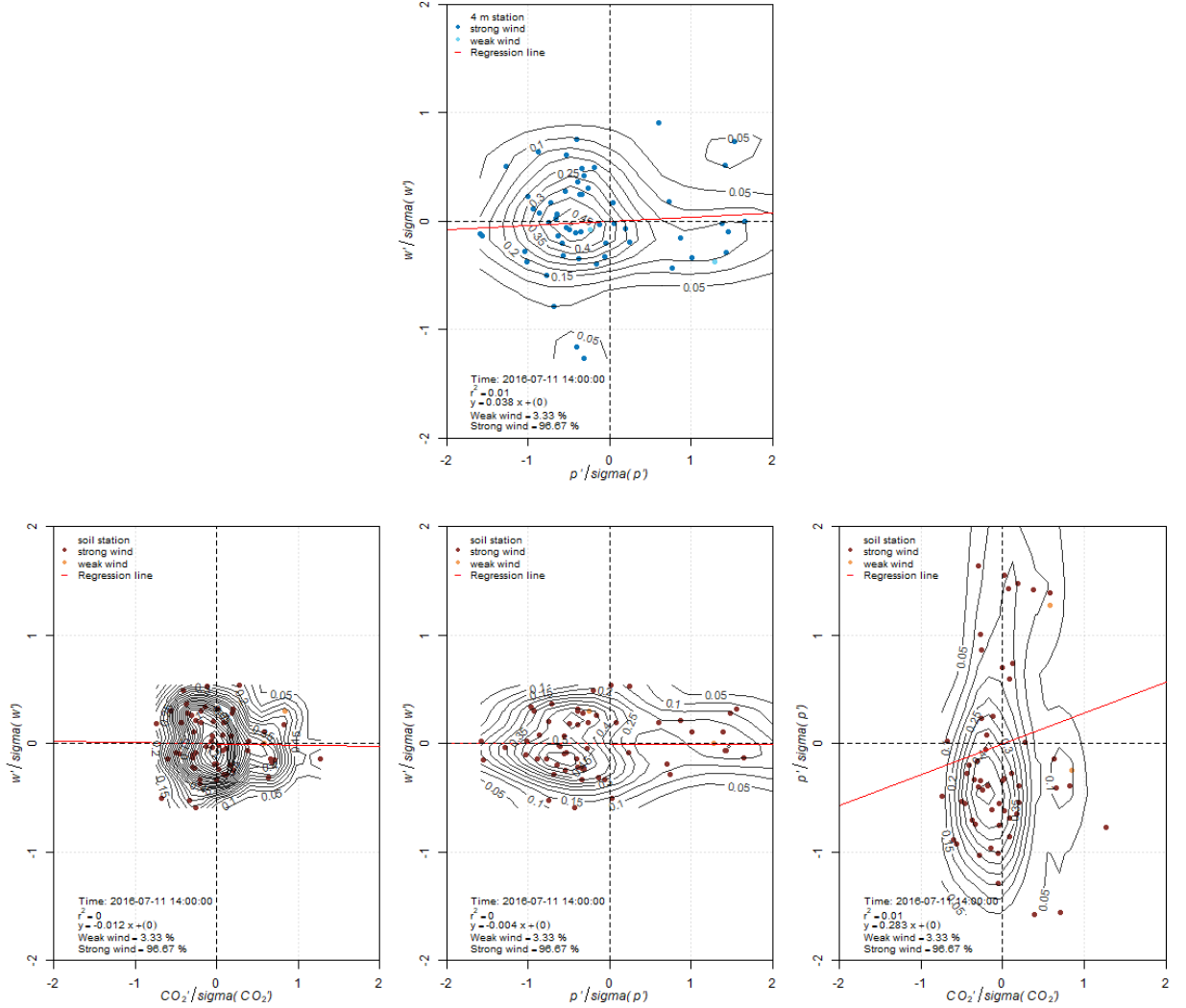


Figure 4.16.: Quadrant analysis case study for the INTRAMIX campaign. 4 m station plots (blue) are positioned over the respective soil station plots (brown) of the normalized  $w_{\text{soil}}' - CO_{2\text{soil}}'$ ,  $w_{\text{soil}}' - p_{\text{soil}}'$  and  $p_{\text{soil}}' - CO_{2\text{soil}}'$  correlation from left to right. Strong-wind data is displayed in the form of dark colored points, whereas weak-wind occurrences are given as lighter colored data points. Information about the date and time of day of the 30 min case study, as well as the coefficient of determination, the linear function of the regression line and the relationship between strong-wind and weak-wind data as percentage is presented in the bottom left corner of each correlation plot. Kernel density lines for each subplot are displayed with identical isolines.

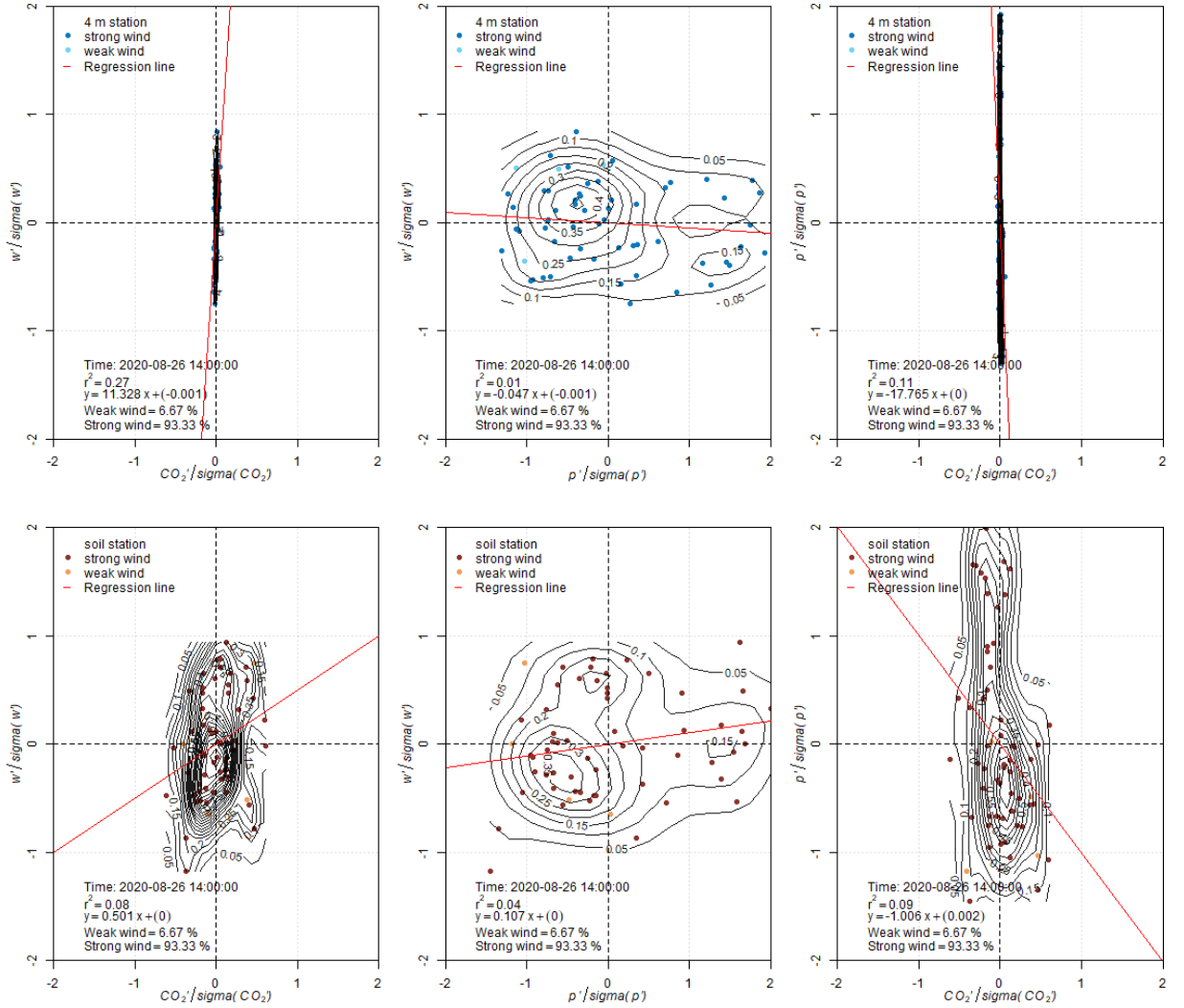


Figure 4.17.: Quadrant analysis case study for the LOeWE campaign. 4 m station plots (blue) are positioned over the respective soil station plots (brown) of the normalized  $w_{\text{soil}}' - CO_{2 \text{ soil}}'$ ,  $w_{\text{soil}}' - p_{\text{soil}}'$  and  $p_{\text{soil}}' - CO_{2 \text{ soil}}'$  correlation from left to right. Strong-wind data is displayed in the form of dark colored points, whereas weak-wind occurrences are given as lighter colored data points. Information about the date and time of day of the 30 min case study, as well as the coefficient of determination, the linear function of the regression line and the relationship between strong-wind and weak-wind data as percentage is presented in the bottom left corner of each correlation plot. Kernel density lines for each subplot are displayed with identical isolines.

Specifically, it was found in Chapter 4.2 (Fig. 4.8) that pressure perturbations of coherent structures increase in connection with drops in pressure on a synoptic time scale. Moreover, it was hypothesized in Chapter 1, that high wind velocities during strong-wind events are a main factor for the reinforcement of coherent structures and the pressure pumping phenomenon ( $H_4$ ). Thomas and Foken (2007) identify the C and Cs coupling regimes most likely to develop around midday and the afternoon hours. The fourth hypothesis ( $H_4$ ) of this thesis relates to these findings and speculates about a more pronounced pressure pumping during the day in contrast to nighttime and transition periods.

In Fig. 4.18 (INTRAMIX) and 4.19 (LOeWE) the categories of the quadrant analysis are given in accordance to Table 4.1 and 4.2 on the abscissa of four histograms. Histograms on the left hand side distinguish between daytime (yellow), nighttime (blue) and transition time (orange) data within the respective category (see Chapter 3.2), whilst the histograms on the right differentiate between strong-wind (dark green) and weak-wind (light green) events. Occurrences where the kernel density distribution for Table 4.1 and 4.2 were centered in more than one quadrant are here summarized in one category named "Rest". The frequency of the wind regime or time of day events are displayed with color-coded bars and given in absolute numbers by the counts of the y-axis. The percentage on top of each bar sets these absolute values of times of day or wind regime within a certain quadrant (1, 2, 3, 4, Rest, NA) into relation with the absolute values of times of day or wind regime of the whole CS data. The importance of this relationship refers back to the note, that the CS data is not equally distributed over all times of day and wind regimes after an extensive filtering of the raw data (see Chapter 3.2 and Fig. 3.1). The same histograms with information about the percentages of time of day events or wind-regime occurrences within one quadrant are shown in the appendices (see Fig. D.3 and D.4)

It becomes obvious again from Fig. 4.18 and 4.19, that for both campaigns strong-wind events are more abundant. Moreover, the analyzed data of the INTRAMIX experiment is heavily shifted towards the daytime events, whereas the times of day in the LOeWE campaign are more uniformly distributed. For both experiments however, most of the nighttime data has been filtered out after selecting the highest 5 % of pressure variances. Since Q2 and Q3 have been ascertained to be the quadrants with the largest fraction in density (see Table 4.1 and 4.2), they are of special interest in the wind-regime and time of day analysis. Particularly the INTRAMIX campaign showed a strong tendency towards Q2 (28% of all data) and Q3 (29 % of all data) in the discussion around Table 4.1. For the INTRAMIX histograms in Fig. 4.18, these quadrants are also the ones presenting a distinctive presence in daytime and strong-wind data. With 27 % and 28 % daytime data in Q2 and Q3 respectively, more than half of the total midday data is located in these quadrants. The same holds true for the strong-wind occurrences (Q2: 26 %; Q3: 30 %). This can be explained by the prevalence of higher wind velocities throughout the day, which results in flow instabilities at the top of the canopy as well as extensive coupling of the forest system. Moreover, these times of coupling seem to be dominated by strong sweep motions in conjunction with air being pushed from the canopy into the sub-canopy and the ground layer as argued in Fig. 4.9. This is in agreement with hypothesis  $H_4$ . In the course of the discussion around Fig. 4.10 and 4.11 it

was found, that higher temperatures for both, the INTRAMIX and the LOeWE campaign could be observed in Q3. This seems reasonable considering the large amount of daytime data existing within this quadrant. However, it also raises the question whether buoyancy could be a strong factor towards the pressure pumping phenomenon analyzed in this thesis. Despite of Shaw et al. (1990) claiming that buoyancy effects have been proven negligible in their study about pressure fluctuation at the forest ground, it has been known for decades that buoyancy along with shear are the driving forces behind the development of turbulence (Monin and Obukhov, 1954). During the LOeWE campaign, the daytime events in Q2 and Q3 are not as abundant as for the INTRAMIX campaign. However the transition time makes out a large fraction of the LOeWE data and shifts into focus. In fact, for both experiments, the times of the morning and evening hours are strongly represented in Q2 (INTRAMIX: 28 % of total transition data; LOeWE: 39 % of total transition data) and Q3 (INTRAMIX: 31 % of total transition data; LOeWE 32 % of total transition data). Buoyancy plays only a minor role during the night, where moderate turbulent flow is mainly provoked by weak-wind shear. During the morning hours however, the top of the canopy heats up more quickly than the air below and the buoyancy flux at higher levels of the canopy is stronger than the one in the sub-canopy. This might result in pressure differences and flow instabilities initiating mixing and driving the pressure pumping phenomenon. Both, the gradient of high static pressure aloft and low static pressure near the ground (see Fig. 4.9 Q3), as well as the buoyancy induced flow instabilities at the canopy crown with dynamic pressure pushing into the canopy (see Fig. 4.9 Q2) would cause a downward directed  $CO_2$  flux towards the soil station with air stemming from the canopy and sub-canopy. The prominence of air stemming from this direction has already been confirmed with Table 4.1 and 4.2 as well as Fig. 4.9. It can therefore be concluded that even though a more thoroughly analysis would need to be done in the future, the given data indicates some impact of buoyancy effects on the pressure pumping phenomenon. Nevertheless, the overall tendency towards daytime and strong-wind regime data located in Q2 and Q3 becomes apparent for the INTRAMIX, as well as the LOeWE campaign. Assuming  $H_3$  and  $H_4$  are true and apply, one would expect a pronounced relationship of daytime and transition time data as well as strong-wind events accumulated in Q2 and Q3 of a CS  $p_{soil}' - CO_{2\ soil}'$  quadrant analysis for future experiments.

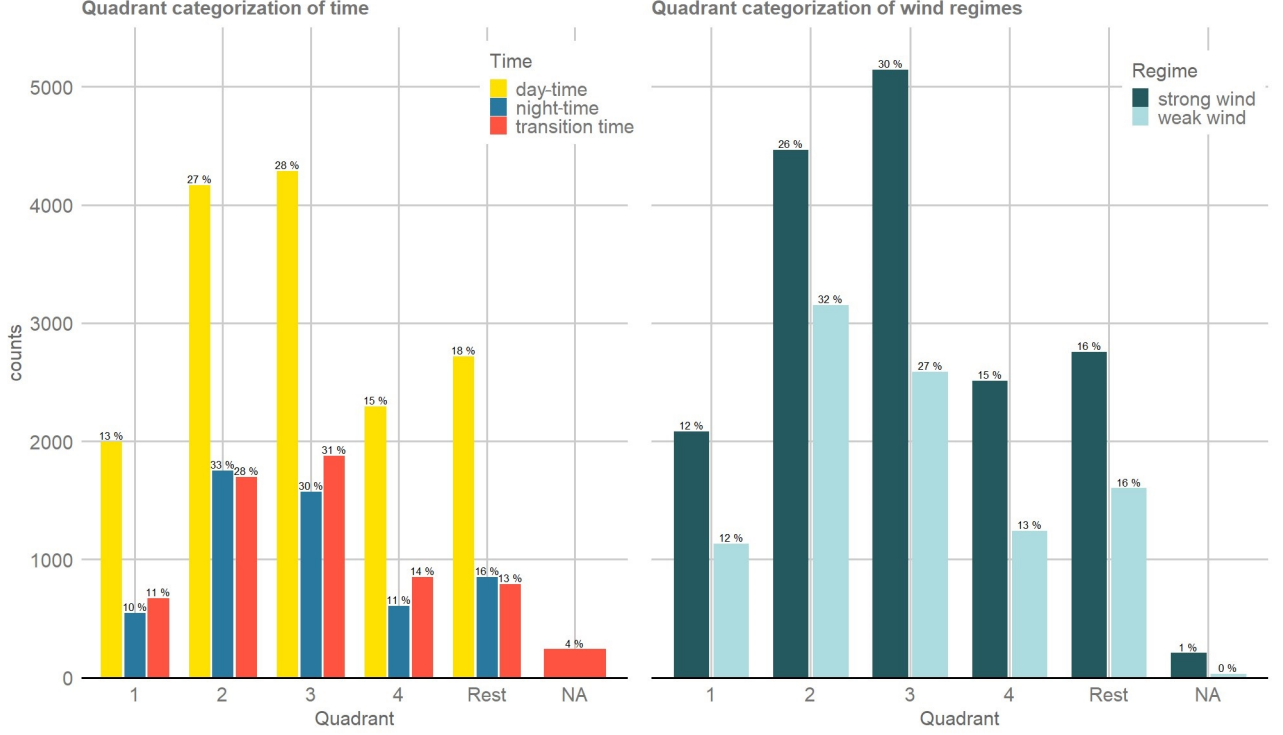


Figure 4.18.: Quadrant analysis after times of day (left) and wind regimes (right) for the INTRAMIX campaign. The categories of the quadrant analysis are given in accordance to Table 4.1 on the x-axis of the two histograms. The frequency of the wind regime or time of day events are displayed by color-coded bars (daytime: yellow, nighttime: blue, transition time: orange, strong-wind: dark green, weak-wind: light green) and given in absolute numbers by the counts of the y-axis. The percentage on top of each bar relates to the absolute values of times of day (or wind regime) within a certain quadrant (1, 2, 3, 4, Rest, NA) divided by the absolute values of times of day (or wind regime) of the whole CS data. Bars of one color add up to 100 %. Occurrences where the kernel density distribution for Table 4.1 were centered in more than one quadrant are summarized in one category named "Rest".



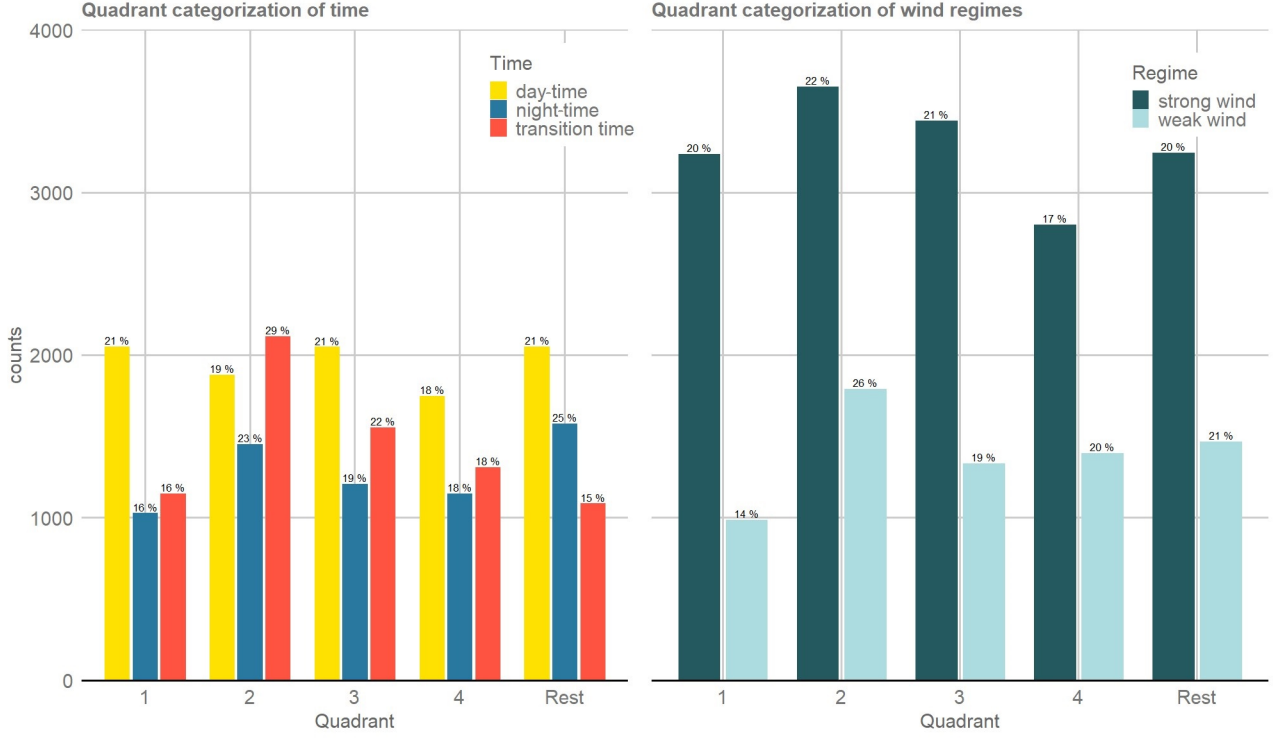


Figure 4.19.: Quadrant analysis after times of day (left) and wind regimes (right) for the LOeWE campaign. The categories of the quadrant analysis are given in accordance to Table 4.2 on the x-axis of the two histograms. The frequency of the wind regime or time of day events are displayed by color-coded bars (daytime: yellow, nighttime: blue, transition time: orange, strong-wind: dark green, weak-wind: light green) and given in absolute numbers by the counts of the y-axis. The percentage on top of each bar relates to the absolute values of times of day (or wind regime) within a certain quadrant (1, 2, 3, 4, Rest, NA) divided by the absolute values of times of day (or wind regime) of the whole CS data. Bars of one color add up to 100 %. Occurrences where the kernel density distribution for Table 4.2 were centered in more than one quadrant are summarized in one category named "Rest".

## 5. Conclusions

During two separate field experiments (INTRAMIX 2016 and LOeWE 2020) with almost identical setups, data was collected at two heights (soil station: 0.1 m, 4 m station: 4 m) in the sub-canopy of a mountainous central European spruce forest. The presented thesis used this data to perform a flux analysis, time series analysis and quadrant analysis and thereby managed to successfully identify flow modes capable of generating the pressure pumping phenomenon.

Four research questions with corresponding hypotheses were introduced in this work. Hypothesis  $H_1$  stated, that coherent structures covering time scales of 30 seconds are expected to dominate the pressure pumping phenomenon in terms of resolution and forcing. Furthermore, a high dependency of coherent structures on synoptic phenomena was anticipated. The findings of this thesis are in agreement with  $H_1$ . Wave-like pressure fluctuations with low amplitudes and wavelengths of several days were observed for the synoptic time scale (30 min averaging period). Minima of these synoptic motions associated with the passage of fronts were found to be correlated with strong pressure fluctuations on the time scale of coherent structures (30 s perturbation period). More precisely, a steep slope of the synoptic mean was ascertained to be accompanied by a high standard deviation of CS pressure with a coefficient of determination of  $R^2 = 0.40$  for the INTRAMIX campaign and  $R^2 = 0.55$  for the LOeWE experiment. The outcome of this analysis is in agreement with the work of Shaw et al. (1990) who showed that the surface pressure signal is mainly created by the velocity field near the top of the forest and that overpressure at the surface is strongly correlated with the passage of microfronts at the above-canopy linked to coherent structures. It was further hypothesized that the measurement instruments would only be able to detect static pressure opposed to dynamic pressure ( $H_2$ ). This assumption was initially based on the experimental setup of the pressure transducer with a built-in Quad-Disc probe. It could be determined however, that the collected data consists equally of signals attributed to dynamic pressure and static pressure. A possible explanation for the rejection of hypothesis  $H_2$  is offered by the findings of Wyngaard et al. (1994) towards the response of the Quad-Disc probe. They found a strong angular dependency for the static pressure error, as well as a weak sensor sensibility during times of small wind velocities. Both limitations exist in the presented setup of this thesis. Thirdly, based on the assumption that a vertical transport of air is initiated by either static pressure or advective/turbulent transport, no source area (air stemming from the soil or the sub-canopy) was expected to dominate the data detected at the soil station measurement site during the entire experimental period. However, it was hypothesized that a dominating source area will be found for smaller time periods. In this respect, a dependency on wind regimes, diurnal courses, soil properties and the behavior of sweeps and ejection connected to coherent structures was predicted. Over 62 % of the

INTRAMIX and more than 48 % of the LOeWE CS quadrant analysis could be allocated towards air stemming from the region above the 0.1 m height soil station. This accounts for over half of the discernible processes since 15 % of the INTRAMIX quadrant analysis results as well as 13 % of the LOeWE events could not be clearly attributed towards air originating from the soil or the sub-canopy. The connection between the source of air detected at the soil station and the underlying wind regimes, diurnal courses as well as sweep and ejection phases, manifested particularly well in Q3 of the  $p_{\text{soil}}' - CO_{2\text{soil}}'$  analysis. Here, strong sweep motions initiated by a low static pressure at the surface and a high static pressure at the top of the canopy lead to a coupled sub-canopy by sweeps (Cs) (Thomas and Foken, 2007) and bring warm, moist air from the canopy down into the ground layer. From this it can be concluded that the coupling of the forest with the sub-canopy and the canopy as the primary source of air seems to be dependent on strong-wind regimes and pronounced sweep motions. Hypothesis  $H_3$  is hereby confirmed. Whilst an effect of soil moisture on the pressure pumping phenomenon could not be verified from a quadrant analysis, it was taken into consideration for the discussion on the flux analysis. Even though the two campaigns studied in this thesis showed similar tendencies in the general behavior of their data, the INTRAMIX campaign yielded more pronounced variabilities in the  $CO_2$  flux on a 30 min averaging period. It was speculated, that these fluctuations can be attributed towards higher soil and air temperatures (INTRAMIX mean air temperature: 16 °C, LOeWE mean air temperature: 11 °C) during the INTRAMIX experiment. Together with an increase of VSMC (INTRAMIX VSMC: 31 %, LOeWE VSMC: 20 %) they are capable of driving soil respiration and enhancing the  $CO_2$  fluxes in the sub-canopy. Lastly it was predicted, that the full extent of the pressure pumping could be observed mainly during midday and in times of strong wind velocities ( $H_4$ ). For the INTRAMIX campaign, 27 % and 28 % of the daytime data were located in Q2 and Q3, respectively. This makes up more than half of the overall midday data of the entire INTRAMIX experiment. A similar distribution of the strong-wind events could be found for the same campaign (Q2: 26 %; Q3: 30 %). Although not as pronounced as for the 2016 experiment, the tendency for the LOeWE daytime data and strong-wind occurrences towards Q2 and Q3 was determined. The explanation for the acceptance of hypothesis  $H_4$  matches the one for  $H_3$ . High wind velocities, which prevail throughout the day are known to result in flow instabilities at the top of the canopy (Thomas and Foken, 2007; Thomas et al., 2008; Ruppert et al., 2006; Shaw et al., 1990). These flow instabilities initiate the development of coherent structures dominated by strong sweep motions. Consequently, air is being pushed down from the canopy into the sub-canopy and the ground layer in accordance with a high data accumulation in Q2 and Q3. Apart from the daytime data, transition time data was found to be strongly represented in Q2 and Q3. This was especially evident for the LOeWE campaign (Q2: 29 %, Q3: 22 % of the overall transition time data). In conjunction with this, it was theorized that transition time data and buoyancy fluxes might play an additional role in the pressure pumping discussion. However, the effect should be investigated in further research.

The results of the presented thesis are limited towards the assumptions about fluid mechanics stated in Fig. 4.9, as well as site and season specific properties. Whilst the outcome of

two separate campaigns at the same location and during similar climatic circumstances has proven itself to be replicable, results may differ across sites. Several authors have highlighted the importance of soil parameters such as soil pH, soil type, soil temperature, soil moisture and soil aeration (Subke et al., 2004; Flechard et al., 2007; Maier et al., 2010) as well as forest architecture (Thomas et al., 2008; Ehrnsperger, 2017) for the intensity of the pressure pumping phenomenon. Mohr et al. (2021) very recently analyzed wind-induced pressure fluctuations investing data from several different urban and natural sites in regards to the pressure pumping phenomenon. They found that wind direction in connection with the surrounding topography of the measurement site influences the strength of the wind-induced air pressure fluctuations. However, they did not examine their results on different time scales and introduced a new parameter for the measurement of the pressure pumping intensity. This so called pressure pumping coefficient yielded a surprisingly low dependency on local surface roughness and remains to be tested in further research. A more detailed study based on the presented thesis with a higher number of measurement stations vertically spanning the sub-canopy and canopy, as well as a larger range of experimental sites similar to Mohr et al. (2021) has the potential to broaden the understanding of the pressure pumping phenomenon. This approach can ultimately be helpful in closing the research gaps on the acquisition of a meaningful NEE. Specifically, a shared data base for pressure pumping related data might be a valuable means to achieving this goal. Additionally, it would be beneficial for the pressure pumping discussion to analyze the coupling regimes proposed by Thomas and Foken (2007) for the pressure pumping data in order to find more detailed connections between coupling mechanisms, diurnal courses and the soil-air gas exchange.

# Acknowledgements

I want to thank my supervisor Prof. Dr. Christoph Thomas, who guided me throughout the experimental and theoretical parts of my thesis with valuable inputs. Not only did he help me to achieve the completion of my Masters degree by supervising my thesis, but he also was a formative professional influence during my time as a Geoecologist at the University of Bayreuth. I also like to thank Dr.rer.nat. Wolfgang Babel for his insights concerning matters of software solutions and programming. My special thanks go to Johannes Olesch, who helped me with the preparation of my experiment and accompanied me during many Waldstein trips regarding the setup and troubleshooting of the measurement installations. Moreover, I wish to show my appreciation towards the entire working group of the DarkMix-Team, who were always prepared to join in numerous interesting scientific discussions during weekly meetings. Lastly, I would like to thank my family and friends for the moral support during the one year period of intense scientific work. This includes Tina, who was always happy to take on my occasional frustration from particularly difficult programming sessions on the BJJ mats.

# Bibliography

- Atkinson, J. (2009). Pressure. In Likens, G. E., editor, *Encyclopedia of Inland Waters*, pages 155–165. Academic Press, Oxford.
- Aubinet, M., Grelle, A., Ibrom, A., Rannik, S., Moncrieff, J., Foken, T., Kowalski, A., Martin, P., Berbigier, P., Bernhofer, C., Clement, R., Elbers, J., Granier, A., Grünwald, T., Morgenstern, K., Pilegaard, K., Rebmann, C., Snijders, W., Valentini, R., and Vesa, T. (2000). Estimates of the annual net carbon and water exchange of forests: the euroflux methodology. *Advances in Ecological Research*, 30(1):113–175.
- Babel, W., Lüers, J., Hübner, J., Rebmann, C., Wichura, B., Thomas, C. K., Serafimovich, A., and Foken, T. (2017). Long-term carbon and water vapour fluxes. In *Energy and matter fluxes of a spruce forest ecosystem*, pages 73–96. Springer.
- BayCEER. [http://www.bayceer.uni-bayreuth.de/meteo/de/klima/gru/html.php?id\\_obj=139938](http://www.bayceer.uni-bayreuth.de/meteo/de/klima/gru/html.php?id_obj=139938), accessed 26.04.2021.
- BayCEER. [http://www.bayceer.uni-bayreuth.de/meteo/de/forschung/proj/detail.php?id\\_obj=140737](http://www.bayceer.uni-bayreuth.de/meteo/de/forschung/proj/detail.php?id_obj=140737), accessed 26.05.2021.
- BayCEER. [https://www.bayceer.uni-bayreuth.de/bayceer/de/forschung/proj/m\\_detail.php?id\\_obj=78292](https://www.bayceer.uni-bayreuth.de/bayceer/de/forschung/proj/m_detail.php?id_obj=78292), accessed 27.05.2021.
- BayEOS. <https://bayeos.bayceer.uni-bayreuth.de/>, accessed 22.03.2021.
- BayernAtlas. <https://v.bayern.de/MhcnK>, accessed 18.03.2021.
- Böhm, M., Finnigan, J. J., Raupach, M. R., and Hughes, D. (2013). Turbulence structure within and above a canopy of bluff elements. *Boundary-layer meteorology*, 146(3):393–419.
- Ehrnsperger, L. (2017). Experimental evaluation of the significance of the pressure transport term to the Turbulence Kinetic Energy budget across contrasting forest architectures. Master’s thesis, University of Bayreuth.
- Flechard, C., Neftel, A., Jocher, M., Ammann, C., Leifeld, J., and Fuhrer, J. (2007). Temporal changes in soil pore space CO<sub>2</sub> concentration and storage under permanent grassland. *Agricultural and Forest Meteorology*, 142(1):66 – 84.
- Foken, T., Göckede, M., Mauder, M., Mahrt, L., Amiro, B., and Munger, W. (2004). Post-field data quality control. In *Handbook of micrometeorology*, pages 181–208. Springer.

- Freundorfer, A., Rehberg, I., Law, B. E., and Thomas, C. (2019). Forest wind regimes and their implications on cross-canopy coupling. *Agricultural and Forest Meteorology*, 279:107696.
- Gu, L., Falge, E. M., Boden, T., Baldocchi, D. D., Black, T., Saleska, S. R., Suni, T., Verma, S. B., Vesala, T., Wofsy, S. C., and Xu, L. (2005). Objective threshold determination for nighttime eddy flux filtering. *Agricultural and Forest Meteorology*, 128(3):179 – 197.
- Humphreys, E., Black, T., Ethier, G., Drewitt, G., Spittlehouse, D., Jork, E.-M., Nesic, Z., and Livingston, N. (2003). Annual and seasonal variability of sensible and latent heat fluxes above a coastal douglas-fir forest, british columbia, canada. *Agricultural and Forest Meteorology*, 115(1-2):109–125.
- Hussain, A. K. M. F. and Reynolds, W. C. (1970). The mechanics of an organized wave in turbulent shear flow. *Journal of Fluid mechanics*, 41(2):241–258.
- Kang, Y., Belušić, D., and Smith-Miles, K. (2015). Classes of structures in the stable atmospheric boundary layer. *Quarterly Journal of the Royal Meteorological Society*, 141(691):2057–2069.
- Launiainen, S., Rinne, J., Pumpanen, J., Kulmala, L., Kolari, P., Keronen, P., Siivola, E., Pohja, T., Hari, P., and Vesala, T. (2005). Eddy covariance measurements of co<sub>2</sub> and sensible and latent heat fluxes during a full year in a boreal pine forest trunk-space. *Boreal Environment Research*, 10:569–588.
- Liberzon, D. and Shemer, L. (2010). An inexpensive method for measurements of static pressure fluctuations. *Journal of Atmospheric and Oceanic Technology*, 27(4):776–784.
- Lindner, H. (1991). Strömende inkompressible flüssigkeiten. In *Physik für Ingenieure*, pages 134–153. Springer.
- Liu, H., Peters, G., and Foken, T. (2001). New equations for sonic temperature variance and buoyancy heat flux with an omnidirectional sonic anemometer. *Boundary-Layer Meteorology*, 100(3):459–468.
- Lu, S. and Willmarth, W. (1973). Measurements of the structure of the reynolds stress in a turbulent boundary layer. *Journal of Fluid Mechanics*, 60(3):481–511.
- Mahrt, L. (2010). Variability and maintenance of turbulence in the very stable boundary layer. *Boundary-layer meteorology*, 135(1):1–18.
- Mahrt, L. and Thomas, C. K. (2016). Surface stress with non-stationary weak winds and stable stratification. *Boundary-layer meteorology*, 159(1):3–21.
- Maier, M., Schack-Kirchner, H., Hildebrand, E. E., and Holst, J. (2010). Pore-space co<sub>2</sub> dynamics in a deep, well-aerated soil. *European Journal of Soil Science*, 61(6):877–887.



- Matteucci, G., Dore, S., Stivanello, S., Rebmann, C., and Buchmann, N. (2000). Soil respiration in beech and spruce forests in europe: trends, controlling factors, annual budgets and implications for the ecosystem carbon balance. In *Carbon and nitrogen cycling in European forest ecosystems*, pages 217–236. Springer.
- Misson, L., Baldocchi, D., Black, T., Blanken, P. D., Brunet, Y., Yuste, J. C., Dorsey, J., Falk, M., Granier, A., Irvine, M. R., et al. (2007). Partitioning forest carbon fluxes with overstory and understory eddy-covariance measurements: A synthesis based on fluxnet data. *Agricultural and Forest Meteorology*, 144(1-2):14–31.
- Mohr, M., Laemmle, T., Maier, M., Kolbe, S., Jung, C., Zeeman, M., Longdoz, B., Knohl, A., Thomas, C., and Schindler, D. (2021). Comparison of wind-induced air pressure fluctuations at sites with different land use. Number EGU21-3341. EGU General Assembly 2021.
- Monin, A. and Obukhov, A. (1954). Basic laws of turbulent mixing in the atmosphere near the ground. *Tr. Akad. Nauk SSSR Geofiz. Inst*, 24(151):163–187.
- Moore, C. J. (1986). Frequency response corrections for eddy correlation systems. *Boundary-Layer Meteorology*, 37(1):17–35.
- Nabuurs, G.-J., Masera, O., Andrasko, K., Benitez-Ponce, P., Boer, R., Dutschke, M., El-siddig, E., Fr, J., Frumhoff, P., Karjalainen, T., Krankina, O., Kurz, W., Matsumoto, M., Oyhantcabal, W., Ravindranath, N., Sanz-Sanchez, M.-J., and Zhang, X. (2007). *2007: Forestry. In Climate Change 2007: Mitigation. Contribution of Working Group III to the Fourth Assessment Report of the Intergovernmental Panel on Climate Change [B. Metz, O.R. Davidson, P.R. Bosch, R. Dave, L.A. Meyer (eds)]*. Cambridge University Press, Cambridge, United Kingdom and New York, NY, USA.
- Nishiyama, R. T. and Bedard Jr, A. J. (1991). A “quad-disc”static pressure probe for measurement in adverse atmospheres: With a comparative review of static pressure probe designs. *Review of scientific instruments*, 62(9):2193–2204.
- Orlanski, I. (1975). A rational subdivision of scales for atmospheric processes. *Bulletin of the American Meteorological Society*, pages 527–530.
- Raupach, M. R., Finnigan, J. J., and Brunet, Y. (1996). Coherent eddies and turbulence in vegetation canopies: the mixing-layer analogy. In *Boundary-layer meteorology 25th anniversary volume, 1970–1995*, pages 351–382. Springer.
- Ruppert, J., Mauder, M., Thomas, C., and Lüers, J. (2006). Innovative gap-filling strategy for annual sums of co2 net ecosystem exchange. *Agricultural and Forest Meteorology*, 138(1):5–18.
- Salesky, S. T., Katul, G. G., and Chamecki, M. (2013). Buoyancy effects on the integral lengthscales and mean velocity profile in atmospheric surface layer flows. *Physics of Fluids*, 25(10):105101.

- Shaw, R., Paw, K. U., Zhang, X., Gao, W., Den Hartog, G., and Neumann, H. (1990). Retrieval of turbulent pressure fluctuations at the ground surface beneath a forest. *Boundary-layer meteorology*, 50(1):319–338.
- Shaw, R. H., Tavangar, J., and Ward, D. P. (1983). Structure of the reynolds stress in a canopy layer. *Journal of Applied Meteorology and Climatology*, 22(11):1922–1931.
- Stoesser, T., Salvador, G. P., Rodi, W., and Diplas, P. (2009). Large eddy simulation of turbulent flow through submerged vegetation. *Transport in porous media*, 78(3):347–365.
- Subke, J.-A., Buchmann, N., and Tenhunen, J. (2004). Soil co<sub>2</sub> fluxes in spruce forests—temporal and spatial variation, and environmental controls. In *Biogeochemistry of Forested Catchments in a Changing Environment*, pages 127–141. Springer.
- Subke, J.-A. and Tenhunen, J. D. (2004). Direct measurements of co<sub>2</sub> flux below a spruce forest canopy. *Agricultural and forest meteorology*, 126(1-2):157–168.
- Takle, E. S., Brandle, J. R., Schmidt, R., Garcia, R., Litvina, I. V., Massman, W. J., Zhou, X., Doyle, G., and Rice, C. W. (2003). High-frequency pressure variations in the vicinity of a surface CO<sub>2</sub> flux chamber. *Agricultural and Forest Meteorology*, 114(3):245 – 250.
- Thomas, C. (2016). ERC Consolidator Grant 2016 Research proposal [Part B2].
- Thomas, C. and Foken, T. (2007). Flux contribution of coherent structures and its implications for the exchange of energy and matter in a tall spruce canopy. *Boundary-Layer Meteorology*, 123:317–337.
- Thomas, C., Martin, J., Goeckede, M., Siqueira, M., Foken, T., Law, B., Loescher, H., and Katul, G. (2008). Estimating daytime subcanopy respiration from conditional sampling methods applied to multi-scalar high frequency turbulence time series. *Agricultural and Forest Meteorology*, 148:1210–1229.
- Thomas, C., Martin, J., Law, B., and Davis, K. (2013). Toward biologically meaningful net carbon exchange estimates for tall, dense canopies: Multi-level eddy covariance observations and canopy coupling regimes in a mature Douglas-fir forest in Oregon. *Agricultural and Forest Meteorology*, 173:14–27.
- Thomas, C. K. (2011). Variability of sub-canopy flow, temperature, and horizontal advection in moderately complex terrain. *Boundary-layer meteorology*, 139(1):61–81.
- Thomas, C. K., Law, B. E., Irvine, J., Martin, J. G., Pettijohn, J. C., and Davis, K. J. (2009). Seasonal hydrology explains interannual and seasonal variation in carbon and water exchange in a semiarid mature ponderosa pine forest in central oregon. *Journal of Geophysical Research: Biogeosciences*, 114(G4).
- Wallace, J. M., Eckelmann, H., and Brodkey, R. S. (1972). The wall region in turbulent shear flow. *Journal of Fluid Mechanics*, 54(1):39–48.

- Wang, L.-P., Chen, S., Brasseur, J. G., and Wyngaard, J. C. (1996). Examination of hypotheses in the Kolmogorov refined turbulence theory through high-resolution simulations. Part 1. Velocity field. *Journal of Fluid Mechanics*, 309:113–156.
- Webb, E. K., Pearman, G. I., and Leuning, R. (1980). Correction of flux measurements for density effects due to heat and water vapour transfer. *Quarterly Journal of the Royal Meteorological Society*, 106(447):85–100.
- Wilczak, J. M., Oncley, S. P., and Stage, S. A. (2001). Sonic anemometer tilt correction algorithms. *Boundary-layer meteorology*, 99(1):127–150.
- Wunder, T. (2017). Erhebung und auswertung von windregimen in dichten waldbeständen. Master’s thesis, University of Bayreuth.
- Wyngaard, J., Siegel, A., and Wilczak, J. (1994). On the response of a turbulent-pressure probe and the measurement of pressure transport. *Boundary-layer meteorology*, 69(4):379–396.

## A. Data Processing

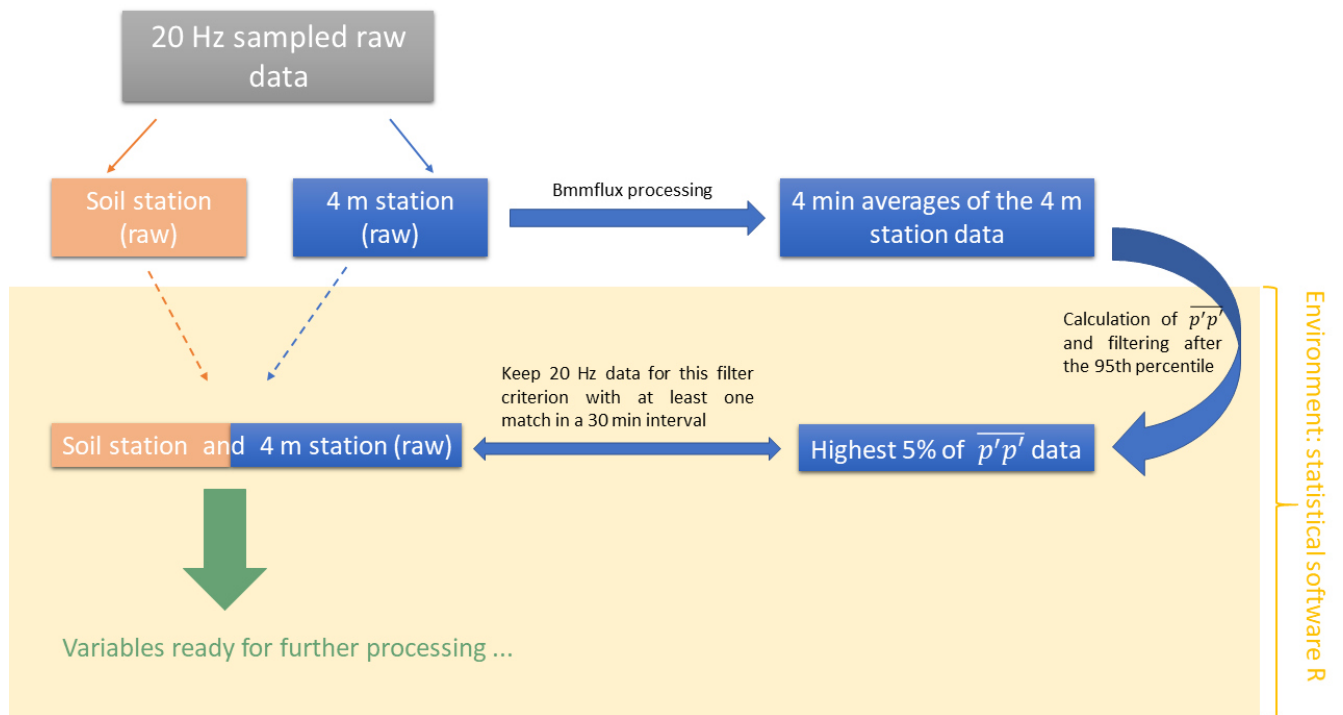


Figure A.1.: Flow chart of the pressure pumping data processing

## B. Flux Analysis

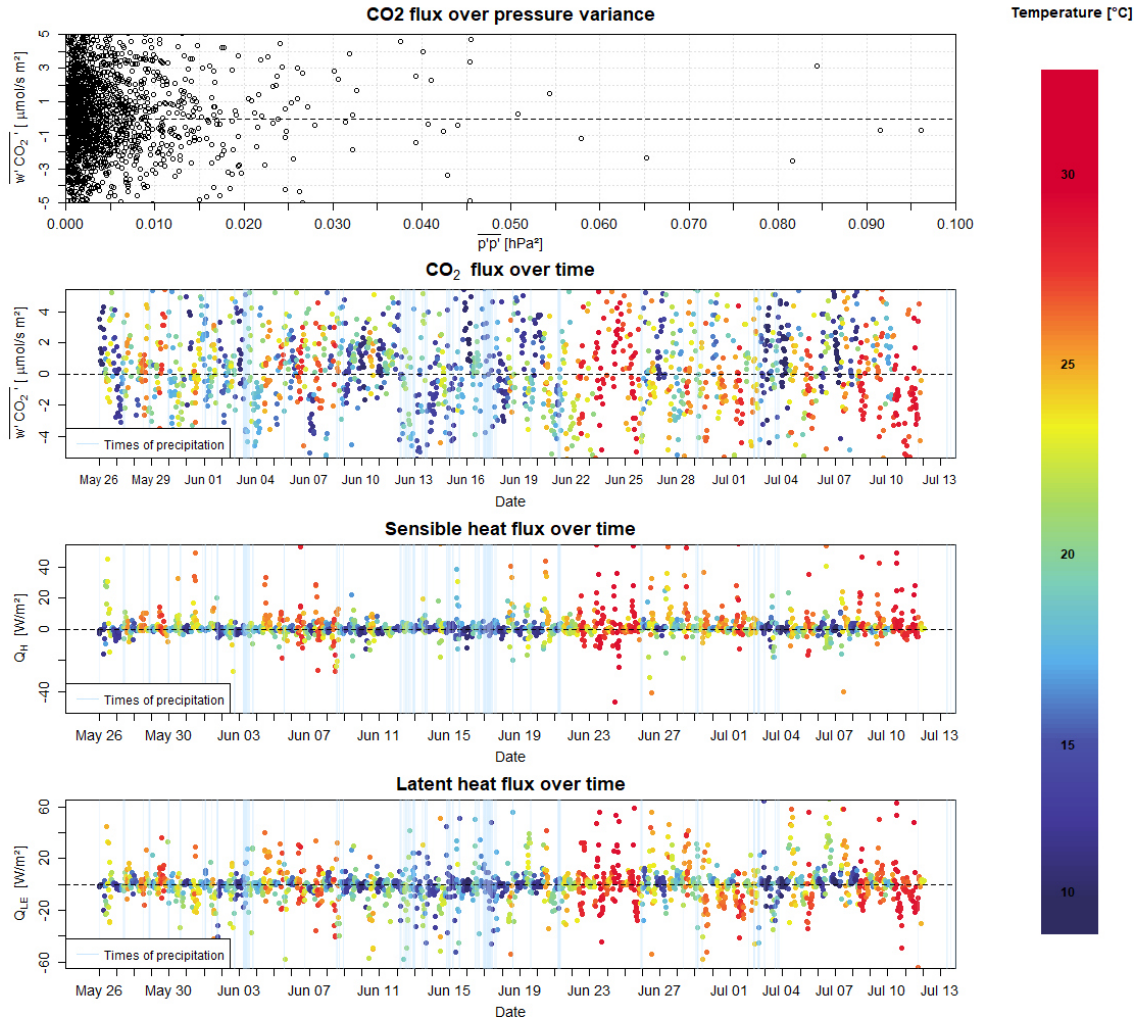


Figure B.1.: Flux analysis overview plot for the soil station measurement site of the IN-TRAMIX campaign with an averaging period of 30 min. Dependencies between the CO<sub>2</sub> flux ( $w'CO_2'$ , 95th percentile within plausibility limits:  $3.9 \mu\text{mol s}^{-1} \text{m}^{-2}$ ) and pressure variance ( $p'p'$ ) (first plot) as well as the time series of the CO<sub>2</sub> flux (second plot), sensible heat flux ( $Q_H$ ) (third plot) and latent heat flux ( $Q_{LE}$ ) (fourth plot) are provided for the entire period of the INTRAMIX experiment. The time series are color-coded by temperature and marked with blue vertical lines during precipitation events.

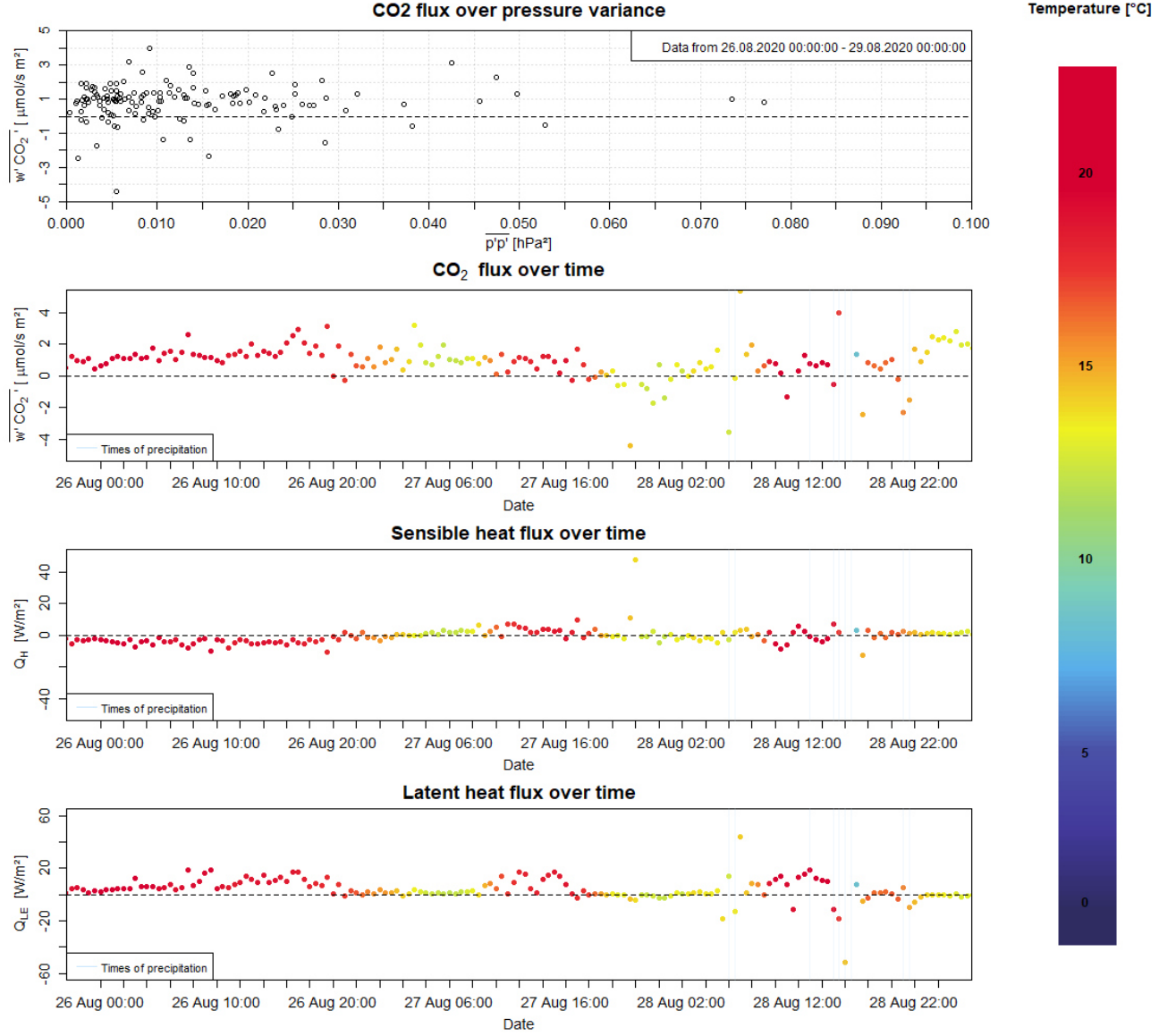


Figure B.2.: Flux analysis case study (26.08.2020 00:00:00 to 29.08.2020 00:00:00) for the 4 m station measurement site of the LOeWE campaign with an averaging period of 30 min. Dependencies between the CO<sub>2</sub> flux ( $w'CO_2'$ ) and pressure variance ( $\overline{p'p'}$ ) (first plot) as well as the time series of the CO<sub>2</sub> flux (second plot), sensible heat flux ( $Q_H$ ) (third plot) and latent heat flux ( $Q_{LE}$ ) (fourth plot) are provided for the entire period of the INTRAMIX experiment. The time series are color-coded by temperature and marked with blue vertical lines during precipitation events.

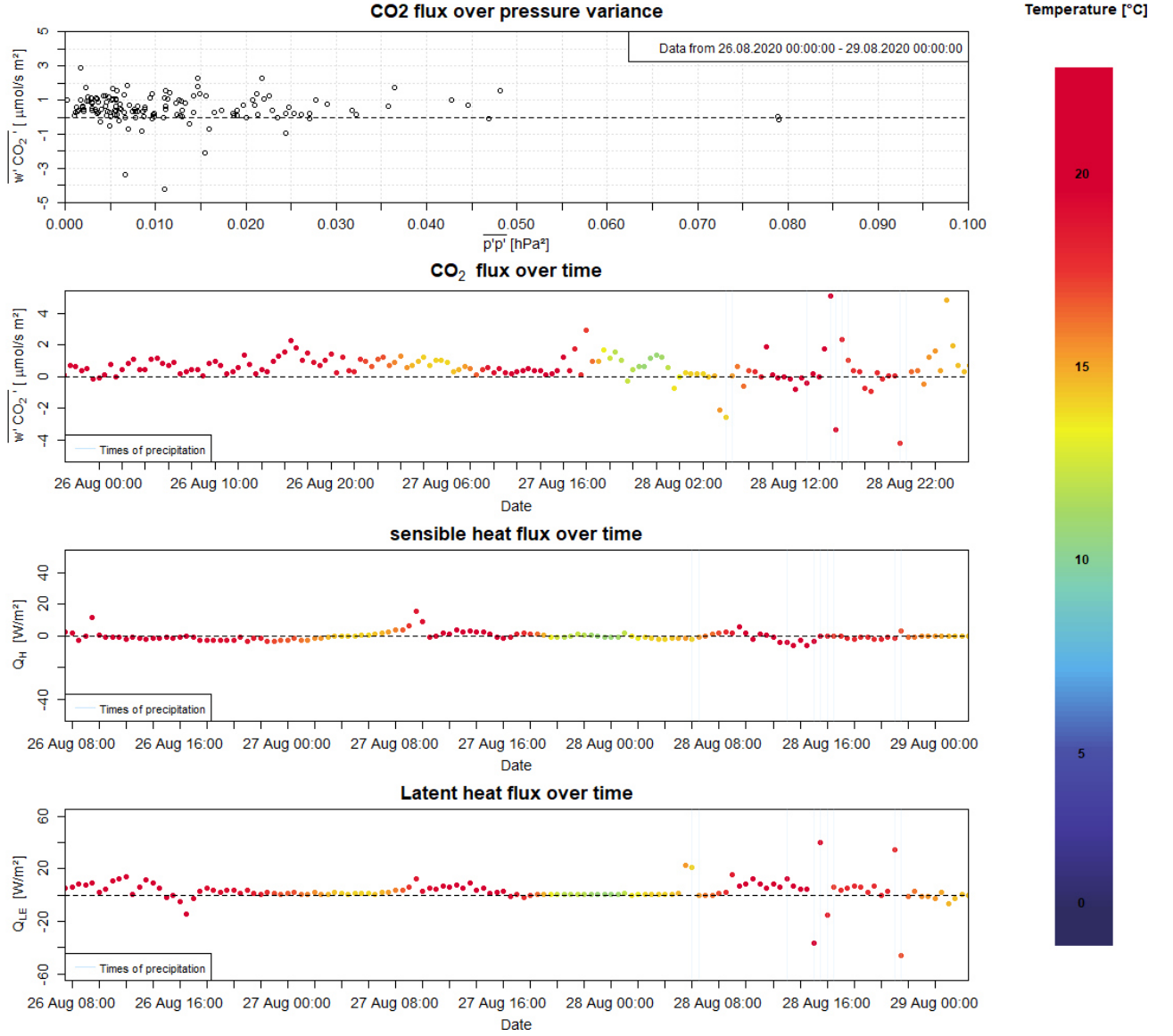


Figure B.3.: Flux analysis case study (26.08.2020 00:00:00 to 29.08.2020 00:00:00) for the soil station measurement site of the LOeWE campaign with an averaging period of 30 min. Dependencies between the CO<sub>2</sub> flux ( $w'CO_2'$ ) and pressure variance ( $p'p'$ ) (first plot) as well as the time series of the CO<sub>2</sub> flux (second plot), sensible heat flux ( $Q_H$ ) (third plot) and latent heat flux ( $Q_{LE}$ ) (fourth plot) are provided for the entire period of the INTRAMIX experiment. The time series are color-coded by temperature and marked with blue vertical lines during precipitation events.

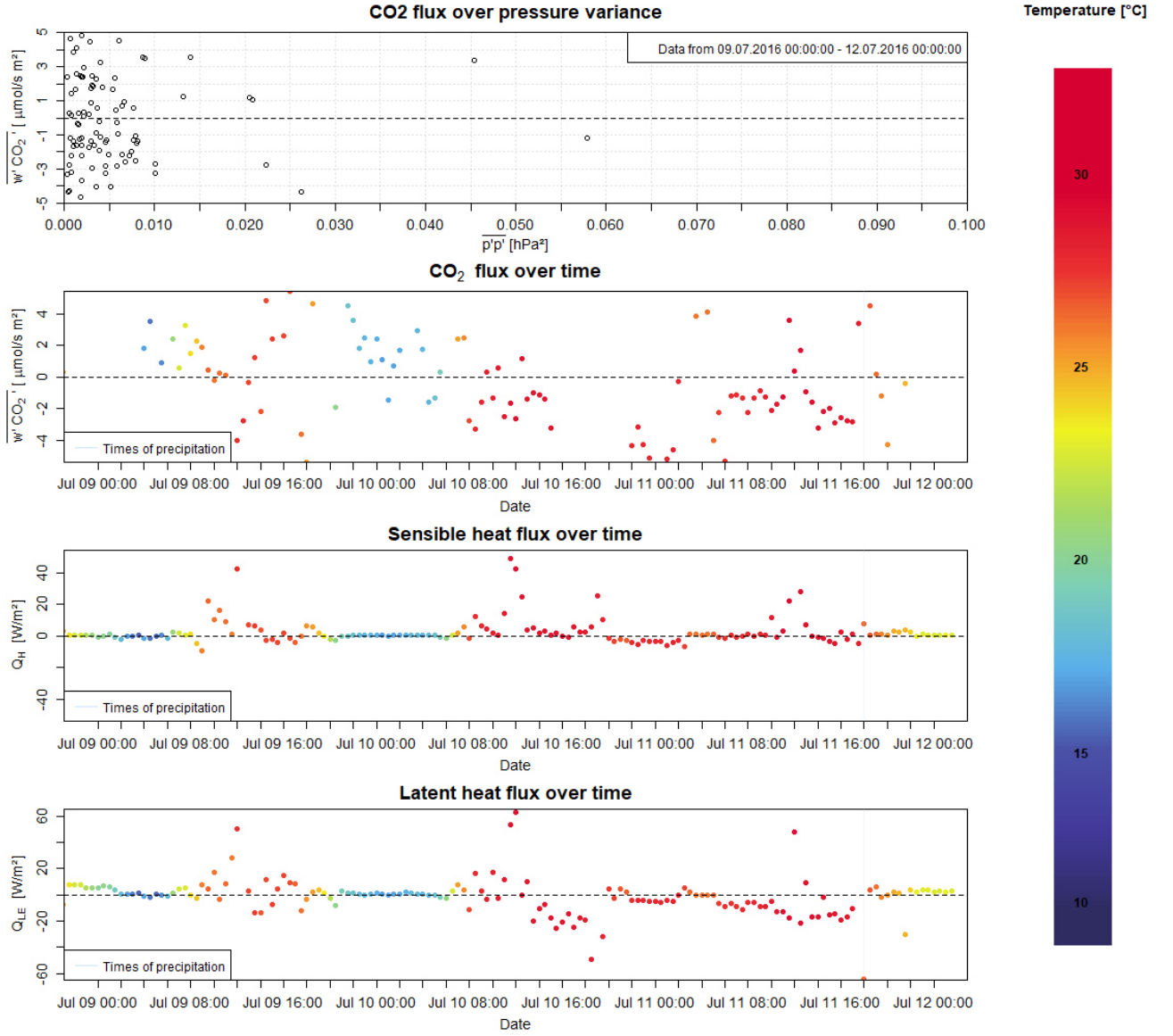


Figure B.4.: Flux analysis case study (09.07.2016 00:00:00 to 12.07.2016 00:00:00) for the soil station measurement site of the INTRAMIX campaign with an averaging period of 30 min. Dependencies between the CO<sub>2</sub> flux ( $w'CO_2$ ) and pressure variance ( $\overline{p'p'}$ ) (first plot) as well as the time series of the CO<sub>2</sub> flux (second plot), sensible heat flux ( $Q_H$ ) (third plot) and latent heat flux ( $Q_{LE}$ ) (fourth plot) are provided for the entire period of the INTRAMIX experiment. The time series are color-coded by temperature and marked with blue vertical lines during precipitation events.



## C. Time Series Analysis

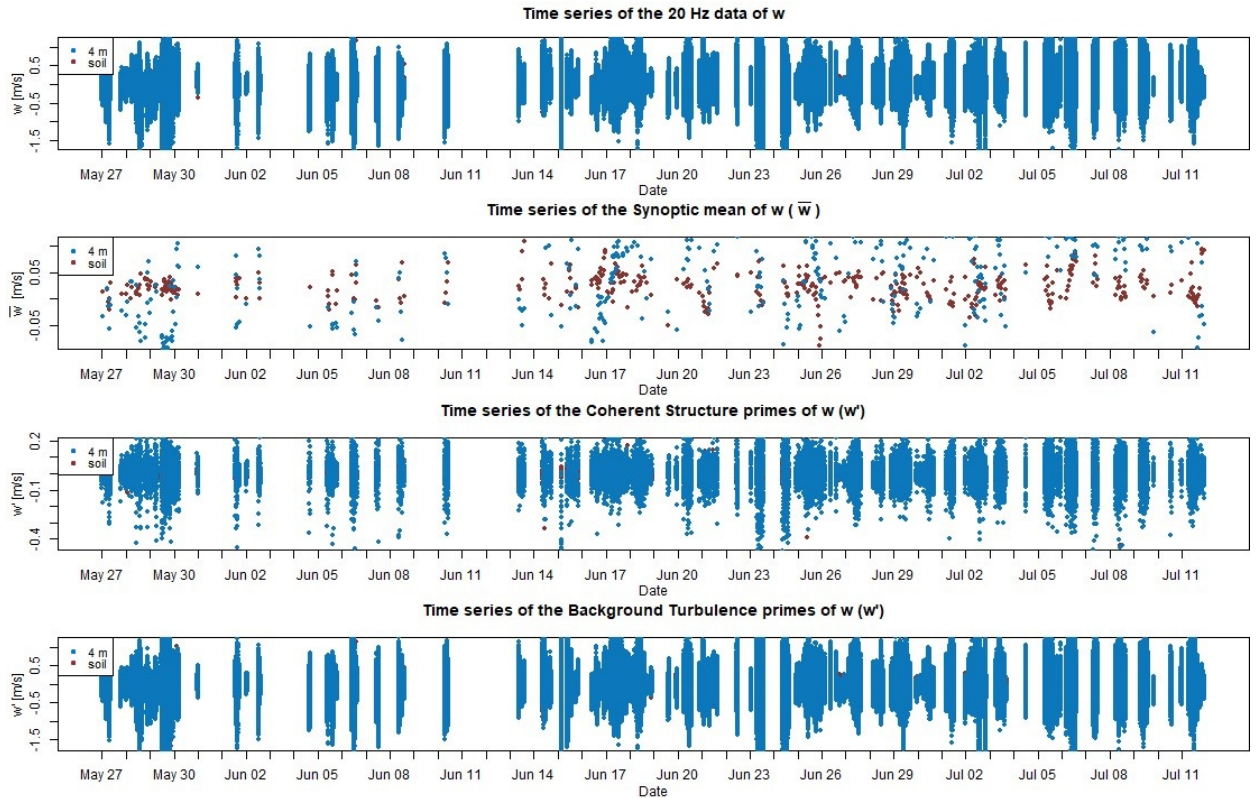


Figure C.1.: Time series analysis of the vertical wind during the INTRAMIX campaign, showing the raw data (20 Hz), synoptic mean (30 min), coherent structures (30 s) and background turbulence (20 Hz) for the soil station (brown) and 4 m station (blue).

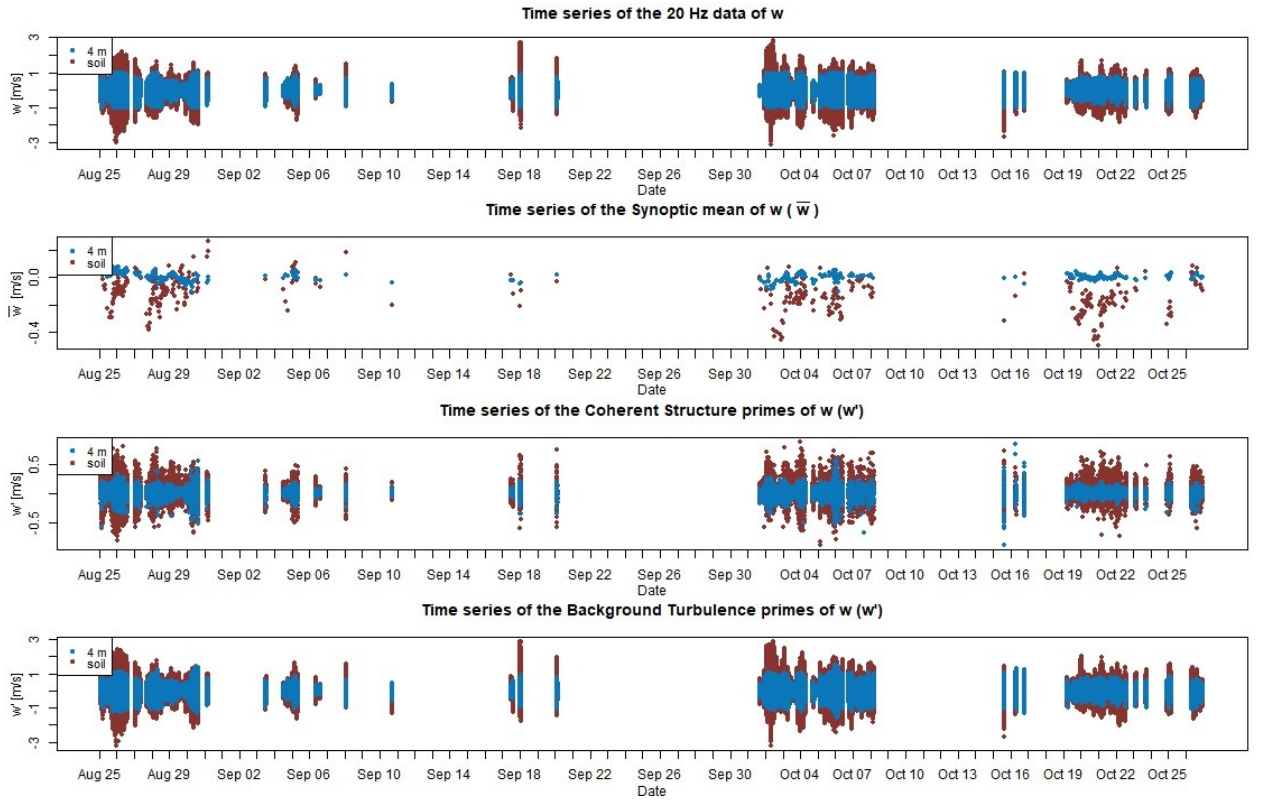


Figure C.2.: Time series analysis of the vertical wind during the LOeWE campaign, showing the raw data (20 Hz), synoptic mean (30 min), coherent structures (30 s) and background turbulence (20 Hz) for the soil station (brown) and 4 m station (blue).

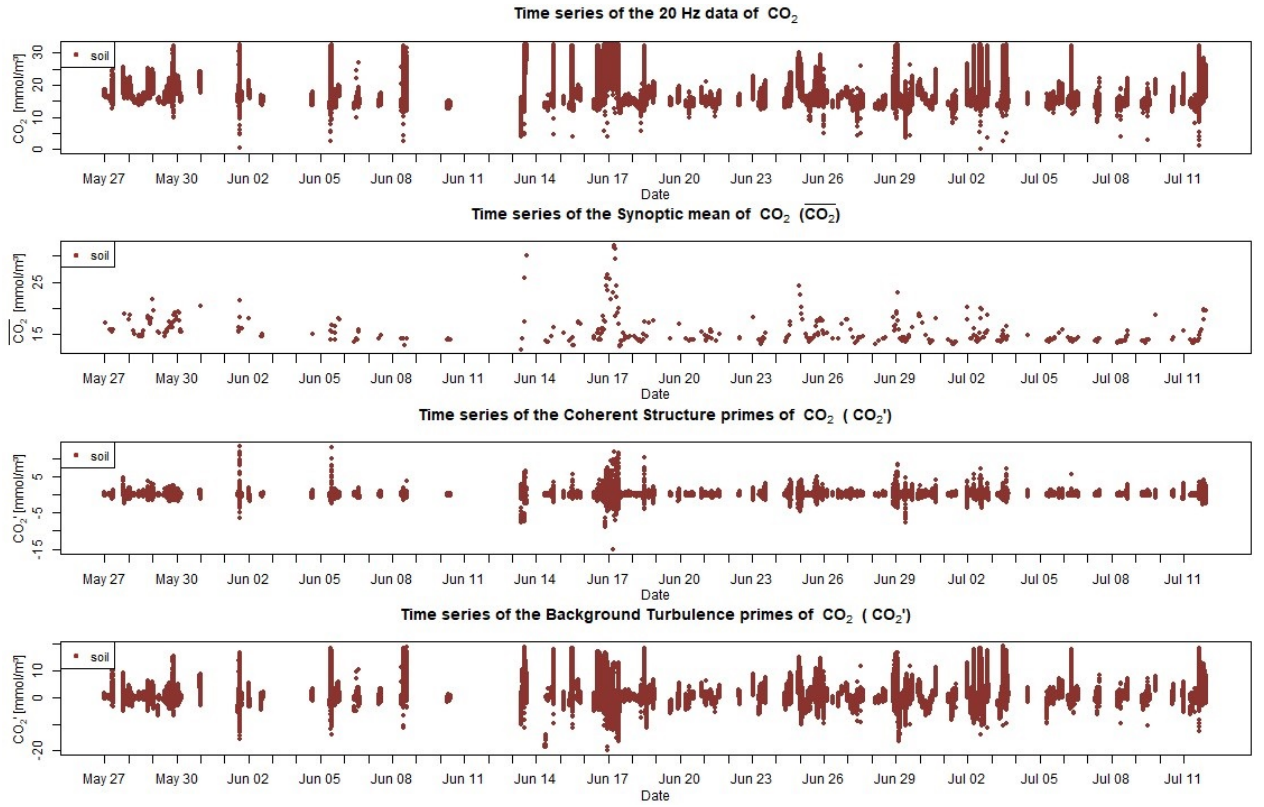


Figure C.3.: Time series analysis of the CO<sub>2</sub> concentration during the INTRAMIX campaign, showing the raw data (20 Hz), synoptic mean (30 min), coherent structures (30 s) and background turbulence (20 Hz) for the soil station (brown) and 4 m station (blue).

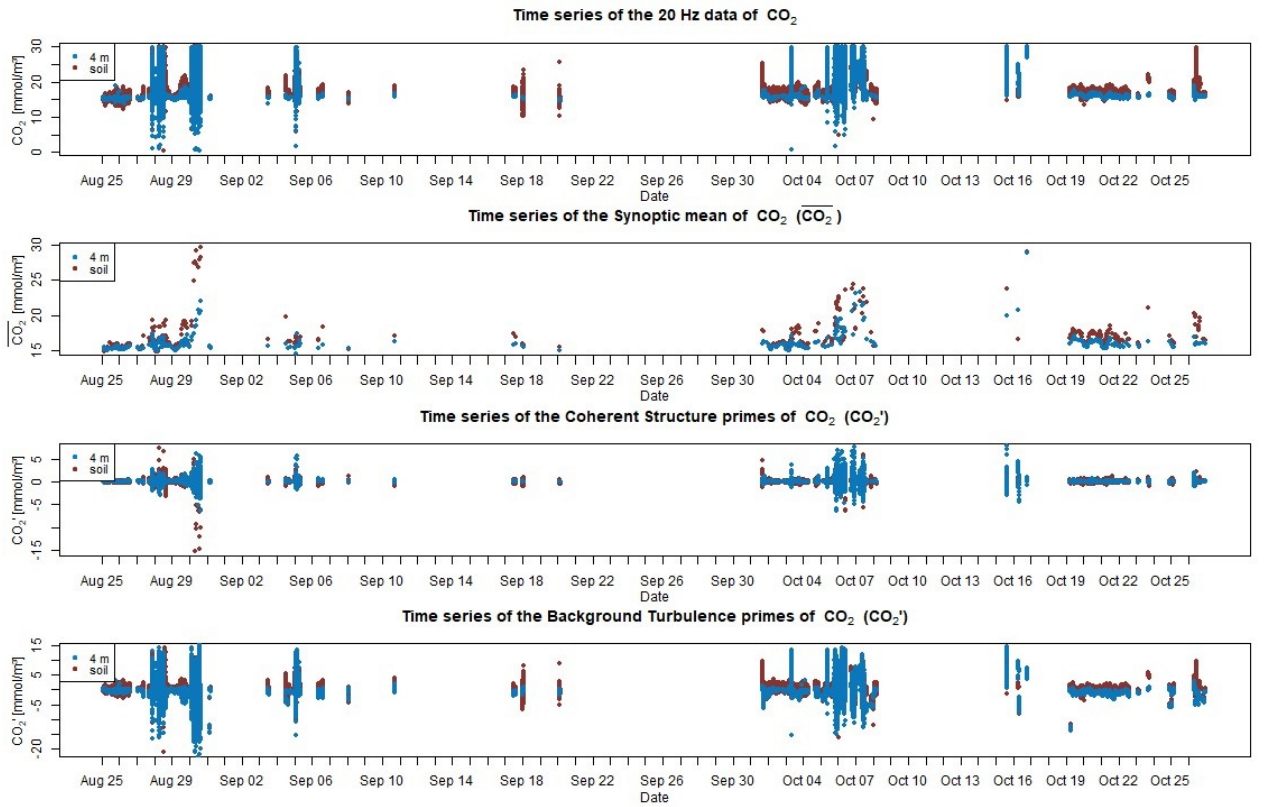


Figure C.4.: Time series analysis of the  $\text{CO}_2$  concentration during the LOeWE campaign, showing the raw data (20 Hz), synoptic mean (30 min), coherent structures (30 s) and background turbulence (20 Hz) for the soil station (brown) and 4 m station (blue).

## D. Quadrant Analysis

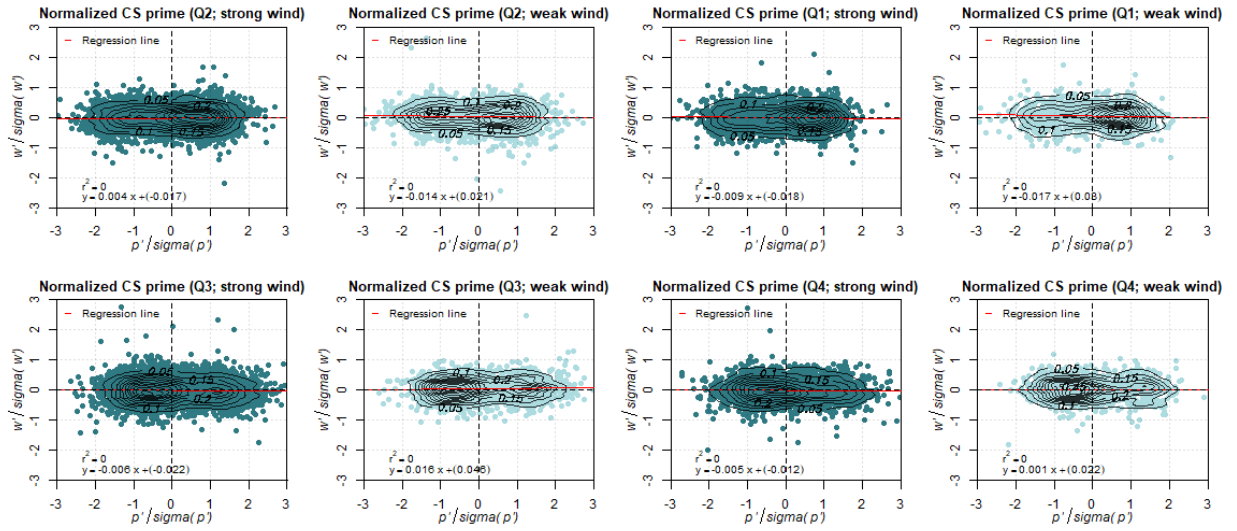


Figure D.1.: Wind regime dependent quadrant analysis of the normalized  $w_{\text{soil}}'$  (y-axis) -  $p_{\text{soil}}'$  (x-axis) correlation for the INTRAMIX campaign. The CS data was normalized by the 30 min period standard deviation of the raw data they fall into and categorized according to the first four columns of Table 4.1. These categories have been additionally filtered towards wind regimes (weak-wind: light green; strong-wind: dark green). A regression line was drawn for each categorized quadrant and the information about its linear function as well as the coefficient of determination is given in the bottom left corner for the respective category. Kernel density lines for each subplot are displayed with identical isolines.



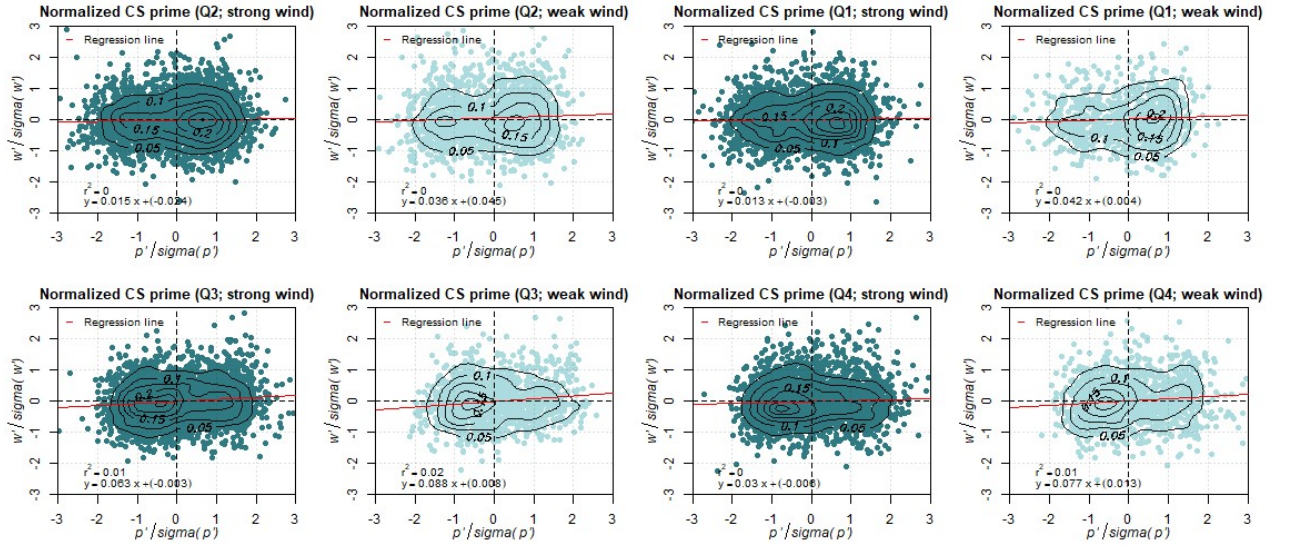


Figure D.2.: Wind regime dependent quadrant analysis of the normalized  $w_{\text{soil}}'$  (y-axis) -  $p_{\text{soil}}'$  (x-axis) correlation for the LOeWE campaign. The CS data was normalized by the 30 min period standard deviation of the raw data they fall into and categorized according to the first four columns of Table 4.2. These categories have been additionally filtered towards wind regimes (weak-wind: light green; strong-wind: dark green). A regression line was drawn for each categorized quadrant and the information about its linear function as well as the coefficient of determination is given in the bottom left corner for the respective category. Kernel density lines for each subplot are displayed with identical isolines.

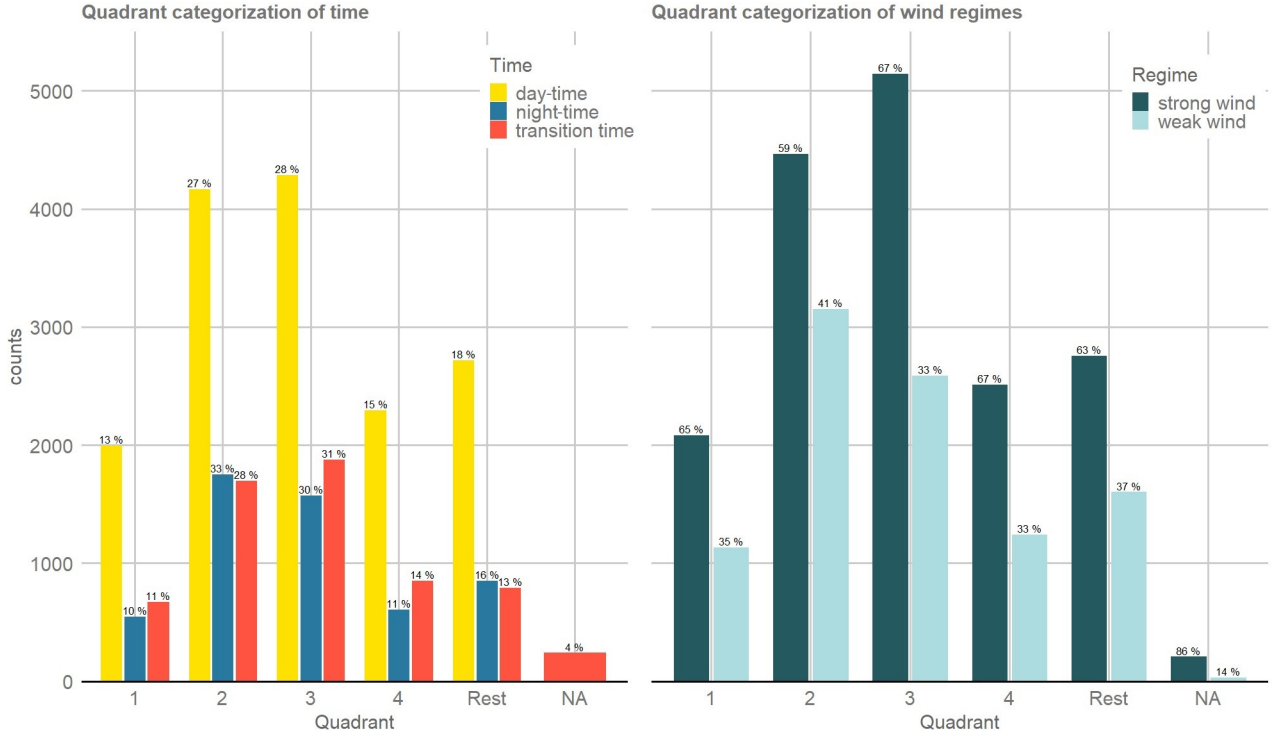


Figure D.3.: Quadrant analysis after times of day (left) and wind regimes (right) for the INTRAMIX campaign. The categories of the quadrant analysis are given in accordance to Table 4.1 on the x-axis of the two histograms. The frequency of the wind regime or time of day events are displayed by color-coded bars (daytime: yellow, nighttime: blue, transition time: orange, strong-wind: dark green, weak-wind: light green) and given in absolute numbers by the counts of the y-axis. On top of every bar the percentage of each time of day (or wind regime) in relation to the others within the respective quadrant is presented. Occurrences where the kernel density distribution for Table 4.1 were centered in more than one quadrant are summarized in one category named "Rest".



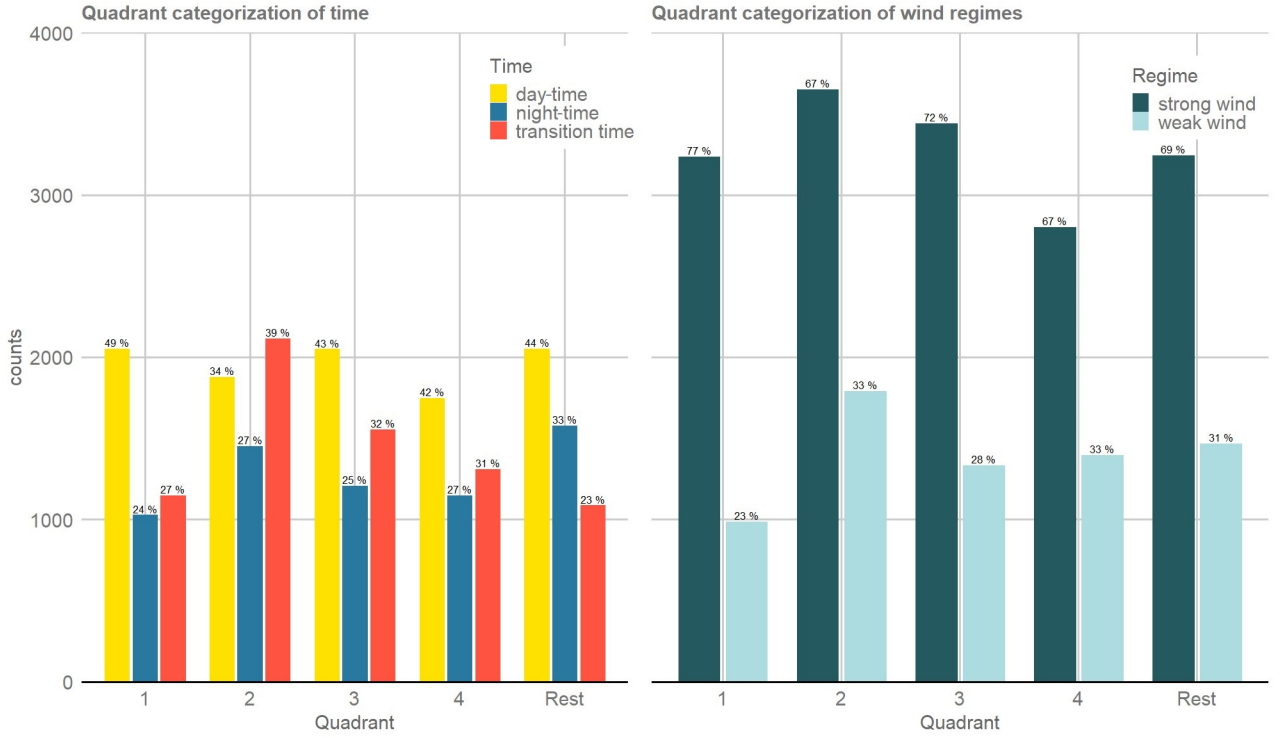


Figure D.4.: Quadrant analysis after times of day (left) and wind regimes (right) for the LOeWE campaign. The categories of the quadrant analysis are given in accordance to Table 4.2 on the x-axis of the two histograms. The frequency of the wind regime or time of day events are displayed by color-coded bars (day-time: yellow, nighttime: blue, transition time: orange, strong-wind: dark green, weak-wind: light green) and given in absolute numbers by the counts of the y-axis. On top of every bar the percentage of each time of day (or wind regime) in relation to the others within the respective quadrant is presented. Occurrences where the kernel density distribution for Table 4.2 were centered in more than one quadrant are summarized in one category named "Rest".